UNIVERSITÀ DEGLI STUDI DI PADOVA
Dipartimento di Fisica e Astronomia "Galileo Galilei"

CORSO DI DOTTORATO DI RICERCA IN ASTRONOMIA
CICLO XXXIV

Open Clusters in the TNG Stellar Population Astrophysics large program.

Direttore della scuola: Ch.mo Prof. Giovanni Carraro
Supervisore: Dr. Sara Lucatello

Dottorando: Ruyuan Zhang

Sommario

Grazie alla conoscenza dell'evoluzione stellare e alle isocrone di ultima generazione, l'etá degli ammassi aperti (AA) pu'øessere misurata con accuratezza, in particolare se se ne conosce la composizione chimica. La possibilitá di accurata datazione unita alla loro distribuzione spaziale, rendono gli OC traccianti ideali del disco galattico: essi infatti si trovano sia nella zona centrale che in quella esterna del disco, vicino al piano galattico.

Gaia, con la *data release 2*, oltre a fornire parallassi precisi, ha portato al rilevamento di molti nuovi ammassi, aprendo una nuova era per lo studio del disco galattico. In seguito a questo, varie campagne osservative, anche all'interno di grandi progetti che usano spettrografi multi-fibra di ultima generazione, si sono concentrate (o si concentreranno) sullo studio della composizione degli AA. Tuttavia, i dati ottenuti con questi strumenti non consentono una completa caratterizzazione chimica delle stelle degli AA, limitandone l'utilizzo nel sondare l'evoluzione chemo-dinamica del disco.

Questo progetto si inserisce nel progetto *Stellar Population Astrophysics (SPA) with TNG*, il cui obbiettivo é mappare ed esplorare la chimica del disco della Via Lattea Parte di questo lavoro prevede l'uso di AA e la derivazione della loro composizione chimica precisa e accurata. In questo lavoro presentiamo l'analisi di un campione di AA situati entro circa 2 kpc dal Sole, con etá da circa 50 Myr a pochi Gyr.

Abbiamo utilizzato HARPS-N al Telescopio Nazionale Gaileo e raccolto spettri ad altissima risoluzione (R = 115 000) di 40 stelle giganti rosse del *Red Clump* in 18 AA (di cui 16 mai o poco studiati, e due di riferimento). Ne abbiamo misurato le loro velocità radiali e derivato i parametri stellari ($T_{\rm eff}$, log g, v_{micro}, e [Fe/H]) utilizzando un approccio 1D - LTE basata sull'analisi delle larghezza equivalente delle righe. Abbiamo inoltre misurato l'abbondanza degli elementi α, O, Mg, Si, Ca, Ti e degli elementi a cattura protonica Na e Al, tutti determinati con il metodo della larghezza equivalente. Abbiamo anche misurato l'abbondanza di Li attraverso il metodo di sintesi.

Abbiamo discusso la relazione tra metallicitá e distanza galattocentrica, aggiungendo i dati della letteratura ai nostri risultati per ampliare il campione e tenendo conto anche dell'etá. I risultati ottenuti per Litio, Sodio e Alluminio sono stati discussi nel contesto dell'evoluzione stellare. In particolare, per Na e Al abbiamo confrontato i nostri risultati con i modelli per studiare il loro comportamento in funzione della massa, suggerendo che l'aumento evolutivo di Na nell'atmosfera stellare di giganti potrebbe iniziare addirittura partire da $2\,M_{\odot}$.

Abbiamo poi studiato i *trends* delle abbondanze radiali, verticali e per etá. trovando gradienti significativi (positivi) solo per [Mg/Fe] e [Ca/Fe]. Infine, i valori di Fe, O e Mg nel campione combinato sono stati confrontati con l'ultima generazione di modelli chemo-dinamici, trovando un buon accordo per i cluster di età intermedia e vecchi. Per gli ammassi piú giovani, troviamo un forte aumento della dispersione delle composizioni chimiche misurate, accompagnato da un *fit* assai piú scadente con i modelli per Fe, O e Mg. Sono state esplorate diverse possibili spiegazioni, comprese le incertezze nella metallicitá derivata, confermando la difficoltá nella determinazione dei parametri per le stelle giovani (età < 200 Myr), probabilmente a causa di una combinazione di fattori intrinseci (attività, rotazione veloce, campi magnetici, ecc.) che i modelli atmosferici non possono riprodurre facilmente e che influenzano i parametri e incertezza di misura chimica.

ii

Abstract

Context: Thanks to modern understanding of stellar evolution, we can accurately measure the age of Open Clusters (OCs). Given their position, they are ideal tracers of the Galactic disc. Gaia data release 2, besides providing precise parallaxes, led to the detection of many new clusters, opening a new era for the study of the Galactic disc. However, detailed information on the chemical abundance for OCs is necessary to accurately date them and to efficiently use them to probe the evolution of the disc.

Aim: Mapping and exploring the Milky Way structure is the main aim of the Stellar Population Astrophysics (SPA) project. Part of this work involves the use of OCs and the derivation of their precise and accurate chemical composition. We analyze here a sample of OCs located within about 2 kpc from the Sun, with ages from about 50 Myr to a few Gyr.

Method: We used HARPS-N at the Telescopio Nazionale Gaileo and collected very high-resolution spectra (R = 115 000) of 40 red giant/red clump stars in 18 OCs (16 never or scarcely studied plus two comparison clusters). We measured their radial velocities and derived the stellar parameters (T_{eff}, log g, v_{micro}, and [Fe/H]) based on equivalent width measurement combined with 1D - LTE atmospherical model. Moreover, the abundance of α-elements O, Mg, Si, Ca, Ti, and the light elements Na and Al, all determined by the equivalent width method. We also measured Li abundance through the synthesis method.

Result: We discussed the relationship between metallicity and Galactocentric distance, adding literature data to our results to enlarge the sample and taking also age into account. We discussed the behaviors of lithium, sodium and aluminum in the context of stellar evolution. For Na and Al, we compare our findings with models to investigate their behaviour as a function of mass, suggesting that Na mixing to the surface during the giant phase might start in masses as low as $2\,\mathrm{M}_{\odot}$. We study the radial, vertical, and age trends for the measured abundance ratios in a sample combining our results and recent literature for Open Clusters, finding significant (positive) gradients only for [Mg/Fe] and [Ca/Fe] in all cases. Finally, we compare Fe, O and Mg in the combined sample with chemo-dynamical models, finding a good agreement for intermediate-age and old clusters. There is a sharp increase in the abundance ratios measured among very young clusters (age < 300 Myr), accompanied by a poorer fit with the models for O and Mg. Several possible explanations are explored, including uncertainties in the derived metallicity. We confirm the difficulties in determining parameters for young stars (age < 200 Myr), due to a combination of intrinsic factors (activity, fast rotation, magnetic fields, etc) which atmospheric models can not easily reproduce and which affect the parameters and chemical measurement uncertainty.

List of Papers

Paper I, Zhang et al. (2021); R. Zhang, S. Lucatello, A. Bragaglia, R. Carrera, L. Spina, J. Alonso-Santiago, G. Andreuzzi, G. Casali, E. Carretta, A. Frasca, X. Fu, L. Magrini, L. Origlia, V. D'Orazi, A. Vallenari (2021). *Stellar Population Astrophysics (SPA) with TNG Atmospheric parameters of members of 16 unstudied open clusters.* A&A, 654 (2021) A77

   Paper II, Zhang et al. (2022); R. Zhang, S. Lucatello, A. Bragaglia, J. Alonso-Santiago, G. Andreuzzi, G. Casali, E. Carretta, V. D'Orazi, A. Frasca, X. Fu, L. Magrini, I. Minchev, L. Origlia, L. Spina, A. Vallenari (2022). *Stellar Population Astrophysics (SPA) with TNG II. α-elements, lithium, sodium and aluminum in 16 open clusters.* To be submitted

   Paper III, Alonso-Santiago et al. (2021); J. Alonso-Santiago, A. Frasca, G. Catanzaro, A. Bragaglia, G. Andreuzzi, R. Carrera, E. Carretta, G. Casali, V. D'Orazi, X. Fu, M. Giarrusso, S. Lucatello, L. Magrini, L. Origlia, L. Spina, A. Vallenari, and **R. Zhang** (2021). *Stellar Population Astrophysics (SPA) with the TNG. Stock 2, a little-studied open cluster with an eMSTO.* A&A, 656 (2021) A149.

iv

Contents

List of Figures

List of Tables

Chapter 1

Open clusters and the Galactic disk

Most of our knowledge of stellar physics, on the ages of stars and on their evolution has been acquired thanks to the study of star clusters, of their formation and evolution and of their stellar populations.

This knowledge has very general bearing in our insight on a variety of astrophysical processes. Age dating stellar populations is necessary to investigate the formation of the Milky Way (e.g. Ness et al., 2016). The interpretation of light from simple stellar systems allows the building of population synthesis models used in studying the star formation history in other galaxies. The rate and timing of mass loss is a crucial ingredient in probing the chemical evolution and feedback processes in galaxies. For all this, stellar clusters are privileged probes and test cases.

Open Clusters (OCs hereafter), in particular, provide key insight on the Galactic disc. These objects are made of coeval, chemically homogeneous, and dynamically bound groups of stars born from the same molecular cloud. With metallicities not too far off from that of the Sun ($-0.5 <$[Fe/H] $<$ 0.5, see e.g. Netopil et al. 2016; Donor et al. 2020; Casali et al. 2019), they are generally young (most of them are < 1 Gyr, but there are clusters with ages as high as 8–10 Gyr, see e.g. Kharchenko et al. 2013; Cantat-Gaudin et al. 2020) and range greatly in size: from loose associations with just a handful of stars to super star clusters, with as many as 10^4 members. As they form and evolve into (or in close proximity to) the Galactic disc, they are prone to stripping and disruption, and are in fact thought to be one of the main sources of field stars (e.g. Lada & Lada, 2003).

Stellar populations in OCs cover stars from low to high mass, and different evolutionary stages, making each cluster a snapshot of stellar evolution at a given age and composition. With ages covering the entire lifespan of the thin disc, OCs trace the young, intermediate-age, and old thin disc components. Age can be measured for OCs with much more accuracy than for Galactic field stars, making them the ideal tool to probe the Galaxy formation and evolution, through the age-metallicity relation, radial gradients and the comparison with theoretical models.

This chapter focus on the basic information and characteristic of OCs trying to explain why the OCs were chosen as the tracer to investigate the galactic disk properties. Then the description is about how OCs as tools to study the Milky Way's disc, and the recent relevant results are discussed in the last part of the chapter.

1.1   What are Open Clusters?

Stellar clusters is a label applied to objects with very different characteristics, with types differentiated on the basis of rather qualitative criteria. In the Milky Way (MW), star clusters are (from least massive to most massive) groups of stars, associations of stars, OCs, and globular clusters (GCs). Super star

clusters (SSCs), very massive stellar clusters, are found mostly in external galaxies, but Westerlund 1 can be considered as a MW SSC (see Portegies Zwart et al. (2010)) and NGC 3603 is also a candidate (Fukui et al., 2014).

The Fig 1.1 shows a collection of images of clusters of different characteristics.

Clusters are considered associated with stars' birth in hierarchical structure and will decompose in the short timescale after forming, which makes them related to both to stellar formation and property and the galaxies evolution procedure. So far, there are thousands of OCs and ~150 GCs were found inside of the Miky Way. Star clusters are crucial as bridges for studying both star formation and galaxies.
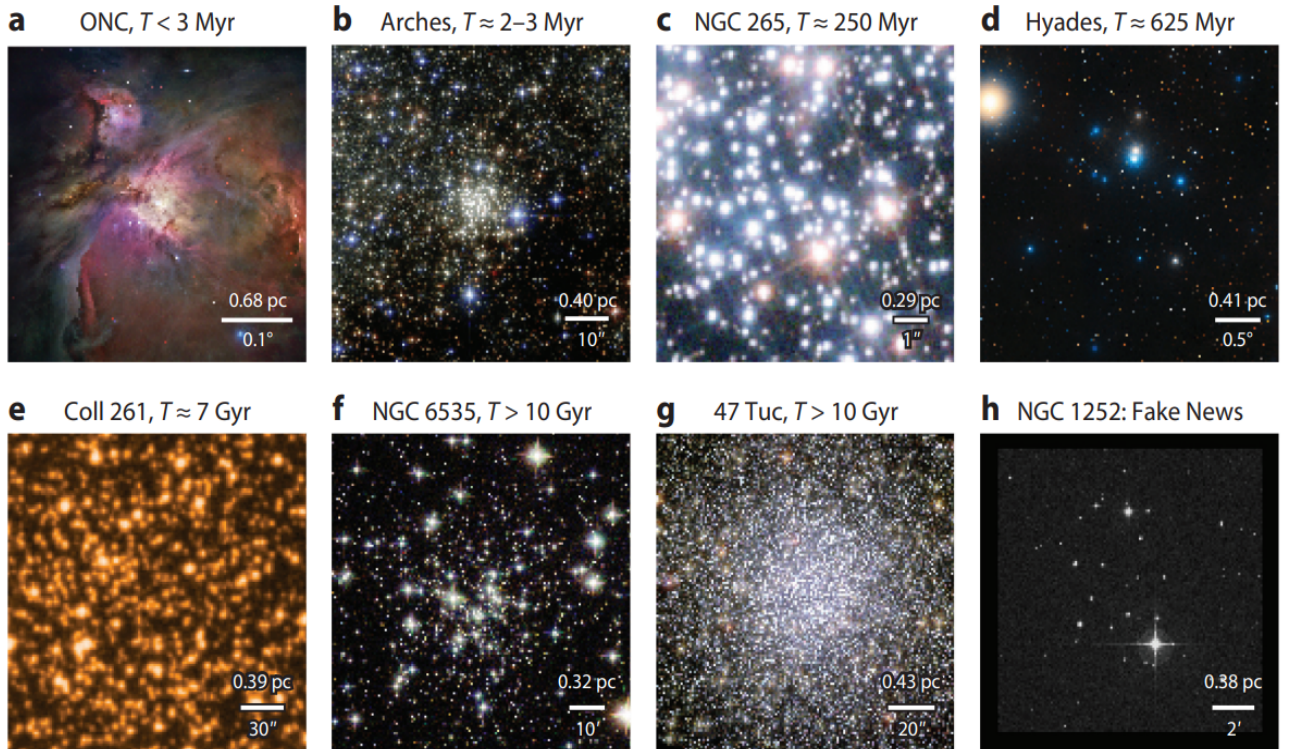
Figure 1.1: This illustration is a series of clusters 3 pc x 3pc field of view (Krumholz et al., 2019) from multiples sources. a:Robberto et al. (2013); b:NASA and ESA; c:NASA and ESA; d:NASA,ESA, and STScI; e:ESO/SDSS; f:ESA/HubblE, NASA; g:NASA,ESA and the Hubble Heritage (STScI/AURA)-ESA/Hubble Collaboration; h:WEBDA datasets

Unfortunately, there are is no clear definitions for the different kinds of clusters.In the past, one of the criteria used to distinguish clusters were their positions, with Globular Clusters (GCs) being star clusters located in the Galactic Halo and Bulge, while OCs were found in the disk, as were YMC (the latter being even more common in other galaxies).

Age has also often be used as a discriminant between OCs and GCs. Fig 1.2 is the H-R diagram of stellar members belong the two types of clusters: OCs (Pleiades or M45) and GCs (NGC 5024 or M53). The differences are clear in this case as the OC under consideration is young (< 150 Myr, see e.g. Gossage et al. (2018)), some MW OCs are as old as 10 Gyr, and young extragalactic GCs are known, a nearby example is the Large Magellanic Cloud that contains clusters with ages ~3 Gyr (Bekki et al 2004). (Bekki & Chiba, 2005) More in general, studies have shows that there is overlap in

the metallicity, density, and mass distribution for OCs and GCs (see e.g. Zhang & Fall, 1999; McCrady & Graham, 2007). There are possible connections between different types of clusters, with e.g. YMCs being the candidates to being analogous to what GCs were in their infancy (see e.g. Maíz-Apellániz (2002); Portegies Zwart et al. (2010))

One kind of definition proposed is based on the gravitational bound between a set of stars (Portegies Zwart et al., 2010). Based on the observational result and dynamical simulation, Portegies-Zwaart focused on the massive young star clusters (YMCs hereafter which related to the massive and young OCs sometimes) YMCs were discovered in more galaxies and the stars clusters are bound satisfied younger than 100 Myr and the massive more than 10^4 $M_\odot$ can identify the YMCs, after the YMCs entered the long-term evolution stage which lifetime depending on stellar dynamical evolution and external interaction. Investigate the properties of YMCs related to stellar evolution and galactic astrophysics, for some YMCs whose ages are consistence with GCs are contains exotic objects.

Lada & Lada (2003) argued that based criteria of stability against tidal disruption by the galaxy and by passing interstellar clouds, and setting an evaporation time (the time necessary for internal stellar encounter to eject all members) $>10^8$ (see Adams & Myers 2001) the minimum number of star in an OC is of 35. This provides a quantitative separation between stellar clusters (OCs) and star associations and star groups.

As of today, there is no well established quantitative set of criteria to identify each type of cluster even the basic parameters have the typical range for each type in Table 1 (Portegies Zwart et al., 2010).

Qualitatively, we can summarise the criteria for MW stellar clusters as follows: GCs and YMCs have high total mass and densities, while OCs and associations are generally less massive and loose. GCs are the oldest of three clusters and hence have the lowest turn-off mass. OCs are found around galactic midplane, and have a composition rich in metals, as are YMCs, while GCs are generally located in the halo or Galactic bulge and are characterised by a lower content of metals.

Moreover, given the age difference, MW GCs are typically red objects, while OCs (especially young OCs) are much bluer.

One interesting approach to establish the separation between OCs and GCs is that suggested by Carretta et al. (2010) and is based on the presence of variations in the content of some key elements (Na-O, Mg-Al, C-N), the so-called anticorrelations. Carretta et al. puts forward the idea that the anticorrelations are a defining feature of GCs. Fig 1.3, from Carretta et al. (2010), illustrates the relation between clusters'a age and absolute magnitudes in V band of OCs and GCs in the MW and Large Magellanic Clouds. They used Fig 1.3 to explain the relationships between clusters' ages and absolute magnitudes and to argue that the anti-correlation is a defining feature of GCs.
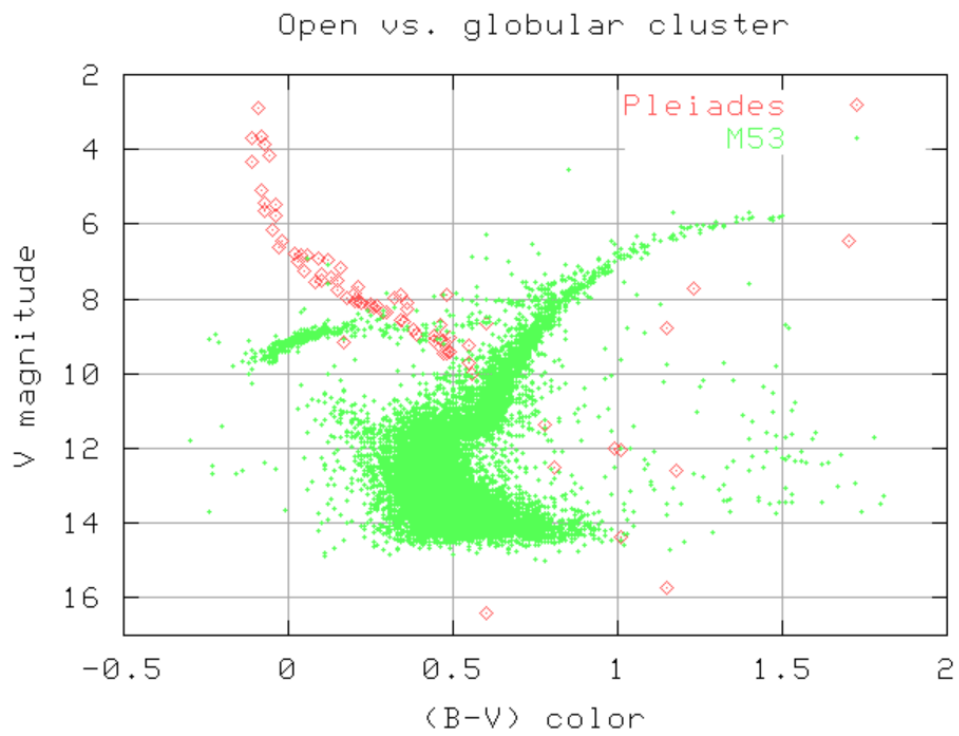
Figure 1.2: This image is from "http://spiff.rit.edu/classes/phys230/lectures/clusters/clusters.html", as we can see from the H-R diagram. Most of Pleiades member are located in main sequence and dominate by bright, massive, blue stars, with turn-off mass around -0.1 at (B-V). However, there are no blue stars in older cluster.
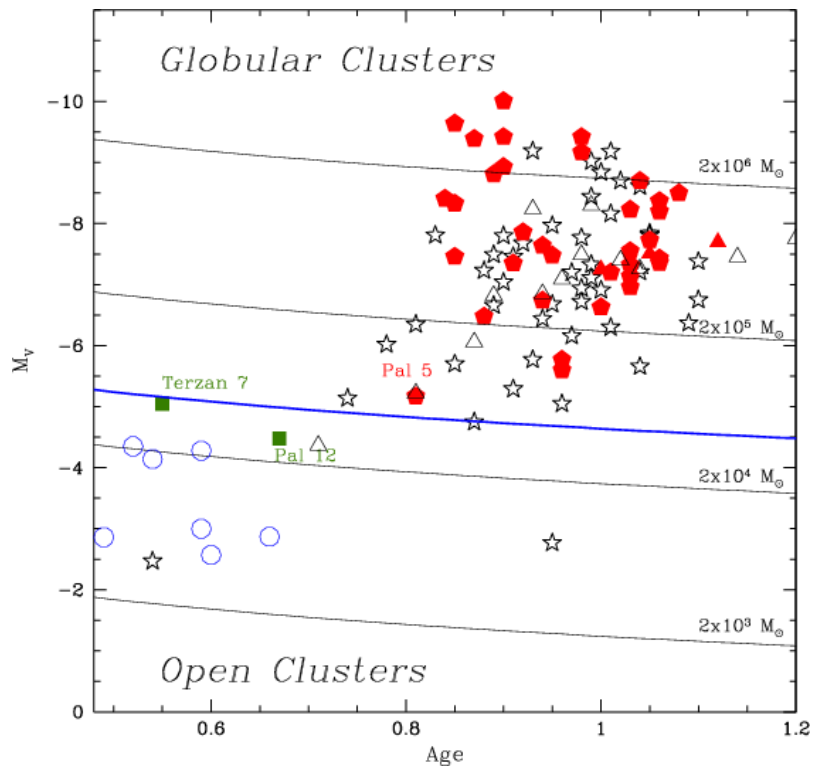
Figure 1.3: The relationship between age and absolute magnitude in V band from Carretta et al. (2010). Solid lines are contours with the same mass, the blue line is the dividing line of OCs and GCs. red filled pentagons and triangles: GCs with Na-O anticorralation in Milky Way (MW) and Large Magellanic Cloud (LMC); green square: cluster without Na-O anticorrelation; open star and triangles: samples without enough data in MW and LMC; open circle: old OCs.

1.2 The Properties of Open Clusters

In general, OCs are regarded as a simple stellar population, namely, their stars were born in the same episode of star formation, and thus share similar properties such as age, distance and composition. This makes OCs ideal laboratories to explore stellar evolution in different phases and for stars of different masses. This also means that the study of just a small subset of their members is sufficient to characterize the chemistry of an OC. It is thus relatively easy to collect data on large samples of OCs, a fact that is exploited in the study of the Galactic disk.

Due to the OCs' being numerous and widespread in the Milky Way, many sky-survey and observational campaigns have aimed at collecting large samples of OCs (see later). In terms of data collections, among the most used sources for is WEBDA (Paunzen, 2008) a website which collects information on OCs in the MW and in the Magellanic Clouds. Catalogs collecting OCs parameters are DAML02 catalogue (see Dias et al. (2002)), and the Milky Way Star Clusters Catalog (MWSC) (Kharchenko et al., 2012, 2013; Schmeja et al., 2014; Scholz et al., 2015) Gaia second data release (DR2) and the early third data release (EDR3) contain precise information about position, parallax, proper motions, photometry of more than 1.8 billion stars, among which those in stellar clusters. The use of Gaia astrometry, possibly combined with auxiliary ground-based information on radial velocity, provides accurate membership information for OC stars (see e.g. Cantat-Gaudin et al., 2018; Jackson et al., 2020).

Size and Mass

Radius and mss are among the most basic properties for clusters. Measurements for radii of OCs are available for a vast majority of the objects included in the large collections. DAML02 reports the radius for essentially all the objects included (2168 OCs, 99.7%), with most of the values being based on visual inspections. Only in a few exceptions the structural properties were explored in more details (see e.g. Seleznev et al. (2010); Cignoni et al. (2011); Donati et al. (2014)) as this requires accurate photometry on relatively large fields of view. Precise determination of structural parameters are dependent on magnitude limit from (brighter, more massive stars are more concentrated) and on FoV size (large enough to cover the whole extension of the cluster). The diameters in DAML02 cover a rather wide range, with young clusters having diameters between 0.6 and 20 arcmins (median 7 arcmins) and old OCs between 0.6 to 20 (median 5). Note that data available in DAML02 is heterogeneous and a considerable fraction of the diameter estimates listed there are affected large errors. However, they are useful to describe the general properties of OCs.

Kharchenko et al. (2013) used 2MASS photometry and proper motions, to homogeneously derive the tidal and code radii for close to 3,000 clusters, over 99% of the objects in the MWSC catalogue. For old open clusters they found ~1.2 pc and ~8.8 pc for the median core and tidal radius respectively. For young OCs, on the other hand, 1.1 pc and 7.6 pc respectively. It is interesting to note that, in terms of angular sizes, the 8 pc of the median tidal radius corresponds to 5 arcmin at a distance of ~10 kpc, suggesting that the angular extension of nearby clusters is larger than what reported in DAML01.

Estimates of the masses are unfortunately not as widely available in the databases and catalogs, and in any case the number of mass measurements available in the literature is much smaller. Mass determination is in general not as straightforward as that for the radius, different methods yield rather different results, and the associated uncertainties are sizeable.

Mass estimates are generally based on star counts, whose accuracy can be severely affected by limits in the data magnitude range or in the size of the field of view considered. In fact, dynamical models suggest that cluster members should be found well outside the apparent diameter, as stars will

linger around the (much larger) tidal radius. Typically, the considered field of view does not reach those distances, and hence ignores those potential cluster members. Another source of uncertainty is the considerable binary incidence in OC stars ($\sim 30\%$ on average, with higher fractions among the more massive stars/younger clusters). This often poorly constrained quantity needs to be corrected for when determining star counts, affecting its accuracy. Dynamical evolution is also expected to play a role in old clusters, causing mass segregation and evaporation of low mass stars, and the compensation of these effects affects the accuracy of the mass determination. Finally, the magnitude range covered by the data is also a source of uncertainty, as the magnitude limits turn into coverage of the luminosity function and mass ranges, leading to significant extrapolations outside the range.

Age

Clusters are regarded as being made of coeval stars: while strictly speaking the individual star formation time change according to the mass, the differences are generally negligible with respect to the age of the cluster, at least when excluding young OCs.

Putting all stellar members on the H-R diagram (also called color-magnitude diagram CMD) is one of the most used approaches to investigate the cluster properties. The CMD measures the stellar relevant information individually, the mass determination of main sequence turn-off star can infer the age (infer the time when hydrogen burn out theoretically), which represents other stellar as well. The study of the CMD features and the comparison with theoretical isochrones with various approaches is the most used method to determine ages in old OCs. For young OCs, different approaches are used (see e.g. Soderblom 2013), with the most accurate being the Lithium Depletion Boundary technique, applied in the 20-200 Myr age range.

In summary, OCs, at least in a relative sense, are easily dated and their age determinations are accurate. Thus they can provide a key tool to study the chemical evolution of their host galaxy. Ideally, to study them as a system in the MW (or in general) homogeneously derived ages based on fully consistent sets of theoretical models would be of particular importance. Unfortunately, this is not the case: a wide variety of theoretical models coupled with different methodologies are often used in literature, and collections such as WEBDA or DAML02 are affected by systematics. This is not the case of e.g. MWSC or of recent studies based on Gaia (see e.g. Cantat-Gaudin et al. (2020)).

Kharchenko et al. (2013) in the MWSC catalog used isochrone fitting method for all the clusters based on Padova isochrones (excluding pre-main sequence isochrones, which are based on different models). They adopting one single metallicity, solar (they adopt Z=0.019), arguing that this has a very modest effect on accuracy of derived ages in the relevant metallicity range (for old OCs 10% internal error and up to 40% external error [1]). The age MWSC clusters age distribution has a median of 0.4 Gyr, with 75% of the OCs within 1 Gyr. The median age for just the old OCs (> 300 Myr) is 0.9 Gyr, with 75% of them is within 1.5 Gyr. The age distribution is plotted in Fig 1.4, Piskunov et al. (2018). DAML02 age distribution is not so different: overall median age is 0.3 Gyr, with 75% of it is within 0.8 Gyr, median age for old OCs is 0.8 Gyr, with 75% of them younger than 1.4 Gyr.

A more recent work, Cantat-Gaudin et al. (2020), determines ages using a a data driven approach using neural-networks, and includes in its sample newly discovered OCs on the basis of Gaia data, these clusters are typically quite young. In fact, in this case, the overall age distribution has a median of 0.2 Gyr, with 85% of the OCs within 1 Gyr. The median age for just the old OCs (> 300 Myr) is 0.8 Gyr, with 76% of them is within 1.5 Gyr.

---

[1] They suggest that the source of discrepancy could be the differences in the adopted theoretical models and/or to poor membership determinations
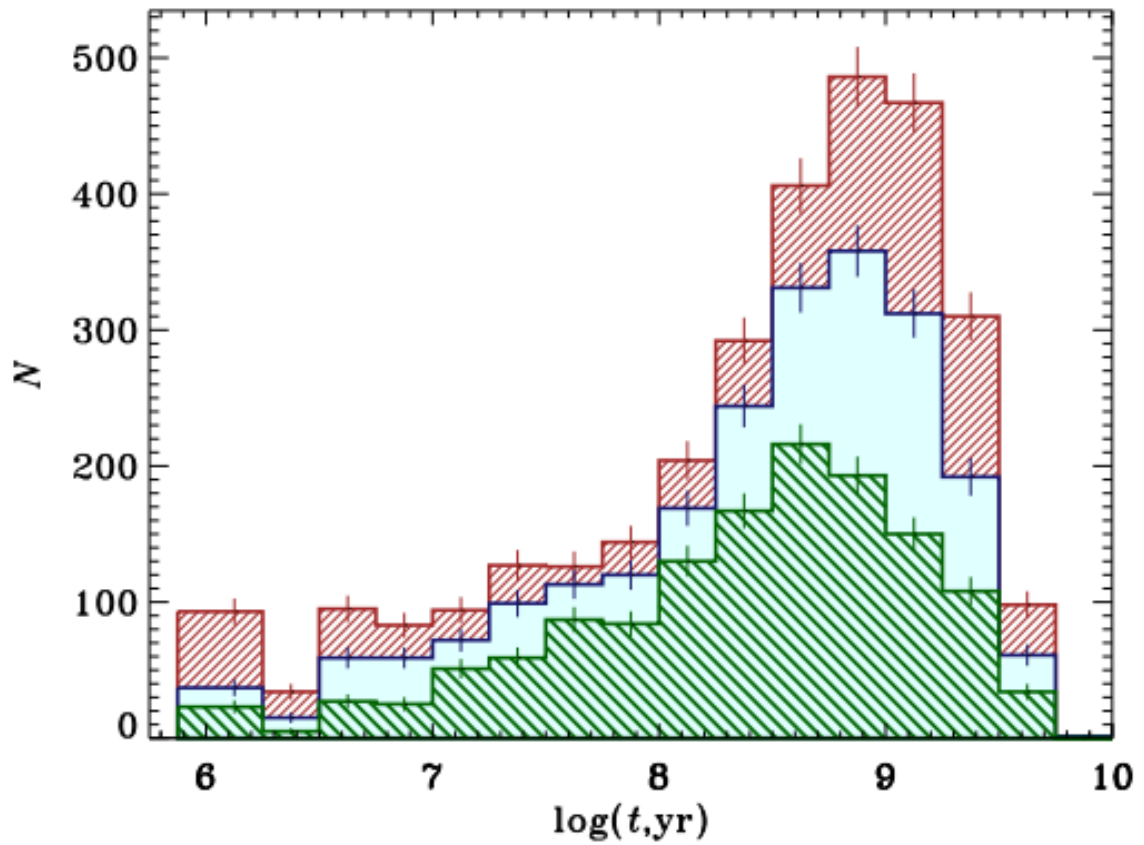
Figure 1.4: The age distributions of MWSC clusters (total 3061) from Piskunov et al. (2018). The brown background hatched histogram is the total sample, the intermediate blue histogram represent the clusters within individual completeness, the foreground green histogram is the clusters within the general completeness, and the vertical bar is the Poisson error.

Composition

Overall metallicity for OCs has been derived through photometric indices, whilelow and high resolution spectroscopy have lead to more detailed information on their composition. For the cluster located near enough, high resolution spectroscopy allows the derivation of individual abundance ratios. OCs cover a range in metallicity $-1 <$[Fe/H]$ < 0.4$ (from Kharchenko et al. (2013)), with most of the clusters between -0.4 and 0.1. The MWSC catalog clusters show a weak age-metallicity relation, which is however not present in the DAML02 catalog (note that Cantat-Gaudin et al. (2020) does not provide metallicity). Observations collected to date show that OCs have very uniform composition, both in overall metallicities and other chemical elements (α-, Fe-peak, p-capture and n-capture elements), with a the scatter within 0.05 dex generally for high-resolution spectrum (De Silva et al., 2007a). Some very small differences have been observed in the old cluster M67 NGC2682: Liu et al. (2016a,b) show small changes (0.02 to 0.03 dex) in the composition, with possible causes including the infall event of planet (Meléndez et al., 2017) and atomic diffusion (Dotter et al., 2017). Due to the OCs being young, usually, within a few hundred million years, the stars still stay around at their original positions they formed and contained the progenitor information. Interestingly, in moving unbound groups the similar homogeneous were found (De Silva et al., 2007b).

Position and Kinematics

Stellar clusters positions in the Milky Way vary according to different ages and types. Fig 1.5 is the positions distribution of OCs and GCs. OCs are both closer to the galactic center and midplane and the GCs have the opposite properties, spanning large distances from the galactic center and midplane. The younger clusters are more clearly identified with in the galactic disc.

Even restricting the consideration to just OCs, objects of different ages have different spatial contribution, a fact that was noticed already by van den Bergh in 1958. The oldest OCs reach the farthest distances from the Galactic centre and the Galactic plane, while the younger ones are much more closely associated with the disk. Figure 1.6 shows the distribution of young and old OCs based on the results reported in Cantat-Gaudin et al. (2020). We note that incompleteness and selection effects also play a role in this distribution. The lack of objects in the inner Galaxy is partially affected by the high extinction present in this region, concealing – at a given distance – preferentially old clusters which are fainter than brighter young clusters. This, however, does not exclude the existence of evolutionary or physical selection effects. Large dynamical age results, for instance, in considerable orbital variations due to interaction with the spiral arms (see e.g. Roškar et al., 2012) might have played a role. On the other hand, further away clusters are more likely to survive disruptive encounters happening within the disk.

Other explanations have been suggested. Yong et al. (2005), for instance, by studying chemical signature of a sample of outer OCs, argued that they have experienced a nucleosynthetic history significantly different from other Galactic population, and proposed that outer disk OCs might in fact originate from past merging events. On the other hand, Carraro et al. (2007) did not find any significant evidence of extra-galactic origin of the outer OCs based on the chemical composition.

Kinematical studies of individual stars are key in establishing cluster memberships.

On the other hand, studying the kinematical properties of the overall system of OCs, can shed light on the mechanisms that destroy clusters.

Gaia has brought a veritable revolution in the kinematic study of OCs, both internal and as a system. Naturally, it has also allowed the detection of many of such objects, and the refinement of membership at an unprecedented precision, see e.g. Cantat-Gaudin et al. (2020).
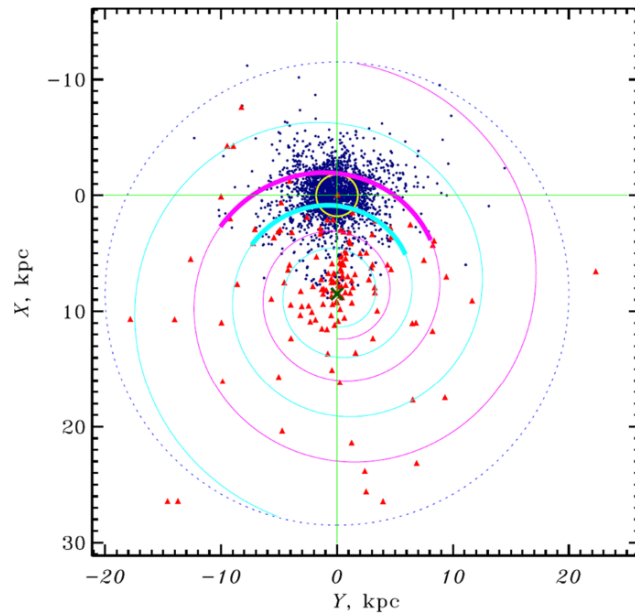
Figure 1.5: The figure is published in Kharchenko et al. (2013), shows the clusters' position distribution in the Milky Way with XY-plane. blue dot:OCs and associated group; red triangles:GCs; thick solid cyan and magenta lines: local spiral arms; the yellow thick circle: the surveys region within 1.8 kpc radius around the Sun; cross: the galactic center with the position of (8.5,0).
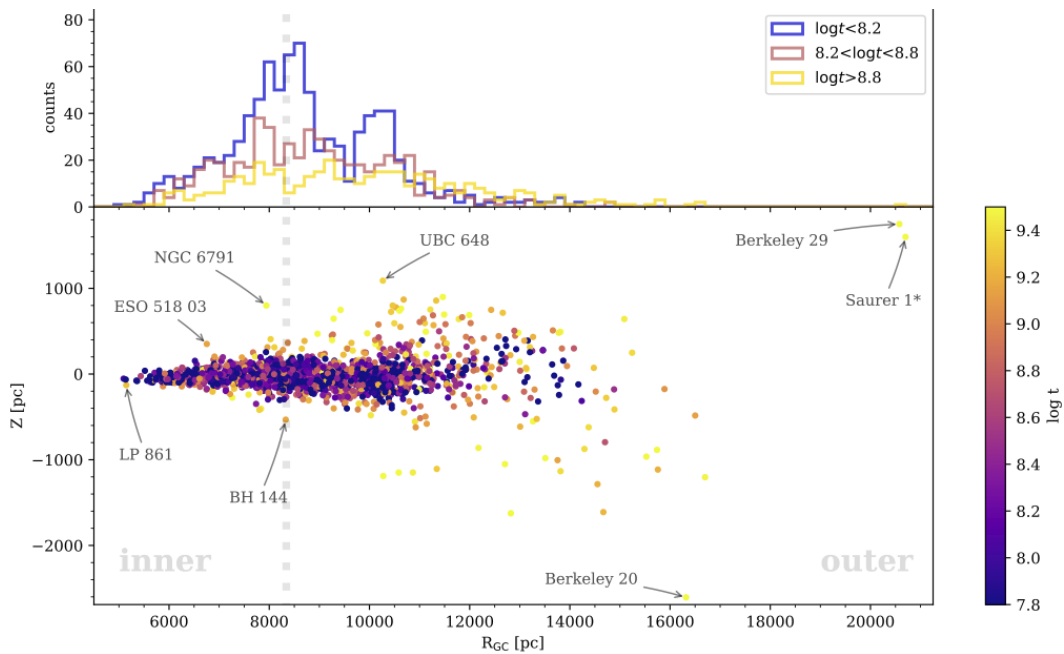
Figure 1.6: Figure from Cantat-Gaudin et al. (2020), showing the spatial distribution of Galactic OCs. Top: galactocentric distribution, bottom: distance from the galactic midplane as a function of galactocentric distance.

Tarricq et al. (2021) recently published a study of the kinematics of over 1300 OCs, which coupled Gaia EDR3 results with radial velocities from a variety of sources (e.g. APOGEE, Gaia-ESO, RAVE, GALAH etc). They derive reliable orbital elements for over 400 clusters.

They find that that for most of the clusters the maximum altitude above the plane reached during their orbits is less than 400 pc. Clusters older than 1 Gyr are typically capable of much further motion, bust still remain confined within 1 kpc. There is also a relation between age and eccentricity, with OCs being born typically in circular orbits and having their eccentricity affected increasingly by perturbations, as their age increases.

1.3 Chemo-dynamical evolution of the Galactic disk and OCs

Galaxies contain dynamically bound stars. In general, the typical large spiral galaxy, such as the MW, includes more than 10^{10} stars and has a diameter of ~30 kpc. Moreover, the densities of galaxies are 10^7 times more than the mean densities of the Universe. Galaxy can be defined and identified using this conception. The investigation of the galaxy is from diverse aspects including cosmology; initial conditions, and physical processes. In some cases, galaxy formation and evolution can be regarded as the physical procedure based on cosmology combined with initial and boundary conditions, but the physical processes related to various space sizes and age scales make the understanding of galaxies are complex. Moreover, from the aspect of empirical, looking at the galaxies that have high redshift is the same as looking at the galaxies that have similar ages of Universe. And explore the galaxies at different epochs in statistics, those samples span a wide range of masses, sizes, and diversity morphologies. The comparison shows the galaxy structure parameters following the various scaling relationships. Furthermore, the galaxies' researches are not only related to their characteristics but also as a probe to indicate the structure and evolution of the Universe. Due to the bright, plentiful, and long-lived, galaxies that can be observed in the long-distance and large time scale with a sufficient number of samples, that makes galaxies as the unique tracer to detect the whole Universe and constraints the cosmological parameters.

Morphology is one of the most basic properties for galaxies. Nowadays, the earliest classification of galaxies through galactical morphology Hubble sequence is available, that morphology sequence indicating the galaxies formation history. Spirals and ellipticals are two basic galaxy types. Hubble classification covers the galaxies types from pure ellipsoids to pure disks. Elliptical galaxies are formed by stars' random movement, which shows mildly flattened. Spiral galaxies are related to disk galaxies which are rotation support, that have highly flattened galaxies. However, most of the galaxies are combined with both spirals and ellipticals. In 1845 William Parsons discovered the special structure. The Milky Way is one of the typic spiral galaxies with the structure in Fig 1.7, In 1785 William Herschel confirmed the galactic stars distributed as the disk shapes around the Sun, based on the galaxy cross-section with star gauges. From now we knew the galaxy dominate by disk structure with 50 $M_\odot$, around 3.5 kpc of radial length and 0.3 kpc for the vertical scale. the dick are 10-20 % of the thin disc with a smaller radial range and 1 kpc vertical scale. However, the Milky Way includes more like a halo, bulge structures, and also contains complex parts like the fragments infall from the central halo collapse (Searle & Zinn, 1978).

In what follow we will focus on the Milky Way disk. Not because most of the galaxies' components belong to the disk. It contains other galaxies' information like angular momentum, star formation, and the spiral arm evolution. The Galaxy disk investigations are crucial for galaxy formation and evolution. A series of works derived the galaxy detail properties. Salpeter (1959) gave the initial mass function(IMF) for the first time, and Schmidt (1959) defined using the relationships between density
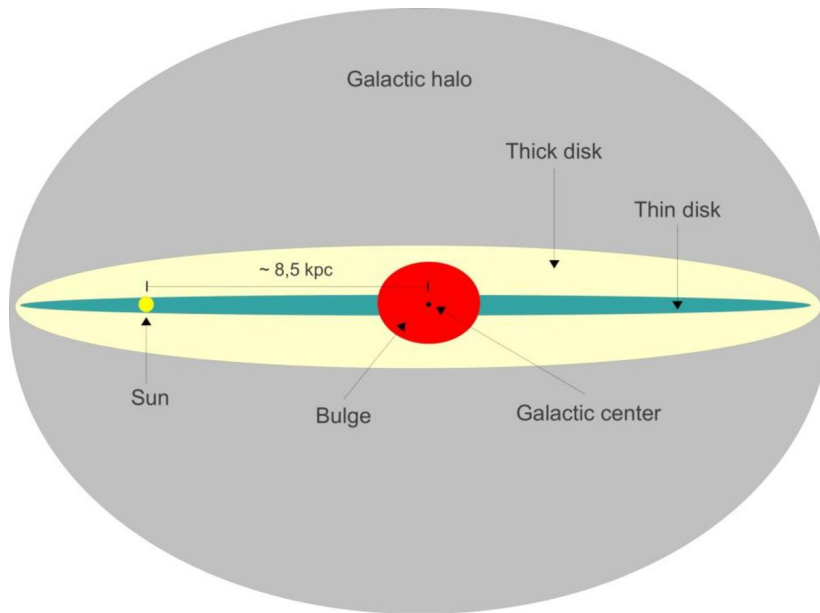
Figure 1.7: Sketch of the Milky Way structure on the edge on view are from Wikipeda. Sun located on the galaxy midplane with the 8.5 kpc galactocentric distance. The thin disk is the dominate baryonic of the Galaxy with the mass around $50\,\mathrm{M}_\odot$. And the mass of thick disk reduce to $30\,\mathrm{M}_\odot$ with lower rotation velocities. Other structure contains galactic bulge which mass are around $10^{10}\,\mathrm{M}_\odot$, the last part is halo have 3% of bulge mass even its radius is larger.

and ISM can represent the rate of star formation. In the chemical evolution, research Tinsley (1980), the G-dwarf appears to live longer and with low metallicity compare with the solar neighborhood, which is the G-dwarf problem. Garnett & Shields (1987) added the chemical enhancement and star formation to extend the previous chemical evolution models (Searle et al., 1973), which just contains the metallicity radial gradient following the galactic disk. Based on those works, the understanding of galactic is ongoing, including collecting more observation data and extending the galactic models with more complex evolution information.

Sky Surveys

One of the main open issues in modern astrophysics is to understand the history, formation, and evolution procedures of the galaxy. Combining the recent observation data with the theoretical and simulation, we explored further nature of the Milky Way. From the modeling, similar galaxies have a stable evolution process and smooth star distributions. However, multiple data combinations in different dimensions revealed more details for galaxies. Sky-surveys data provide sufficient data to explore more irregular galaxy structures. Enough and accurate observation result allows simulating a more complex galaxy evolution process. Moreover, multiple sky surveys data help to build the seven-dimensional (7-D) space, including three spatial coordination, velocities in three directions, and chemical abundances (which can itself turn into further dimensions if individual abundance ratios are considered). These are a results of combining multiple techniques: the derivation of distance and proper motions from astronomy and that of radial velocity and chemical composition from spectroscopic studies complemented by photometry.

The Galaxy disk investigations are crucial for the undestanding of galaxy formation and evolution.

In the past, the observation required a lot of time to collect the stellar data, usually consuming a few decades. The current sky-surveys with multiobjects, high-resolution facilities allow the carrying out of galactic surveys programs more efficiently, which are complemented by wide-sky or all-sky coverage photometric campaigns. Some recently completed or ongoing galactic surveys relevant to the present discussion are briefly described in the appendix.

OC as probe of the disk

The study of MW OCs is one of the key approaches to investigating the Galactic disk, trace its structure and chemical evolution. In fact, as previously discussed, they cover a rather large range of distances across the disk

They have been recognised as such for many decades, thanks to the relative ease in the determination of age, distances and age, as previously discussed. This allowed the measurements of metal gradients with galactocentric distance, with distance from the midplane and ages.

Thanks once again to Gaia and to modern surveys, the study of open clusters has made strides in the last couple of decades. In the next section we will discuss the studies modern surveys have performed of Galactic OCs. Note that other metallicity tracers have been used for the disk, including Cepheids, planetary nebulae (PNe), and H II regions, which will however not be discussed in the present text.

Chemical evolution and simulations

The primordial gas of Universe after the Big Bang is H, He. And also includes some light elements (Li, Be and B, etc). The first star (population III) without metal exploding produces heavier elements like C, O, Ne, Mg, Si, and Fe. As the massive stars evoluve into supernova, the massive star will explode, eject energies and chemical material into the gas. Studying this gas enrichment process is the key to understanding the galaxies formation early, especially the population III is crucial, which influence the early galaxy formation and evolution from dynamical, thermal, and chemical. The different chemicals will be synthesized at different timescales from stars, which process leads to the element ratio change following the time. Investigating them helps to trace back to the galaxy chemical enhancement (galactic archaeology). That makes galactic chemical evolution (GCE) a tool for understanding the history of galactic formation(Tinsley, 1980) and also provide a new aspect to detected the detail both of stellar evolution and supernovae(Kobayashi et al., 2011) And the GCE contains the information of stellar yields(Kobayashi et al., 2006; Timmes et al., 1995). One of the simples models is called the monolithic model based on the cosmology framework. One of the simples models is called the monolithic model based on the cosmology framework. The model is assumed mixed uniformity and has consentaneous elements composition. The relevant works are listed in Tinsley (1980); Prantzos et al. (1993); Timmes et al. (1995); Chiappini et al. (1997); Kobayashi et al. (2000)

The general model parameters include the proportion of supernova type Ia (Kobayashi & Nomoto, 2009), the trend and limitations of IMF, the galactic age. All of these parameters are the function of star formation and outflow time scale. Most of the model parameters are based on the observations like the gas fractions, age-metallicity correction, metallicity distribution function (MDF), and IMF which have the best constraints from observation data. The IMF from Salpeter (1955); Chabrier (2003); Kroupa (2008) lead to the different simulation results. Nowadays, Stochastic models (Argast et al., 2002; Cescutti, 2008) can simulate the really ISM mixing situation, which is inhomogeneous actually. In the work of Tumlinson (2006), the models considerate the hierarchical structure with the mass accretion on cosmology background. Recently, the model with 3D simulations (chemo-dynamical

simulation) are used to predict the chemical evolution of the Galaxy (Kobayashi & Nakasato, 2011; Minchev et al., 2014a,b). The prediction can calculate the information on age, position, chemical composition considered with the asymmetry mixing process.

Many galactic disk models in 1990-1980 were based on the assumption that the gas infall process leads the galactic formation, mentioned the timescales are longer than 3 to 4 Gyr, considered with the metallicity distribution of G-dwarf. Larson (1976) suggest the disk inside-out formation by gas accretion, through chemo-dynamic simulation. The inner accretion is faster than that of the outer region, which leads to the negative abundance gradient in the thin disk (Matteucci & Francois, 1989). However, Chiappini et al. (1997) build "two-infall" simulation indicated the galaxy formation consist of two procedures, the halo and thick disk formed on the first stage, and the second phases spending longer time from 7 to 8 Gyr which relate to thin disk formation. Moreover, Yoshii (1982) and Gilmore & Reid (1983) discovered thick disk structure, there are different stellar densities between thick and thin disk, the stars belong to thick disk have high [α/Fe], similar with that from halo, but the dynamical characteristics are different from that of halo and thin disk membership.

The radial and vertical metallicity gradients and their evolution with time provide crucial insight in the formation and evolution of galaxies and can constraint models of formation and chemical evolution of the disk. The key input from OCs are the presence of a negative radial gradient in the inner disk which flattens in the outer disk, a significant metallicity dispersion at any distance and age and a poor age-metallicity correlation.

These findings are a challenge to traditional GCE models, which generally reproduce the present-day distributions but fail to predict its evolution (see e.g. Magrini et al 2009 for a comparison of models to observations, but also Tosi 1996 for discussion of different types of models).

Chemo-dynamical models are a better match to observations, as they are able to at least qualitatevely predict the evolution of the metallicity gradient as will be discussed later (see also e.g. Casamiquela et al. (2019)).

1.4   Recent Relevant Work

The Gaia results have brought a veritable revolution in our knowledge of OCs. High probability memberships based on proper motions and parallaxes have been derived for very large samples of stars, leading also to the discovery of a substantial number of new OCs (see e.g. Cantat-Gaudin et al., 2018; Castro-Ginard et al., 2019, 2020; Liu & Pang, 2019; Sim et al., 2019).

Presently, only a minority of OCs has been studied with high quality spectroscopic data, implying not only a lack of information on the composition for the vast majority of OCs, but also possibly inaccurate ages. In fact, a precise metallicity is a key ingredient for the derivation of ages from photometry (see e.g. Bossini et al., 2019). Moreover, the sample is likely to be affected by bias towards larger clusters, where, in the years before Gaia membership information, it was easier to successfully target actual members.

While Gaia will, at end of mission, provide distances and proper motions with a precision < 10% for almost all known clusters, its spectroscopic capabilities are rather limited. The crucial third kinematic dimension (radial velocity, RV) and detailed chemical composition will need to be largely provided by ground-based complementary observations.

Recently completed and ongoing large stellar surveys, such as Gaia-ESO (GES), GALAH and APOGEE (Gilmore et al., 2012; De Silva et al., 2015; Majewski et al., 2017, respectively), have provided composition and RVs for a few thousands of stars in some hundred of OCs based on high-resolution (~20-40K) spectroscopy. This sample will be further increased by WEAVE (Dalton et al.,

2020), which has the study of OCs as one of the primary goals of its Galactic Archeology Survey, and by the 4MOST Stellar Cluster Survey (de Jong et al., 2019).

A brief summary of the OC focused work in large ongoing or recently completed surveys and projects follows:

- **Gaia** There are a series of work that investigate the properties of Galaxy disk combined with OCs based on Gaia data. The work of Cantat-Gaudin et al. (2018) obtained the parameters of proper motions and parallaxes for 128 OCs (combine Gaia DR1 TGAS parallaxes and proper motions and UCAC4 proper motion to derive the possibilities of OCs membership) and used a Bayesian/Markov Chain Monte Carlo technique to fits stellar isochrones from 2MASS data. They thus derived the cluster parameters (age, metallicity, extinction, distance modulus) combined with spectral data. Finally, the orbital parameter is from the galactic potential. In the work of Cantat-Gaudin et al. (2020), about 2000 stellar clusters were selected from Gaia DR2, and basic stellar parameters(ages, distance modulus, interstellar extinction) were determined through an artificial neural network to homogeneous the catalog. Those parameters are not only can help to understand the cluster formation and disruption, but also can used to detect more complex structure of galactic disc. 3D distribution can be used to investigate the galactic disc structure with warping and flaring in the outer disc. However, the reason for the specific structure is unclear, more kinematic data should be derived combined with age may help to learn insight into the evolutionary history of the Milky Way.

- **GES** Gaia-ESO(GES) is a survey aimed at collecting around 10^5 stars and covering almost all stars in the Galaxy, including the halo samples and the stars in the star formation region. Gaia data provide homogeneous information of chemical composition and dynamic distribution combined the Gaia data help to rebuild the knowledge of the Milky Way. There are many works based on the Gaia-ESO program. The Casali et al. (2019) using open clusters selected from Gaia-ESO and APOGEE calibrated the correlation of age and [C/N] ratio. Some chemical abundance like [C/N] related to the stellar age, based on empirical isochrons fitting with the extra-mixing affection are taken into account in [C/N] determination, the present ratio of [C/N], and ages confirmed by the stellar evolution model (Salaris et al., 2015; Lagarde et al., 2017). For the Open cluster, the changes of age-[C/N] correlation can not be ensured. For the field stars, the ratio of [C/N] shows clearly distinguish for thin and thick disk membership on [α/Fe] versus [Fe/H], furthermore, they estimated the ages of the thin disk and calculated the lower limit of the thick disk. The typical thin-disk stars are younger than those belonging to the thick disk, and the age of stars have low |Z| shows a decreasing trend towards the galactic inner and outskirts region. Those indicated the inner metal-rich stars are tracer the later phase of the Milky Way formation and the galaxy formed from inner to outer. In the work of Sanna et al. (2020), 14 Li-rich stars were studied in global clusters in various evolution phases: 2 dwarfs, 2 AGB stars, 1 post-AGB star, and 9 stars in different regions of RGB or SGB. Most typically Li-rich stars have a lithium abundance of 0.5-1.5 dex. The fourth super-Li rich stars were discovered in NGC1261, which belongs to the RGB bump, the reason of Li enhancement was mentioned by D'Orazi et al. (2015), However, the further detection shows the reason of Li en-richment may include : the extra mixing process in RGB bump stage; but the Ha lines activity in chromospheric support the engulfment assumption. Another possible reason is the mass transfer from the RGB companion when the star on the main sequence.

- **GALAH** Here list of two works on a large number of OCs. Carrera et al. (2019) increased RV and chemical abundance of 1229 OCs from multiple catalogs combined with Gaia DR2 data.

The information of radial velocities, iron abundance, and other elements(Na, Mg, Al, Si, Ca, Cr, Mn, Ni) also are from multiple sources. The Gaia data was used to detect the possibilities of OCs membership. The RV, metallicity, and other elements were derived from APOGEE and GALAH. In this work, the metallicity abundance for 39 OCs was first detected. And the trend of chemical abundance, their result consistent with that from previous work which shows flatten in the outer region. Spina et al. (2021) identified 205 secure members (according to the properties of kinematic) from 226 potential clusters(GALAG or APOGEE), detected 21 elements based on two surveys, and studied the element gradients throughout the galactic disk. and trying to insight the formation and evolution of the galactic disk combines self-consistency, the age distribution. Finally, the spatial and temporal evolution of chemical abundance was studied. Gao et al. (2018) studied one old OCs with high accuracy of data. They measured 7 elements of chemical abundance in 66 stars from OCs M67, based on GALAH (high-resolution) spectral, and corrected by NLET correction. And they noticed the mean abundance was reduced for all elements after NLET correction. And the NLET shows different effects on different evolutionary phases. Then they compared their result with that from atomic diffusion prediction. Turn-off stars and sub-giants are consistent with the prediction, but red-giant and red-clump are poorly modeling consistency. One of the possible reasons is the stellar parameters are determined not accurate so the 3-D atmosphere model will be considered in future work. Then the NLTE correction elements are used to study abundance evolution and chemical tagging.

- **APOGEE - OCCAM** The Open Cluster Chemical Abundance and Mapping (OCCAM) survey provides homogeneous data that can be used to derive the clusters' distance, reddening, ages, and chemical compositions. OCCAM program will combine multiple sources like the data from 2MASS (Skrutskie et al., 2006), GLIMPSE-1 -2 -3D,360 (Benjamin et al., 2003), WISE (Wright et al., 2010), and SDSS/APOGEE. The information of radial velocity, stellar parameters, and chemical compositions are mainly from APOGEE data, corresponding to the other astrophysical surveys the follow-up works about star membership identification, galactic abundance determination, and neutron capture measurement are ongoing. Many works have been published based on OCCAM project, Donor et al. (2020) focuses on 128 open clusters (71 high-quality samples) using APOGEE DR16. Derived abundance for 16 species based on 71 high-quality samples. And then they obtained galactic abundance (alpha, iron-peak, odd-z) gradient according to 4 age bins, and compared the result with that from the chemical evolution model. It is the first time to find the knee in the galactic abundance at R_{gc}=13.9kpc. But the limitation of samples beyond this distance may lead to the unreliable result.

- **OCCASO** Unlike the previous ones, OCCASO is a project which is not part of a large survey. All the information is from the homogeneous data reduction and analysis procedure. There list four works for OCCASO surveys, the final aim of the series of papers is the homogenous and accurate studies of OC to gain insight into the Galactic Disk. (the value of the radial velocities is used to confirm the membership of OCs, and the median radial velocities for each cluster can be used to study their kinematics related to the disc and the spiral arms) In Casamiquela et al. (2016) 77 stars in 12 OCs were studied. They discuss data reduction approaches and present the radial velocities. From Casamiquela et al. (2017), atmospheric parameters (effective temperature, surface gravity, microturbulence and metallicity) for 115 red clump stars in 18 OCs were derived, combined two methods(equivalent width(EW): DAOSPEC+GALA and spectral synthesis(SS):iSpec). In the third work (Casamiquela et al., 2019), Casamiquela analyzed 10 elements for red giants in 18 OCs, from the high-resolution spectrum R>65000. Ni,

Cr, Si, Ca, and Ti was obtained using EW. V, Sc, Mg, and O abundance are computed by SS. Then they explored the changes for mentality and other chemical abundance with R_{GC}, $|Z|$, and ages. From the comparison between OCCASO atmospheric parameters and the results from the model (pure chemical model and chemo-dynamical model of MW thin disk), the younger clusters are consistent with the pure chemical model, however, for the older cluster, the dynamical affection including heating and migration should be considered. That conclusion were confirmed in the [X/Fe]-age (within 3 Gyr) relationship and also supported by the comparison of chemical abundance with chemo-dynamical prediction. And the trend of [X/Fe] vs R_{GC} and $|Z|$ of OCs almost following the region of that for field stars. The last relevant work (Casamiquela et al., 2018) studies the α-elements abundance for the young cluster (NGC 6705, 300 Myr) based on 8 red clump stars. Using the EW method to derive the Si, Ca, and Ti abundance, and spectral synthesis fit (O and Mg). Then they compared the α-element abundances with that from APOGEE and GES, explored the kinematic study of this cluster, investigated the orbits to detect the birthplace at 6.8-7.5 kpc, and found the mild α-enhancement (O, Mg, and Si) for younger samples, which is not only for older samples. However, those enrichment mechanism are different from that in Chiappini et al. (2015), the local enhancement from type SN II in molecular cloud is the possible reason.

The key feature of past, ongoing and of the future large surveys resides in their ability to study multiple members of the clusters in all evolutionary phases, with tens to many hundred of stars observed in each cluster (while APOGEE, for instance, relies generally on much smaller samples). This is in fact a crucial step in the understanding of the formation of the clusters (see e.g. Jeffries et al., 2014; Mapelli et al., 2015) and the evolution of the stars' properties following changes in rotation, activity, surface abundances, all key constraints to modern stellar evolutionary models (see e.g. Bertelli Motta et al., 2018; Smiljanic et al., 2016; Lagarde et al., 2019, on diffusion and extra mixing). However, because of their spectral coverage and/or resolution, the abovementioned large surveys (GES, OCCASO, GALAH, Gaia) are not suitable to provide a complete chemical characterization from the crowded spectra typical of OC giant stars. An accurate determination of chemical abundances requires spectra with a very high resolution and a wide spectral coverage, to measure the full set of the Fe-peak, CNO, α, p- and n-capture elements with high accuracy, on a par with the astrometric and photometric information provided by Gaia.

This implies that there is a need for observations that take a complementary approach, i.e. study in details with high-resolution (R > 50-70000), large wavelength coverage, and high signal-to-noise spectroscopy a few stars per OCs, deriving a full chemical characterization. Indeed, measuring elements of all nucleosynthetic chains, which probe different nuclear reaction sites in stars, means providing robust constraints to stellar evolutionary models and to the history of the Galactic disc.

Projects like OCCASO are moving in this direction, however it is critical to widen the sample of clusters targeted by such high quality studies.

Chapter 2

The Stellar Population Astrophysics Large survey at TNG

The Gaia second data release (DR2) and the early third data release (EDR3) contain precise information about position, parallax, proper motions, photometry of more than 1.8 billion stars, among which those in stellar clusters. The use of Gaia astrometry, possibly combined with auxiliary ground-based information on radial velocity, provides accurate membership information for OC stars (see e.g. Cantat-Gaudin et al., 2018; Jackson et al., 2022, respectively). Presently, only a small fraction, about 10%, of the OCs in the Milky Way have been observed by high-resolution (HR) spectroscopy and, with more objects being identified by Gaia[1], further observations with very high-quality data are crucial to investigate further the structure of the thin disk.

Gaia has also spectroscopic capabilities (see e.g Sartoretti et al., 2018; Cropper et al., 2018). However, those spectra, taken at relatively low resolution (R=11500) and in a narrow wavelength range near the infrared Calcium triplet, allow only the determination of a limited number of elements, with rather large uncertainties. On the other hand, accurate composition information is necessary not only to study the chemical properties, but also to reliably measure the age of OCs (see e.g. Bossini et al., 2019), with obvious repercussions.

The key feature of past (e.g. SEGUE, GES), ongoing (e. g. APOGEE, GALAH) (see e.g. Randich et al., 2022; Donor et al., 2020; Spina et al., 2021) and planned surveys (e.g. WEAVE, 4MOST) resides in their ability to study multiple members of the clusters in all evolutionary phases, with tens to many hundred of stars observed in each cluster (APOGEE is an exception, as it generally relies on much smaller samples). This is in fact a crucial step in the understanding of the formation of the clusters (see e.g. Jeffries et al., 2014; Mapelli et al., 2015) and the evolution of the stars' properties following changes in rotation, activity, surface abundances, all key constraints to modern stellar evolutionary models (see e.g. Bertelli Motta et al., 2018; Smiljanic et al., 2016; Lagarde et al., 2019, on diffusion and extra mixing). However, because of their spectral coverage and/or resolution, these surveys provide an incomplete chemical characterization of OC stars (a partial exception is Gaia-ESO for the small fraction of stars observed with UVES-FLAMES at high resolution, R=47000). An accurate determination of chemical abundances requires spectra with a very high resolution and a wide spectral coverage, to measure the full set of the Fe-peak, CNO, α, p- and n-capture elements with high accuracy, on a par with the astrometric and photometric information provided by Gaia.

This implies that there is a need for observations that take a complementary approach, i.e. study

---

[1]Hundreds of new OCs have been identified based on Gaia data, (see e.g. Castro-Ginard et al., 2019, 2020, 2021; Sim et al., 2019; He et al., 2021). In addition, large scale structures have been discovered, (see e.g. Kounkel & Covey, 2019).

in details with high-resolution (R > 50-70000), large wavelength coverage, and high signal-to-noise spectroscopy a few stars per OCs, deriving a full chemical characterization. Indeed, measuring elements of all nucleosynthetic chains, which probe different nuclear reaction sites in stars, means providing robust constraints to stellar evolutionary models and to the history of the Galactic disc.

Thus, important contributions can come from other, smaller scale projects, dedicated to OCs. These projects provide the chance to collect spectra with high enough resolution and wide enough coverage to investigate the detailed chemical composition of OCs probing all main nucleosynthetic channels. An example is the OCCASO project (Casamiquela et al., 2019), where about 50 OCs have been studied using different spectrographs with R>50000. Another one is OSTTA (One Star to Tag Them All) which uses FIES@NOT (R=65000) and FLAMES@VLT (R=45000), with more than 50 OCs observed (see Carrera et al., 2022, for the first results). In this context, the TNG based large program "Stellar Population Astrophysics" has targeted a number of young OCs with the idea of widening the sample of well studied objects.

2.1   The telescope and the spectrographs

Telescopio Nazionale Galileo (TNG) is the Italian instrument in the Canarian island of La Palma (belongs to Roque de Los Muchachos Observatory) with 3.5 diameter, and an Adaptive Optic system.

There are four current instruments contains two high-resolution spectrographs HARPS-N and GIANO-B, that can be operated simultaneously in GIARPS mode, HARPS-N has a resolution power of 115000 and covered the wavelength range between 3830 and 6930 Å, and the long time stability observation ability allows TNG to provide accuracy velocity measurement (better than 1m/s), used to find the earth-like size exoplanets. GIANO-B with the high-resolution of 50,000 IR spectrograph, and the observation range is 0.9-2.5 micron, those data can be used to explore the detail of stellar abundance and atmospheric parameters.

There are two multi-mode facilities, allow collect imager and spectral data. The instrument (DO-LORES) in virtual wavelength, with spectral power from R=300 to R=7000, was used to detect extragalactic objects and transient events. NICS consists of an imager and spectrometer obtaining at 0.9 - 2.5 micron, suitable for transition events detection and solar systems.

2.2   The program

The program "SPA-Stellar Population Astrophysics: the detailed, age-resolution chemistry of the Milky Way disk" began in 2018, and was set to investigate the properties of young stellar clusters spanning wide distances, including the inner disk. The program aims at obtaining high quality spectra of more than 500 stars across the Milky Way thin disk, observing luminous giant and supergiant stars in young stellar clusters and associations, luminous Cepheid and Mira variables up to large distances and Main Sequence in open clusters in the Solar neighbourhood. Fig 2.1 is the targets distribution at space.

The high S/N and high-resolution spectrum are meant to explore the chemical behaviors for think disk with homogeneous spectral analysis procedure, including detail of iron-peak-elements, α-elements, neutron-elements, light-elements, and composition produced in the CNO cycle. The precision chemical abundances derived from the HR spectra, combined with the ages and distance of OCs, allow probing the age-composition-distance relationships and are meant to shed light on a number of open questions regarding disk formation, evolution and chemical enrichment, provide constraints to
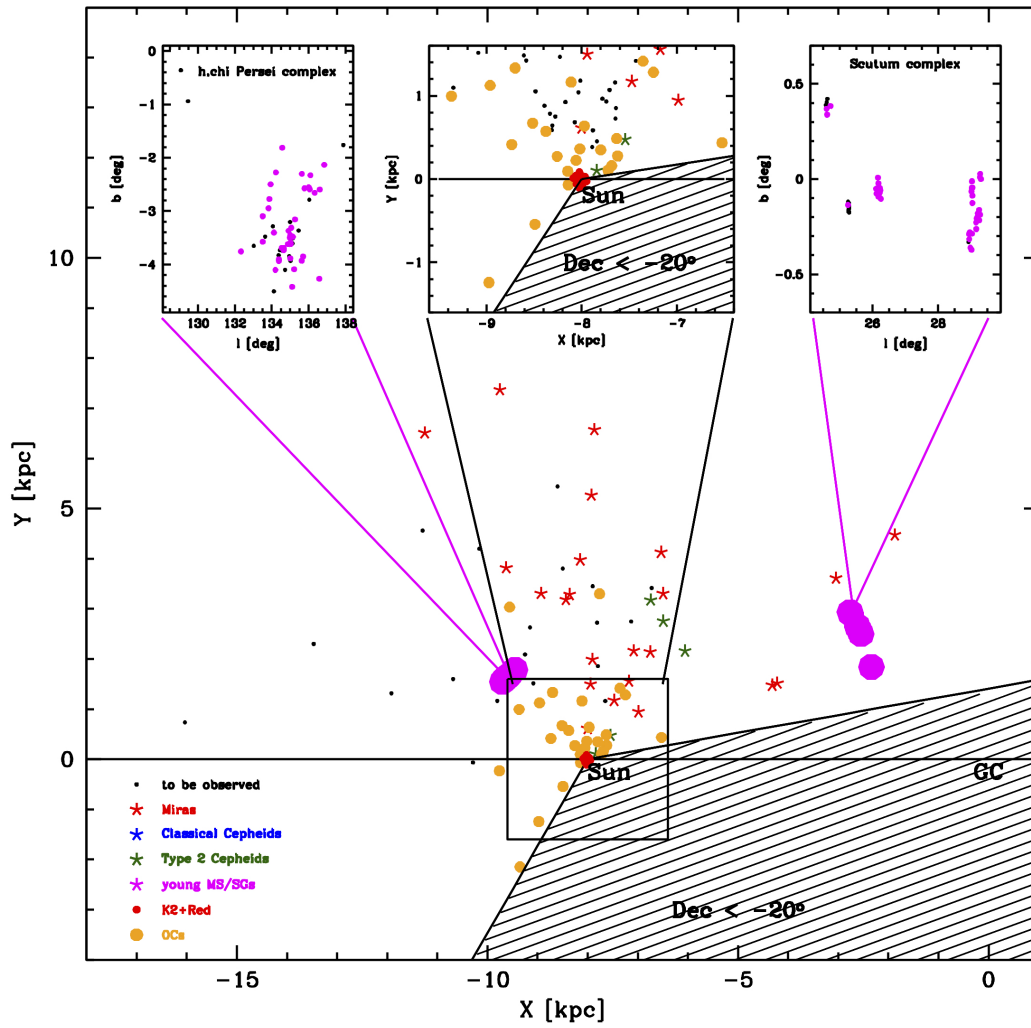
Figure 2.1: Spatial distribution of SPA targets.The illustration is from http://nisp.oabo.inaf.it

stellar evolution models and nucleosynthesis calculations. Moreover, the age-metallicity and distance-metallicity gradients derived, will allow comparing our results to the latest chemo-dynamical models for the Galactic Disk.

The SPA project collected spectra by using the combined HARPS-N and GIANO echelle spectrograph with TNG, GIARPS, the wavelength covering the full optical range and NIR range. This means that observation in the optical range and near-IR are executed at the same time, with the light from a single target separated using a dichroic (a few more details can be found in previous SPA papers, see e.g. Frasca et al., 2019; D'Orazi et al., 2020). The full target list of of SPA is around 500 objects, with a typical magnitude for HAPRS-N of from 10 to 12 in the V band, and for the near-IR instrument, GIANO-B of J=7-11. The main request for the collected spectrum is the signal-to-noise ratio reached at 30 within 1 hr exposure time. For the brightest targets, the exposure is around 30 min and the exposure time increases at 2hrs when observing the faintest targets, however, the condiction of seeing can also affect the signal-to-noise ratio. Taking into account the bad weather and technique issue, the 638hr exposure is needed based on per targets 1hr is needed, for the standard 9hrs nigh observation time, about 1hr should be used for science calibration. Total 80 nights were awarded, 33 for HARPS-N, 27 for GIANO-B, and 20 for GIARPS.

2.2.1   The OC survey from SPA

A total of 23 OCs were observed within SPA, The targets list and additional list of targets (31 OCs) are listed in Tables 2.1,2.2 They were selected to be nearby clusters with a preference for young objects. The clusters were generally poorly studied (no or limited high-quality high-resolution optical spectroscopic studies). The very well studied cluster NGC2682 - M67 was also observed as a comparison cluster and a reference point for the resulting abundance analysis. Of these, seven have the object of published studies. Here we will briefly summarise the results relative to the clusters for which results have already been published:

There four clusters were presented in Casali et al. (2019), who used HARPS-N obtained optical spectral four old OCs. Using LTE atmospherical model and ROTFIT code (Frasca et al., 2006) derived the atmospherical information contains effective temperature, surface gravity, metallicity, and microturbulence,

- **Collinder 350** is the OCs located in the most inner galactic center regions, have previous studied by Kharchenko et al. (2005); Pakhomov et al. (2009); Yen et al. (2018). Recently, Casali et al. (2019) studied 2 red giants in the SPA program, with the optical spectrum. The accurate stellar parameters and chemical composition were analyzed except for one giant are cooler with lower metallicity and appears large dispersion compared with another member, they think to measure the line located in spectrum continuum are difficult, which uncertainties are supported by the inaccuracy existed in the atmospherical model for the cool giant. But the stellar evolution stage does not influence the result from ROTFIT code.

- **Gulliver 51** The youngest OCs in this work studied by Cantat-Gaudin et al (2018b) and Monteiro & Dias (2019), the stellar parameters and chemical composition were derived based on 2 samples by EW method and ROTFIT code.

- **NGC 7044** Have been investigated by Sagar & Griffiths (1998); Warren & Cole (2009). The stellar parameters and chemical composition were derived based on 4 samples by EW method and ROTFIT fitting by Casali et al. (2019)

- **Ruprecht 171** seven stars were selected to do the analysis in Casali et al. (2019), and the work of Ruprecht (1966); Tadross (2003) explored the basic properties of this cluster before, which is the oldest one in this work. The model considered star rotation and mixing are necessary for explain the Li behaviors of old OCs, and there are no Li enrichment stars in Rup 171.

  With the chemical behaviors for all samples, they discussed the correlation of [X/Fe] versus [Fe/H], the α-elements show enrichment with lower metallicities, and have an increasing trend in the outer region, which indicates the galactic formation star from the inner region. Iron-peak does not appear slopes with [Fe/H], and s-process elements appear consistent with the general properties.

- **Stock 2** Alonso-Santiago et al. (2021) analysed optical HARPS-N and Catania Astrophysical Observatory Spectrograph spectra for 46 stars (main-sequence around turn-off stage and giants including three double lines binaries) in Stock 2. They derive radial and rotational velocities, and 1-D, LTE analysis atmospheric parameters and abundance ratios for 21 chemical abundance (C, odd-Z, α-element, iron-peak, and s-process). They explore the OC's characteristics and probe the extended main-sequence turnoff (eMSTO). They found differential reddening, to which they attribute the eMSTO, which, unlike in other clusters, is not explainable with variations in rotational velocities. The main sequence and giant appear consistent insofar chemical composition, except Ba and Sr appear systematic higher for the giant.

- **ASCC123** The young open cluster ASCC 123 (discovered by Kharchenko et al. (2005)) was studied by Frasca et al. (2019) based on the spectra of 17 stars observed with GIARPS (Claudi et al., 2016) instrument. They derived radial and rotational velocities, identifying a new SB2 system. They also derived the atmospheric parameters and determined the abundance of 21 species in 1D, LTE. The average metallicity abundance of ASCC 123 is around 0.14 dex, which value is consistent with the expectation. And the chemical compositions are generally in the range of galactic trend for the thin disk. But V, Co, and Y appear overabundant, Na and Zn are underabundant. And the data indicated the young age of ASCC 123 around 100-250 Myr.

- **M44** The Praespe(M44) is considered to have similar ages and chemical abundance with that of Hyades, but some researches has oppsite conclusions. To re-esitimate the properties of Praespe D'Orazi et al. (2020) combined GIARPS optical and near-IR spectra, deriving atmospheric parameters of 10 solar-type dwarf, and chemical composition (light-elemets, α-elements and iron-peak elements) using 1D, LTE analysis, with NLTE corrections applied for Na. They found that the average iron abundance for Praespe is lower than that of Hyades. They argue that difference in iron abundance suggests the age of Praespe should be younger (570-600 Myr) than previous estimates(Meléndez et al., 2014). D'Orazi et al. (2020) illustrates the relationship between [Fe/H] and ages in Fig 2.3, where in general for OCs younger than 1Gyr, the metallicity abundance is lower than solar. Considered the migration, Praesepe may be born at R_{GC}=5.9 kpc, and moved to the current position (d=1.8 kpc). Moreover, K2 surveys and radial velocity studies demonstrate both of those two clusters contain planets, which may relate to the high metallicities.

The remaining 16 (plus NGC2682 - M67) are the subject of the rest of this dissertation. In the following chapters, the compositions of these OCs is studied and used as galactical thin disk tracer to investigate the trend of metallicity and chemical behaviors.

- **The 16 poorly studied OCs in this study** The basic information of selected 16 OCs is from Casali et al. (2020), the OCs position, distance, R_{gc} and the distance from galactic plane, those
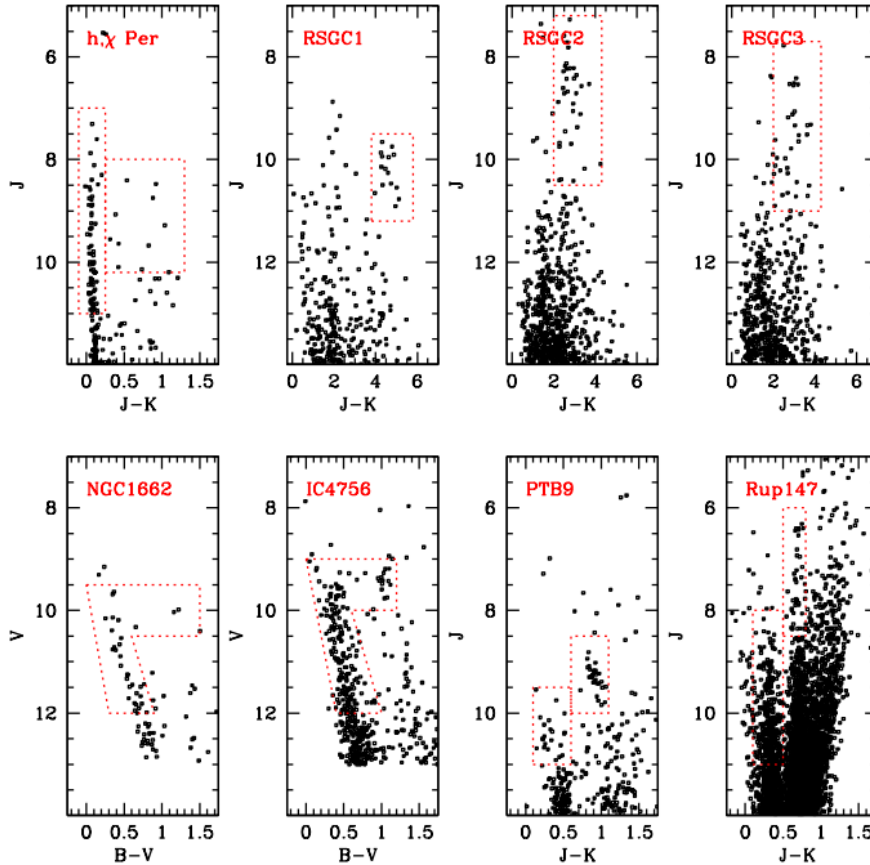
Figure 2.2: The optical and NIR color-magnitude diagrams for some proposal clusters in SPA proposal.The red box are the regions contains observation targets, the cluster NGC1662, IC 4756, PTB9 and Rup147 contains MS and evolved stars, and MS and blue/red supergiants for young OCs h,χ Per. The stars in the OCs RSGC 1,2,3 contains RSGs, which are bright enough for NIR observation and suitable for GIANO-B instrument.

Table 2.1: Properties of the observed targets.

Name	α	δ	Epoch	Time	Additional Information
Miras	18 to 20	-07 to +31	J2000	11hr	11 stars; 7 G, 4 GH
Miras	20 to 22	+30 to +55	J2000	27hr	27 stars, G
Miras	22 to 24	+56 to +64	J2000	15hr	15 stars, G
Miras	00 to 02	+62 to +64	J2000	7hr	7 stars, G
Miras	02 to 04	+59 to +63	J2000	6hr	6 stars, G
Miras	04 to 06	+23 to +54	J2000	10hr	10 stars, G
Miras	06 to 08	+07 to +24	J2000	6hr	6 stars, G
Cepheids	18 to 20	-19 to +31	J2000	33hr	33 stars, 15 H, 9 G, 9 GH
Cepheids	20 to 22	+28 to +61	J2000	20hr	20 stars, 7 H, 13 G
Cepheids	22 to 24	+43 to +63	J2000	14hr	14 stars, 12 H, 1 G, 1 GH
Cepheids	00 to 02	+51 to +64	J2000	10hr	10 stars, 4 H, 6 G
Cepheids	02 to 04	+52 to +69	J2000	7hr	7 stars, 4 H, 3 G
Cepheids	04 to 06	+13 to +59	J2000	12hr	12 stars, 7 H, 4 G, 1 GH
Cepheids	06 to 08	-02 to +36	J2000	9hr	9 stars, 6 H, 3 GH
RSGC1	18 37 58	-06 53 00	J2000	15hr	15 stars, G
RSGC2	18 39 20	-06 01 42	J2000	15hr	15 stars, G
RSGC3	18 45 20	-03 24 43	J2000	15hr	15 stars.G
Alicante 7	18 44 29	-0 00 00	J2000	10hr	10 stars,G
Alicante 8	18 34 51	-0 00 00	J2000	10hr	10 stars,G
Alicante 10	18 45 30	-0 00 00	J2000	10hr	10 stars,G
NGC869	02 19 00	+57 07 42	J2000	15hr	15 stars,GH
NGC884	02 22 23	+57 07 30	J2000	15hr	15 stars,GH

Note

H=HARPS-N
G=GIANO-B
GH=GIARPS

Table 2.2: Additional list of the observed clusters.

Name	α	δ	Epoch	Time	Additional Information
Platais2	01 12 54	+32 03 00	J2000	15hr	15 stars,H
ASCC 123	22 42 23	+54 15 00	J2000	10hr	10 stars,H
NGC1333	03 28 55	+31 22 12	J2000	10hr	10 stars,H
IC 348	03 44 36	+00 54 00	J2000	10hr	10 stars,H
ASCC 19	05 27 41	-01 57 54	J2000	7hr	7 stars,7H
Collinder 359	18 00 29	+02 52 30	J2000	13hr	13 stars,H
Melotte 111	12 23 56	+26 18 00	J2000	5hr	5 stars,H
NGC1662	04 48 07	+10 55 30	J2000	10hr	10 stars,H
Stock 2	02 14 38	+59 26 24	J2000	10hr	10 stars,H
NGC2281	06 48 18	+41 04 48	J2000	10hr	10 stars,H
IC 4756	18 38 56	+05 27 00	J2000	10hr	15 stars,GH
NGC2189	06 12 07	+01 03 18	J2000	5hr	5 stars,GH
NGC2270	06 43 56	+03 28 12	J2000	5hr	5 stars,H
NGC6811	19 37 22	+46 23 42	J2000	5hr	5 stars,H
Dolidze 36	20 02 28	+42 09 54	J2000	5hr	5 stars,H
Collinder 421	20 23 09	+41 41 42	J2000	5hr	5 stars,H
NGC6940	20 34 26	+28 16 48	J2000	15hr	5 stars,H
PTB 9	23 50 01	+68 01 59	J2000	15hr	15 stars,GH
NGC752	01 57 05	+37 47 24	J2000	5hr	5 stars,GH
NGC2099	05 52 21	+32 34 12	J2000	5hr	5 stars,GH
NGC2632	08 40 23	+19 41 24	J2000	5hr	5 stars,H
NGC2682	08 51 32	+11 48 54	J2000	10hr	10 stars,GH
Ruprecht147	19 16 22	-16 15 00	J2000	5hr	5 stars,GH
NGC1342	03 32 01	+37 21 25	J2000	5hr	5 stars,H
NGC1528	04 15 23	+51 11 24	J2000	5hr	5 stars,H
NGC1746	05 04 34	+23 49 48	J2000	5hr	5 stars,H
NGC2168	06 09 13	+24 21 36	J2000	5hr	5 stars,H
NGC2301	06 51 47	+00 27 54	J2000	5hr	5 stars,H
NGC2548	08 12	-05 46 12	J2000	5hr	5 stars,H
Turner9	19 37 22	+29 15 36	J2000	5hr	5 stars,H
NGC6991A	20 02 27	+47 27 58	J2000	5hr	5 stars,H
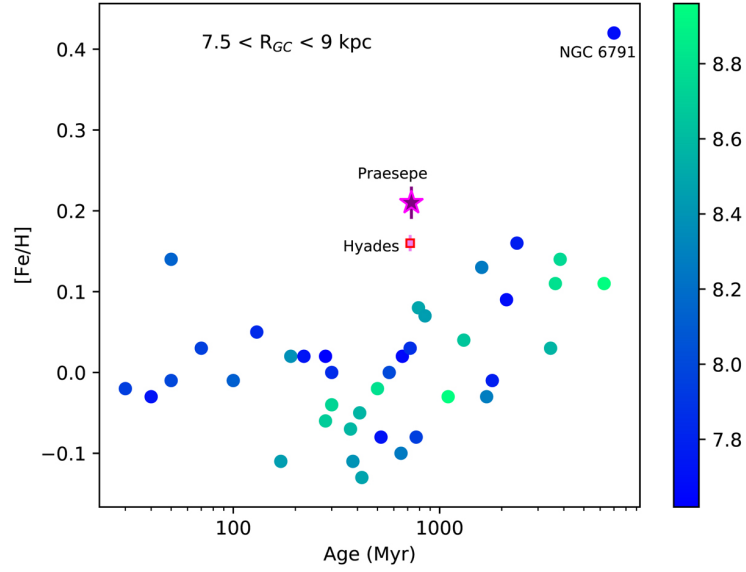
Figure 2.3: The correlation between [Fe/H] and ages for samples around the solar colorcode by galactocentric distance, the figure pubulished in D'Orazi et al. (2020), and the data including ages, metallicity for all OCs are from Netopil et al. (2016), and the data for Hyades are from Liu et al. (2016a).

are listed in section 3.2 Table 3.1. Furthermore, 5 OCs are in common with the previous literature, four of them have a single star in common (Collinder 350 Casali et al. (2020), Basel 11b (APOGEE DR16), Tombaugh 5 Baratella et al. (2018) and NGC 2548 Spina et al. (2021)). For NGC 2682, the relevant results are based on multiple work including the results from Jacobson et al. (2011); APOGEE DR16; (Casamiquela et al., 2019); Gao et al. (2018); Luck (2015); Spina et al. (2021). More information are in the section 5.5 table 5.7.

Chapter 3

The present sample: Sixteen poorly studied Open clusters

3.1 Basic information of 16 OCs

My Ph.D. project aims at the chemical characterization of 16 poorly studied OCs under the SPA framework and use them as a tool to investigate key properties of the Galactic Disk. The precision atmospheric parameters and chemical abundances derived from the HR spectra, combined with the ages and distance of OCs allows probing the age/metallicity/distance relationships using all nucleosynthetic channels (Fe-peak, α, n-capture, etc). Data for two more clusters, M67 – NGC 2682 and Collinder 350, were also analysed for comparison purposes, and to assess the existence of systematic offsets arising from the analysis procedure. Collinder 350 is listed in Collinder 1931 catalog for the first time, the first property study of Collinder 350 is from Kharchenko et al. (2005), and Pakhomov et al. (2009) obtained the spectrum for one candidate in high-resolution. More recently, Casali et al. (2019) used the SPA spectrum updated the information of Conllinder 350. NGC 2682 is one of the most studied OCs in the Galaxy, having been widely analysed in the literature. Even though M67 is significantly older than most of the clusters in our sample, therefore, strictly speaking, is not ideal as a calibrator for the measurements derived from spectra of young stars. However, it is an extremely well studied cluster, and for these reasons is a touchstone object generally included in surveys (e.g. APOGEE, GALAH) and large studies. As our sample gets combined with literature results when compared with chemo-dynamical models for the disk, minimising offsets with respect to the literature is of great importance, and M67 is the best object for this purpose Basic information for the targets is listed in Table 3.1 is based on Cantat-Gaudin et al. (2020) analysis of the Gaia-DR2.

3.2 Targets selection

In this work, we present the analysis of 40[1] giant stars in 18 open clusters. These clusters were selected because they are in the Sun vicinity so we could obtain good quality, high-resolution spectra and are old enough to have stars evolved off the main sequence. The target stars were not selected directly from the Gaia DR2 catalog, but from the membership analysis done by Cantat-Gaudin et al. (2018). We targeted only stars with high membership probability and we have from one (in 8 cases) to a maximum of 7 stars (in 1 cluster) per OC.

---

[1]We observed 41 stars, but one is a double-spectrum binary and was excluded from analysis.

Table 3.1: Properties of the observed clusters, parameters are from Cantat-Gaudin et al. (2020) based on Gaia DR2

Cluster	RA (J2000)	Dec (J2000)	l (deg)	b (deg)	logAge (yr)	A_V (mag)	plx (mas)	pmRA (mas yr^{-1})	pmDE (mas yr^{-1})	dist (pc)	R_{GC} (pc)	$|Z|$ (pc)
ASCC 11	03:32:13.44	+44:51:21.6	150.546	-9.224	8.39	0.60	1.141	0.926	-3.030	867	9095	139
Alessi 1	00:53:22.32	+49:32:09.6	123.255	-13.33	9.16	0.08	1.390	6.536	-6.245	689	8726	159
Alessi-Teusch 11	20:16:30.48	+52:03:03.6	87.435	9.268	8.16	0.37	1.520	-0.139	-1.295	634	8335	102
Basel 11b	05:58:11.28	+21:57:54.0	187.442	-1.117	8.36	1.56	0.534	1.046	-4.137	1793	10121	34
COIN-Gaia 30	01:24:19.20	+70:34:26.4	125.684	7.878	8.41	1.25	1.346	-6.145	2.067	767	8804	105
Collinder 463	01:48:07.44	+71:44:16.8	127.391	9.358	8.06	0.79	1.137	-1.715	-0.307	849	8874	138
Gulliver 18	20:11:37.20	+26:31:55.2	65.527	-3.971	7.60	1.59	0.613	-3.198	-5.646	1595	7816	110
Gulliver 24	00:04:38.64	+62:50:06.0	117.62	0.447	8.25	1.05	0.636	-3.241	-1.57	1498	9131	11
Gulliver 37	19:28:18.48	+25:20:49.2	59.547	3.806	8.55	1.33	0.642	-0.775	-3.74	1438	7712	95
NGC 2437	07:41:46.80	-14:50:38.4	231.889	4.051	8.48	0.73	0.603	-3.838	0.365	1511	9345	106
NGC 2509	08:00:48.24	-19:03:21.6	237.844	5.840	9.18	0.23	0.363	-2.708	0.764	2495	9887	254
NGC 2548	08:13:38.88	-05:43:33.6	227.842	15.390	8.59	0.15	1.289	-1.313	1.029	772	8857	205
NGC 7082	21:28:44.64	+47:06:10.8	91.115	-2.859	7.79	0.79	0.729	-0.293	-1.106	1339	8472	66
NGC 7209	22:04:53.76	+46:30:28.8	95.480	-7.296	8.63	0.53	0.820	2.255	0.283	1154	8525	146
Tombaugh 5	03:47:56.16	+59:04:12.0	143.944	3.599	8.27	2.07	0.561	0.515	-2.388	1706	9768	107
UPK 219	23:27:24.96	+65:18:36.0	114.325	3.861	8.17	1.20	1.210	-1.734	-2.459	873	8735	58
Comparison clusters												
Collinder 350	17:48:04.32	+01:31:30.0	26.952	14.773	8.77	0.52	2.708	4.965	-0.019	371	8021	94
NGC 2682	08:51:23.04	+11:48:50.4	215.691	31.921	9.63	0.07	1.135	10.986	-2.964	889	8964	470

We selected (almost) only red clump stars, not giants in general. They are a rather homogeneous type of stars, bright enough (their absolute magnitude is $M_V \sim 0 - 1$ mag, Girardi 2016) to be observed at very high-resolution in the Solar neighborhood and to relatively large distance, warm enough ($T_{\mathrm{eff}} \sim 4500 - 5700$ K, Girardi 2016) that their spectra are not too problematic, thus allowing the derivation of accurate stellar parameters and abundances. Their temperature is high enough to allow a precise abundance analysis, as opposed to cooler, upper red giant branch stars, where line crowding (in particular at near solar metallicities) may hamper accurate analyses (see for instance the discussion in Casali et al. 2020).

Table 3.1 shows information on the clusters' position (both equatorial and Galactic coordinates) and some basic parameter, such as age, distance, reddening, etc. All values come from a single homogeneous source, i.e. Cantat-Gaudin et al. (2020), where Gaia DR2 data are used to define candidate cluster members and derive cluster properties (see that paper for details).

All these OCs are located in the Galactic thin disc, cover the Galactocentric distance range 7.7-10 kpc, reside close to the Galactic midplane, and are in the age range from about 50 Myr to 4 Gyr. Figures 3.1, 3.2 show the colour-magnitude diagrams (CMD) in the Gaia system of the 18 OCs, based on the selection of Cantat-Gaudin et al. (2018); the stars are coloured with membership probability and the observed targes are indicated by larger symbols.

3.3   Observation, data reduction and radial velocities

For present samples the observations were carried out in four observing runs in December 2018, January, August, and December 2019. In most cases, multiple exposures were obtained (see Table 3.2

for details on the individual targets). The exposure times varied according to the star magnitude and the sky conditions; the goal was to reach at least a signal-to-noise ratio (S/N) of 50 at 500nm. We combined multi-exposure spectra before further data analysis.

We used the two high-resolutions spectrographs HARPS-N and GIANO in GIARPS mode. The analysis of GIANO data will be presented in forthcoming works; we deal here with the HARPS-N data. HARPS-N covers the wavelength range between 383 and 693 nm, with resolution R = 115000; this spectrograph is very well suited for determining radial velocity (RV) and abundances with very high precision.

The spectra were reduced by the HARPS-N Data Reduction Pipelines, including sky subtraction and the eliminating of telluric lines. More information of data reduction pipeline is in `http://ia2-harps.oats.inaf.it/` mentioned in Chapter 2 Sect 2.2. Spectrum continuum normalization with cubic splines and combination were done with IRAF[2]. The normalization is carried out by the task CONTINUUM. The fitting function and the order will be changed by inputting, 'func spline3' and ':order' the fitting will be updated by the key 'f', type 'q' to save the final fitting result (Fig 3.3). Because the noise of merged region is magnified by the normalization process, for avoiding this problem the process before combining are using task CONTINUUM to normalized the spectrum, then dividing the normalized spectra using SARITH, the spectra of the continuum are obtained in Fig 3.4 (they are functions that were fit to the spectra in the normalization process), then the spectrum should be merged by the task SCOMBINE, the parameter set including

Group = aperture

Combine= sum

Then the summed object spectrum is divided by the summed continuum spectrum by SARITH, and the normalized and merged spectrum is obtained.

The calculation of RV was done on the final normalized spectra with the IRAF task RVIDLINES, which measures the wavelength shift of a list of features. The task RVIDLINES measures radial velocities through spectra wavelength shift determined based on a set of clean lines. We typically used 10 lines for this purpose. Fig 3.5 shows a snapshot of the procedure. For all stars, the RV information and the error is given in Table 3.3, together with the S/N measured at 600 nm. As we selected high probability members, we find very similar RVs for stars belonging to the same cluster, which further reinforces their membership, The mean value of RVs for each cluster is quoted in Table 3.4.

All our stars except one have an RV determined with the RVS instrument on board Gaia, which observes the near-IR Ca II triplet region at resolution R=11500. These RVs and the corresponding errors, from Gaia DR2, are also presented in Table 3.3.

Figure 3.6 shows the distribution of RV offsets between the value determined in this work and that from Gaia. These offsets are generally small with an average value of -0.11 ± 1.89 km s^{-1}. Owing to our small sample we have not performed further comparison.

The few discrepant values seem probably due to the much larger errors in the Gaia RVS determinations or to binarity. Two stars in NGC 2682, namely 3 and 4 in our list, one in NGC 2437, namely 6 in our list, and one in NGC 2548, namely 4 in our list, are known binaries (Mermilliod et al., 2007, 2008; Geller et al., 2021). The only Gulliver 37 star observed shows a large Gaia RV dispersion, 8.2 km s^{-1} based on 11 transits, with an average RV of 2.5 km s^{-1}, compared to our value of -4.59 km s^{-1}. Moreover, we have in hand an optical high resolution spectrum for another project from which we derived a RV of 21.92 ± 0.02 km s^{-1} (Carrera et al. in prep.). Due to the large velocity dispersion reported by Gaia and the discrepancy among the different radial velocity determinations, we consider it as a

---

[2]IRAF is distributed by the National Optical Astronomy Observatory, which is operated by the Association of the Universities for Research in Astronomy, inc. (AURA) under cooperative agreement with the National Science Foundation.

probable spectroscopic binary. All these stars do not present doubling of their lines, so the measure of the atmospheric parameters is negligibly affected by the presence of any unseen companion with respect to the precision of our analysis.
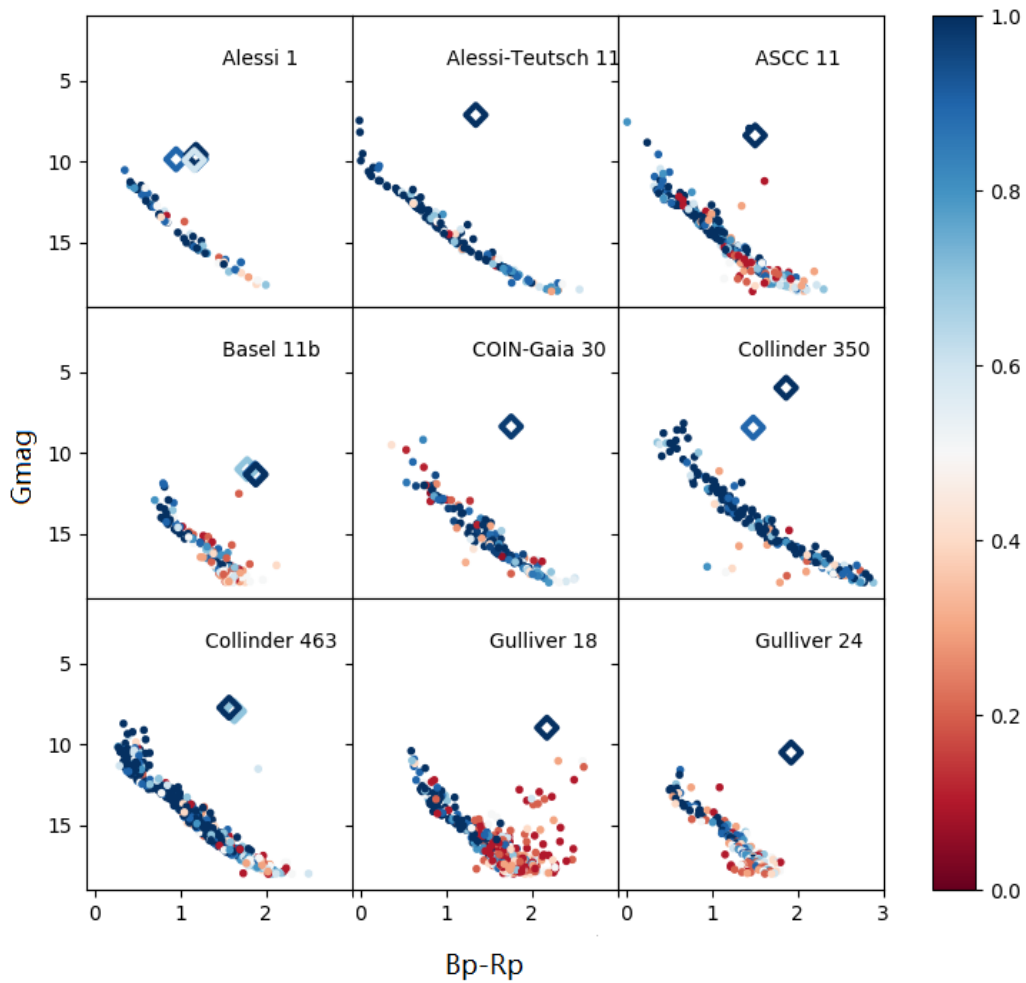
Figure 3.1: The CMDs of nine of the 18 open clusters; the dots are stars selected from Gaia DR2 database, the large diamonds are targets observed in this work. All points are coloured by membership probability (Cantat-Gaudin et al., 2018).
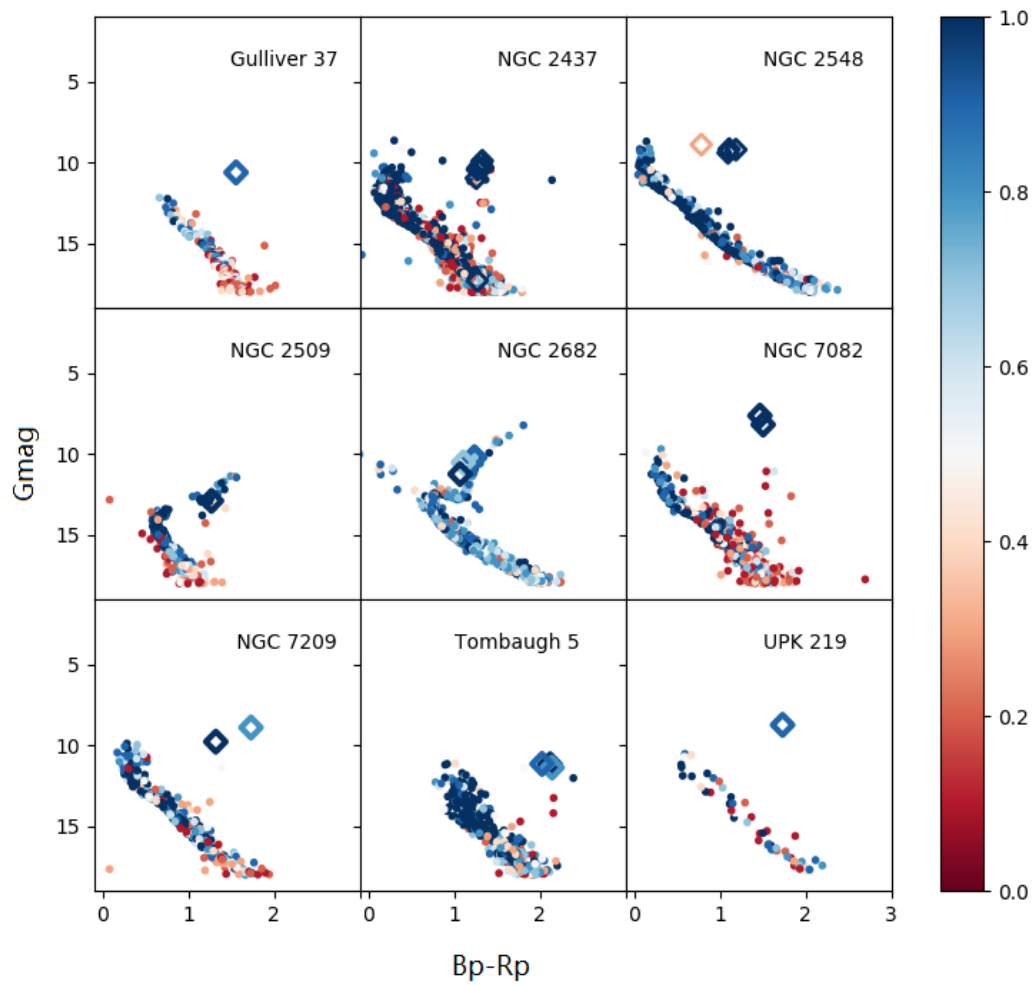
Figure 3.2: As in the previous figure, for the remaining nine clusters.
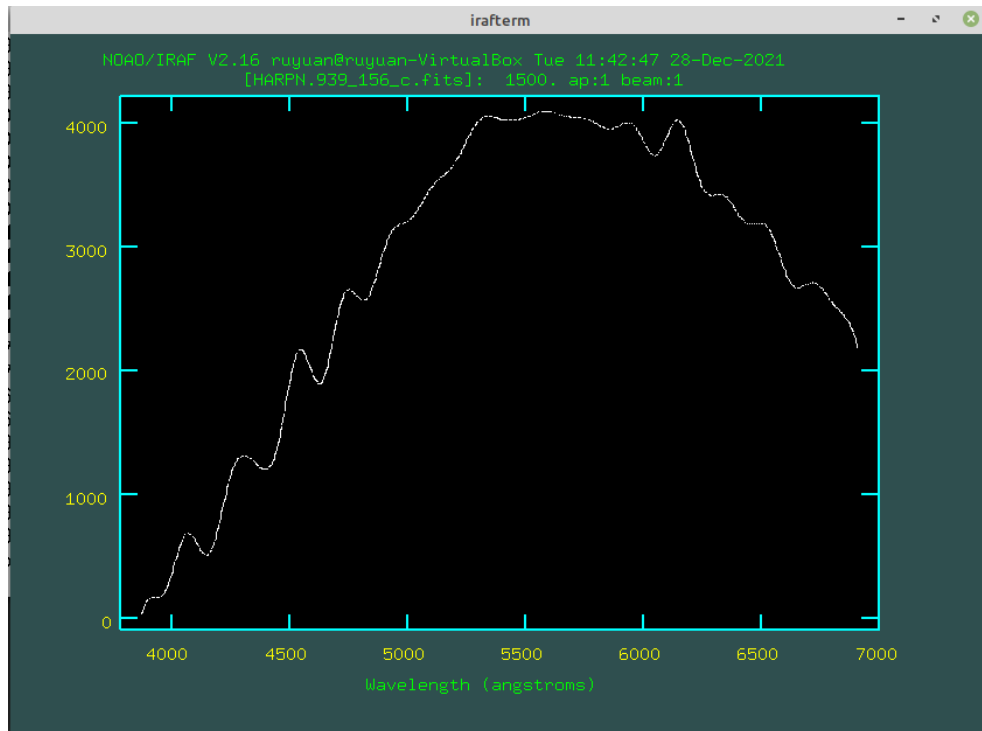
Figure 3.3: The profile of spectrum continuum
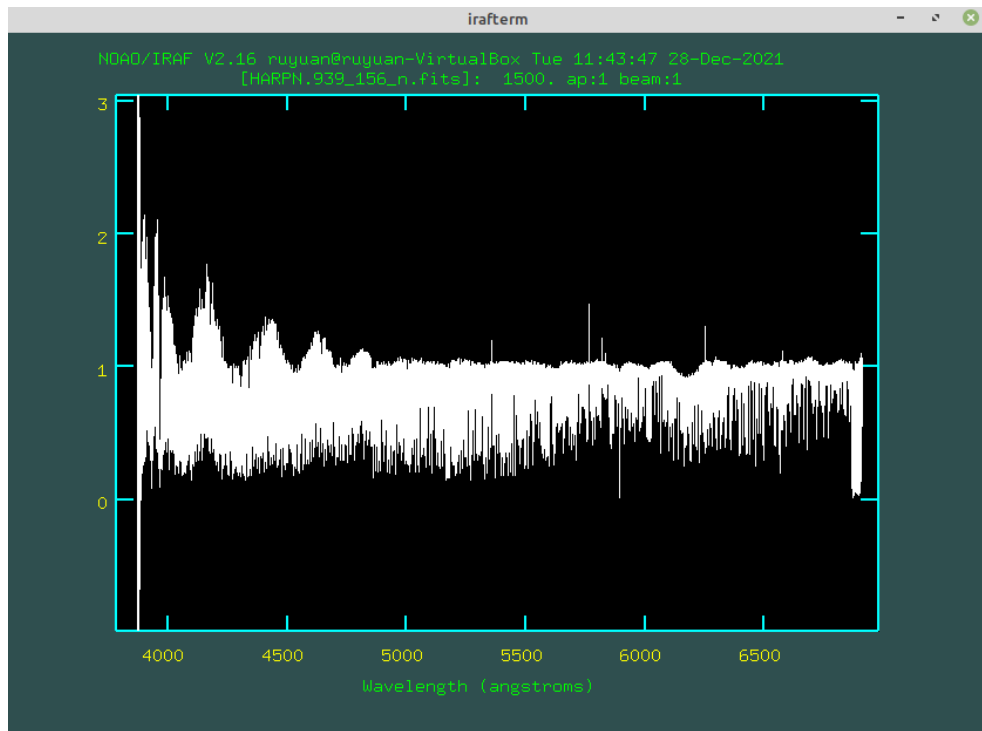
Figure 3.4: The normalized spectrum
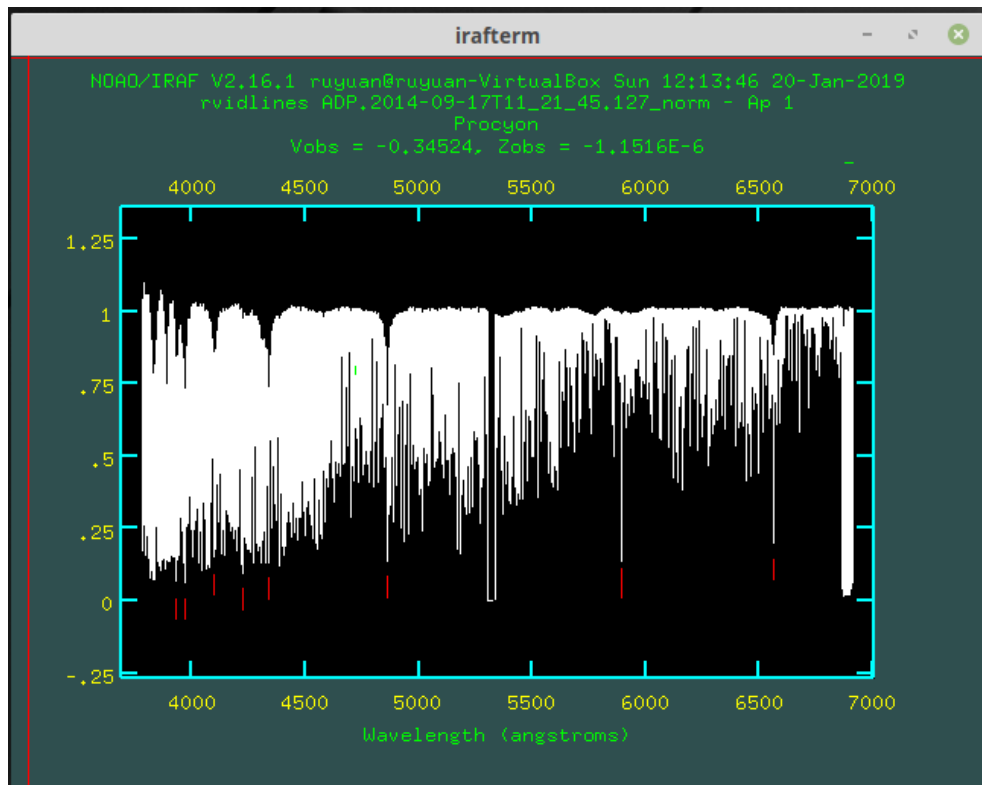
Figure 3.5: The measurement of radial velocity
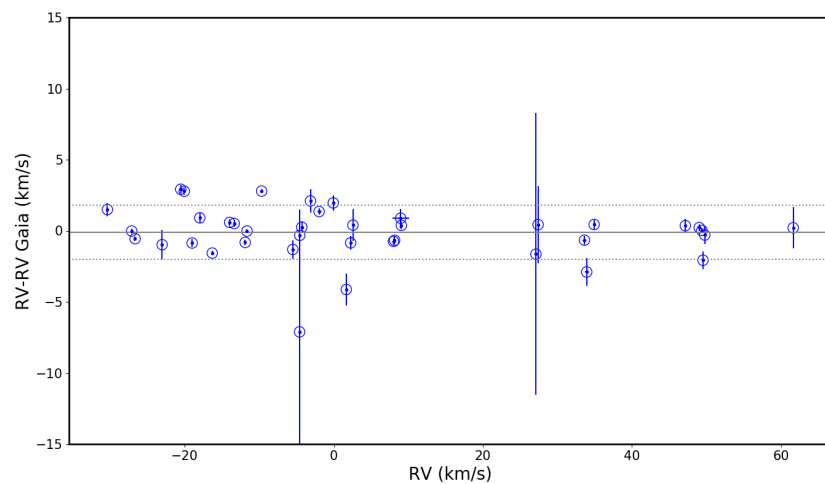
Figure 3.6: Difference in radial velocities for targets between Gaia and this work. The error of our sample is shown in the x-axis (it is so small that it falls within the symbol), and only the Gaia error is plotted on the y-axis, as it is much larger. The grey lines indicate the mean value of offset -0.11 ± 1.9 km s^{-1} (standard deviation).

Table 3.2: Observational log for our targets, along with Gaia DR2 magnitudes and colors.

Name	Gaia ID	Ra (J2000)	Dec (J2000)	Gmag	BP-RP	Obs date	MJD-Obs	exp time (s)
ASCC 11	2417304188055573760	03:32:04.87	+44:57:45.4	8.3675	1.507	2018-12-16	58468.84	1200
						2018-12-16	58468.82	1200
Alessi 1_1	4025063691360008832	00:53:15.44	+49:31:53.8	9.824	1.187	2018-12-19	58471.82	1800
						2018-12-19	58471.84	1800
Alessi 1_2	4025059911788890752	00:53:20.38	+49:28:49.7	9.808	1.176	2018-12-19	58471.87	1800
						2018-12-19	58471.89	1800
Alessi 1_3	4028675930657772288	00:54:51.06	+49:53:17.2	9.565	1.186	2018-12-18	58470.86	1500
						2018-12-18	58470.88	1500
Alessi 1_4	4028806841260588880	00:54:10.20	+49:40:08.9	7.099	1.349	2018-12-19	58471.93	1800
						2018-12-19	58471.95	1800
Alessi-Teusch 11	2184332753719499904	20:16:22.4	+52:06:18.4	7.099	1.349	2019-08-15	58710.86	690
Basel 11b_1	3424056131485038592	05:58:08.10	+21:57:44.7	10.989	1.782	2019-01-30	58513.90	3600
Basel 11b_2	3424055921028900736	05:58:10.12	+21:57:23.2	11.256	1.876	2019-01-30	58513.95	1800
						2019-01-30	58513.97	1800
						2019-01-30	58513.99	1800
Basel 11b_3	3424057540234289408	05:58:18.16	+21:58:43.7	11.320	1.884	2018-12-20	58472.19	1800
						2018-12-20	58472.21	1800
						2018-12-20	58472.24	1800
						2018-12-20	58472.26	1800
COIN-Gaia 30	5325336822286608384	01:24:05.26	+70:25:25.1	8.352	1.762	2019-12-07	58824.85	1400
Collinder 463_1	5342075555539397888	01:33:49.45	+71:51:09.6	7.946	1.632	2018-12-19	58471.80	1200
Collinder 463_2	5343630677715447680	01:45:09.15	+71:53:25.3	7.725	1.572	2018-12-17	58469.81	1200
Gulliver 18	1836389309820904064	20:11:43.9	26:35:07.0	8.964	2.178	2019-08-10	58705.88	1380
Gulliver 24	4300352497779499264	00:04:28.47	+62:42:04.4	10.494	1.927	2019-08-12	58707.15	1500
						2019-08-12	58707.16	1500
Gulliver 37	2024469226291472000	19:28:18.44	+25:22:53.4	10.592	1.559	2019-08-13	58708.94	608
						2019-08-13	58708.93	1500
NGC 2437_1	3029609393042459392	07:41:36.9	-14:26:11.2	10.277	1.338	2018-12-17	58469.08	1800

Name	ID	RA	Dec			Date	MJD	Exp
NGC 2437_2	3029202711180744832	07:41:28.52	-14:54:17.5	10.293	1.285	2018-12-17	58469.10	1800
						2018-12-17	58469.12	1800
						2018-12-17	58469.15	1800
NGC 2437_3	3030364134752459904	07:41:00.64	-14:12:08.4	10.417	1.274	2018-12-17	58469.17	1800
						2018-12-17	58469.19	1800
NGC 2437_4	3029132686034894592	07:42:47.85	-15:17:44.16	10.838	1.302	2018-12-18	58470.18	2400
						2018-12-18	58470.20	2400
NGC 2437_5	3029156222454419072	07:42:41.24	-14:59:51.4	10.948	1.262	2018-12-19	58471.17	2400
						2018-12-19	58471.20	2400
NGC 2437_6	3029207006148017664	07:41:19.42	-14:48:47.5	9.877	1.332	2018-12-18	58470.10	1500
						2018-12-18	58470.12	1500
NGC 2437_7	3029226694277998080	07:41:19.36	-14:40:59.7	9.975	1.322	2018-12-08	58470.14	1500
						2018-12-08	58470.16	1500
NGC 2509	5714209934411718784	08:00:44.36	-19:06:59.4	12.883	1.275	2019-01-15	58498.07	2400
						2019-01-15	58498.10	2400
						2019-01-15	58498.13	2400
NGC 2548_1	3064481400744808704	08:13:35.42	-05:53:02.04	9.377	1.098	2018-12-17	58469.24	1200
						2018-12-17	58469.25	1200
NGC 2548_2	3064537647636773760	08:12:37.24	-05:40:51.0	9.151	1.111	2018-12-18	58470.24	1200
						2018-12-18	58470.25	1200
NGC 2548_3	3064579703955646976	08:14:28.10	-05:42:16.09	9.187	1.190	2018-12-19	58471.23	1200
						2018-12-19	58471.25	1200
NGC 2548_4	3064486692144030336	08:13:40.44	-05:46:24.96	8.873	0.786	2018-12-17	58469.27	1800
NGC 7082_1	1972288740859811072	21:28:48.97	+47:06:54.2	8.171	1.508	2019-12-08	58825.80	1400
NGC 7082_2	1972288637780285312	21:28:34.58	+47:05:22.92	7.622	1.470	2019-12-07	58824.81	1400
NGC 7209_1	1975004019170020736	22:05:09.94	+46:31:25.3	9.766	1.323	2019-08-14	58709.14	1725
						2019-08-14	58709.16	1725
NGC 7209_2	1975002919658397568	22:05:17.63	+46:29:00.6	8.891	1.734	2019-08-14	58709.12	2070
Tombaugh 5_1	473266779976916480	03:47:30.99	+59:02:50.8	11.163	2.123	2018-12-20	58472.11	1800
						2018-12-20	58472.09	1800
						2018-12-20	58472.15	1800

Cluster	Gaia ID	RA	Dec			Date	MJD	Exp
Tombaugh 5_2	4732757822228263296	03:48:32.98	+59:15:16.56	11.366	2.147	2018-12-20	58472.13	1800
						2019-01-15	58497.06	1800
						2019-01-14	58497.04	1800
						2019-01-15	58498.00	1800
Tombaugh 5_3	4732684249409332864	03:47:46.78	+59:05:36.6	11.138	2.028	2019-01-14	58498.03	1800
						2019-01-14	58497.98	1800
						2019-01-14	58497.02	1800
UPK 219	2209440823287736064	23:30:29.72	+65:08:35.3	8.728	1.734	2019-12-08	58825.84	1400
Comparison clusters								
Collinder 350_1	4372743213795720704	17:46:24.88	+01:02:39.7	5.957	1.869	2018-08-20	58350.87	300
						2018-08-20	58350.88	300
Collinder 350_2	4372572888274176768	17:48:43.82	+01:09:51.1	8.421	1.485	2018-08-20	58350.88	1380
NGC 2682_1	604921512005266048	08:51:26.17	+11:53:51.9	10.202	1.238	2020-02-02	58881.07	1500
						2020-02-02	58881.08	1500
NGC 2682_2	604920202039656064	08:51:59.51	+11:55:04.8	10.205	1.243	2020-02-02	58881.10	1500
						2020-02-02	58881.12	1500
NGC 2682_3	604904950611554432	08:51:50.19	+11:46:06.9	10.511	1.110	2020-02-02	58881.14	1500
						2020-02-02	58881.16	1500
						2019-12-08	58825.19	1500
						2019-12-08	58825.21	1500
						2019-12-08	58825.22	1500
						2020-03-11	58919.04	1500
						2020-03-11	58919.06	1500
NGC 2682_4	604917728138508160	08:51:23.76	+11:49:49.3	11.231	1.073	2020-03-10	58918.99	1420
						2020-03-11	58919.00	1420
						2020-03-11	58919.02	1420

Table 3.3: Radial velocities of targets.

Name	Gaia ID	S/N (600nm)	RV km s^{-1}	σRV km s^{-1}	RV(Gaia) km s^{-1}	σRV(Gaia) km s^{-1}	Notes
ASCC 11	241730418805573760	93	-13.36	0.15	-13.87	0.23	
Alessi 1_1	402506369136008832	93	-5.50	0.05	-4.19	0.64	
Alessi 1_2	40250599117880752	88	-3.13	0.07	-5.23	0.81	
Alessi 1_3	402867593065772288	127	-4.57	0.20	-4.25	1.83	
Alessi 1_4	402880684126058880	120	-4.29	0.03	-4.54	0.42	
Alessi-Teusch 11	2184332753719499904	126	-27.11	0.12	-27.09	0.17	
Basel 11b_1	3424056131485038592	125	2.26	0.18	3.11	0.49	
Basel 11b_2	3424055921028900736	86	1.68	0.15	5.81	1.11	
Basel 11b_3	3424057540234289408	66	2.57	0.15	2.71	1.12	
COIN-Gaia 30	532533682228608384	93	-26.66	0.13	-26.10	0.14	
Collinder 463_1	534207555539397888	143	-9.68	0.16	-12.47	0.14	
Collinder 463_2	534363067715447680	152	-11.64	0.12	-11.62	0.14	
Gulliver 18	1836389309820904064	87	-1.97	0.18	-3.32	0.21	
Gulliver 24	430035249779499264	78	-30.37	0.16	-31.86	0.49	
Gulliver 37	2024469226291472000	78	-4.59	0.17	2.52	8.22	binary? (see text)
NGC 2437_1	3029609393042459392	64	49.77	0.11	50.07	0.61	
NGC 2437_2	3029202711180744832	111	47.16	0.14	46.80	0.50	
NGC 2437_3	3030364134752459904	95	49.02	0.17	48.80	0.25	
NGC 2437_4	3029132686034894592	128	49.93	0.15			
NGC 2437_5	3029156222454419072	50	49.37	0.17	49.34	0.17	
NGC 2437_6	3029207006148017664	72	27.12	0.17	28.76	9.91	binary
NGC 2437_7	3029226694277998080	74	49.53	0.19	51.60	0.62	
NGC 2509	5714209934411718784	128	61.63	0.14	61.42	1.45	
NGC 2548_1	3064481400744808704	125	9.06	0.14	8.68	0.29	
NGC 2548_2	3064537647636773760	138	8.16	0.03	8.83	0.31	
NGC 2548_3	3064579703955646976	77	8.01	0.04	8.76	0.22	
NGC 2548_4	3064486692144030336	94	8.98	0.10	8.10	0.67	binary
NGC 7082_1	1972288740859811072	144	-11.89	0.15	-11.07	0.19	
NGC 7082_2	1972288637780285312	151					Double lined binary
NGC 7209_1	1975004019170020736	81	-19.00	0.16	-18.14	0.27	
NGC 7209_2	1975002919658397568	161	-17.98	0.15	-18.89	0.35	
Tombaugh 5_1	473266779976916480	72	-23.03	0.15	-22.05	1.03	
Tombaugh 5_2	473275782228263296	54	-22.63	0.12	-22.84	0.26	
Tombaugh 5_3	473268424940932864	53	-20.53	0.13	-23.45	0.29	
UPK 219	2209440823287736064	81	-0.07	0.15	-2.03	0.55	
	Comparison clusters						
Collinder 350_1	4372743213795720704	240	-13.98	0.17	-14.57	0.20	
Collinder 350_2	4372572888274176768	70	-16.30	0.13	-14.73	0.16	
NGC 2682_1	604921512005266048	141	33.63	0.23	34.29	0.30	
NGC 2682_2	604920202039656064	78	34.93	0.14	34.49	0.35	
NGC 2682_3	604904950611554432	82	33.93	0.20	36.83	0.96	binary (see Tab. 4.4)
NGC 2682_4	604917728138508160	53	27.41	0.13	26.98	2.70	binary (see Tab. 4.4)

Note

NGC 2437_6 P~ 3350^d (Mermilliod et al., 2007)

NGC 2548_4 SB (Mermilliod et al., 2008)

Table 3.4: Mean RV for the observed clusters.

Cluster	RV (km s^{-1})	σRV (km s^{-1})	N
ASCC 11	-10.94	0.19	1
Alessi 1	-4.37	0.85	4
Alessi-Teusch 11	-27.11	0.12	1
Basel 11b	2.17	0.37	3
COIN-Gaia 30	-26.66	0.13	1
Collinder 463	-10.66	0.98	2
Gulliver 18	-1.97	0.18	1
Gulliver 24	-30.37	0.16	1
Gulliver 37	-4.59 [a]	0.17	1
NGC 2437	49.13[a]	0.93	7
NGC 2509	61.63	0.14	1
NGC 2548	8.41[a]	0.46	4
NGC 7082	-11.89	0.15	1
NGC 7209	-18.49	0.51	2
Tombaugh 5	-21.21	1.30	3
UPK 219	-0.07	0.15	1
Comparison clusters			
Collinder 350	-15.14	1.16	1
NGC 2682	34.28[a]	0;65	4

Note
[a] Binary systems (see Tab. 3.3).
When only 1 star is observed, σ is the error, nor the dispersion.

Chapter 4

Atmospheric parameters

The basic stellar atmospheric parameters are effective temperature (T_{eff}), surface gravity (log g), metallicity abundance ([Fe/H]), and microturbulence(V_{micro}). Those four parameters describe the basic atmosphere characteristics of individual stars:

- Effective temperature

Describe the spectral energy distributions, the spectral type (O, B, A, F, G, K, M) are indicators of atmospheric temperature ("early-type" is hotter stars and "late-type" is cooler one). T_{eff} is the temperature of a black body with the same luminosity per surface area as the star, which is defined according to the Stefan–Boltzmann law: $F_{Bol} = \sigma T_{eff}^4$. Hence, the bolometric luminosity of the star expressed as a funtion of the stellar radius R is : L=4π R$^2\sigma T_{eff}^4$. Note that Teff corresponds to the temperature at the radius at optical depth 1 in the stellar atmosphere.

- Surface gravity

Defined as g= $G\frac{M}{R^2}$, can be transformed into

$$g = \frac{M}{R^2} g_\odot,$$ (4.1)

and

$$\log g = \log M - 2 \log R + 4.437$$ (4.2)

where M and R are expressed in solar masses and radii respectively. Such direct measurement is possible in only a small fraction of stars, and the process has considerable uncertainties.

- Metallicity

Frequently referred to [Fe/H], is meant to indicate the metal content of the atmosphere. Generally measured from the strength of elements absorption lines direct. The different percentages of metallicity will change the atmospheric structure and affect stellar evolution, which makes the metallicity crucial for stellar population studies. Otherwise, iron is the most common element used to obtain the other atmospheric parameters for FGK-type stars because the dominant number of iron lines makes the determination more reliable.

- Microturbulence
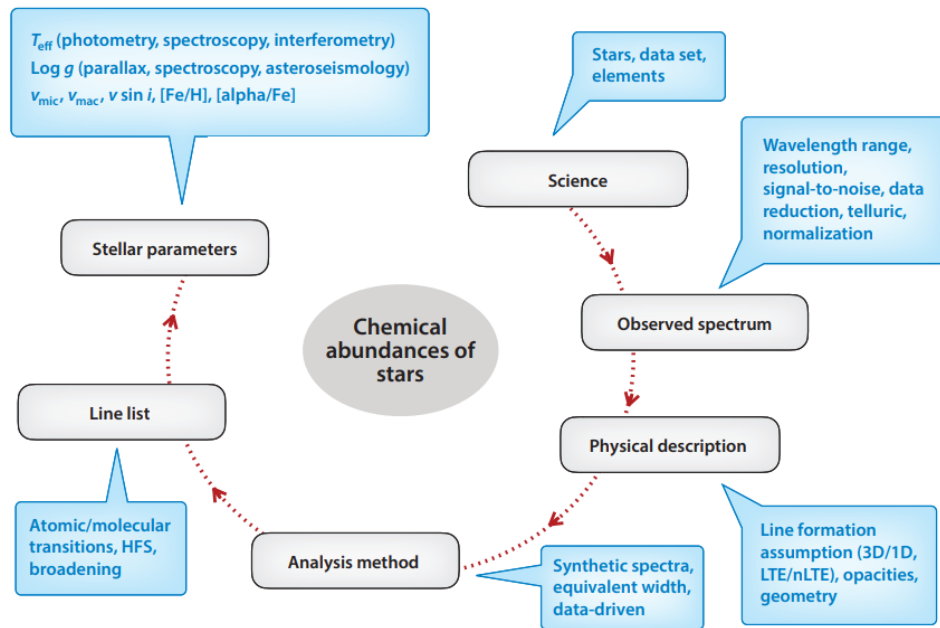
Figure 4.1: The illustration is from Jofré et al. (2019), which shows the basic step of determination of stellar parameters and chemical compositions.The uncertainties exist in each step, which may arise from different sources. (HFS: hyperfine structure, LTE: local thermodynamic equilibrium).

This parameter demonstrates the mass movement in small-scale, compared with the scale of the unit particle velocity distribution. And mainly affects the width of Gaussian shape for absorption lines, microturbulence usually as a free parameter in spectral analysis. Fig 4.1 is the process of spectrum analysis.

4.1 Derivation of atmospheric parameters from abundance analysis

Atmospheric parameters can not be directly observed, but are inferred through modeling the stellar atmosphere and the line formation process and matching the prediction for the line strengths to the measured values.

4.1.1 Initial parameters

In order to do so, a set of initial parameters to be used in the first iteration of the abundance analysis determination is needed. For this purpose, we used photometric parameters, that are determined on the basis of observed photometric colour(s) and the latest generation of stellar isochrones.

To determine the initial stellar effective temperature (T_{eff}) we used IRFM (Infrared flux method). This method is model independent and relies on the flux on the stellar surface in infrared wavelength which relates to the surface temperature. We derived the J-K colours from 2MASS, applied the appropriate reddening for the target coordinate as derived from IRSA (Schlafly & Finkbeiner, 2011). The computation of photometric surface temperature follows the colour-temperature polynomial fitting based on a sample of F0-K5 type from Alonso et al. (1999), appropriate for stars in the range 3700-5300 K, which is consistent with our sample.

To determine $\log g$ we used Padova CMD isochrones (PARSEC release v1.2s, Marigo et al. 2017 and COLIBRI, Pastorelli et al. 2020, and references therein), with web interface CMD 3.4. The initial log g can be estimated when the age (Cantat-Gaudin et al., 2020) and metallicity inputed in the CMD isochrones.

For age and metallicity input for the isochrones we used information taken from the literature (see Table 3.1). In case no estimate of metallicity was available, we adopted the average metallicity of the thin disc ([Fe/H] = -0.25dex Soubiran et al. 2003). This is admittedly low for the typical OC, however it has a negligible impact on the final parameters in Table 4.1.

In fact, while it is important to provide reasonably accurate input parameters in the isochrones to derive similarly reasonable photometric parameters, these values are just the starting point to build the initial model atmosphere. The actual atmospheric parameters have been determined on the basis of the observed spectra.

4.1.2 Line list and equivalent widths measurements

We adopted the line list for Fe ɪ from Ruffoni et al. (2014) and Fe ɪɪ from Meléndez & Barbuy (2009), selecting the lines in the 430 to 640 nm interval. HARPS-N spectra start from 383 nm; however, the S/N is quite low in that region for our spectra. This fact, combined with the extreme crowding of features in the blue part of the spectrum, led us to discard all Fe lines bluer than 430 nm, as their intensity could not be measured with the same accuracy of those in redder regions.

Equivalent widths (EWs hereafter) were measured with the code ARES, following the procedure described in Sousa et al. (2015), using a S/N dependent approach to set the local continuum. Visual inspection was performed for very strong lines (EW > 150mÅ) and lines with large fitting errors (EW < 3×σ(EW)) and we performed a manual measurement of the EW using *IRAF splot* when the inspection showed an issue with the ARES fitting (e.g. incorrect continuum placing due to a badly subtracted cosmic ray). Lines which turned out to be blended were discarded.

4.1.3 Determination of the parameters

The atmospheric parameters analysis was performed using the code MOOG (used through the python wrapper pymoogi[1], based on the MOOG 2019 version), a 1D, Local Thermodynamic Equilibrium (LTE) stellar line analysis code. The model atmospheres were calculated interpolating the ATLAS9 stellar atmosphere library (Castelli & Kurucz, 2003) in 1D plane-parallel geometry. While in principle spherical models should be better for giants, in practice this choice does not introduce significant differences (see e.g. Casali et al., 2020).

Atmospheric parameters were determined iteratively, by varying their values in the input model atmosphere until excitation and ionisation equilibria were reached.

In other words, T_{eff}'s and microturbulent velocities (v_{micro}) were determined by minimising the trends of Fe I abundance as determined from different lines as a function of their excitation potential and their intensity, respectively; surface gravity was determined by matching (within the errors) output Fe I and Fe II abundances. While we adopt the solar abundances from Asplund et al. (2009), we have also repeated the procedure for a solar spectrum collected with HARPS-N during one of our runs, finding an Fe abundance essentially identical to that reported in Grevesse & Sauval (1998). Errors on the atmospheric parameters were derived following the same procedure outlined in Section 4.1.4.

---

[1]https://github.com/madamow/pymoogi

The resulting atmospheric parameters along with their associated uncertainties are reported in Table 4.2 for all individual targets. The mean value of metallicity for each cluster is quoted in Table 4.3 (where, for Collinder 350, we use only the warmer star).

4.1.4 Precision of stellar parameters

The random error mainly contains the uncertainties from the spectra to be analyzed, including the signal-to-noise ratio, the qualities of data reduction, and the instrumental effects. For instance, the value of the signal to noise ratio affected the result of stellar parameters and chemical abundance directly, some work investigated this problem using the spectra from the same instrument with different S/N.

Systematics uncertainties are on the other hand not due to chance but rather to differences introduced in the derivation/measurement procedure. In this context, the adopted temperature scale, the line list, or the class of model atmospheres can all lead to systematic errors in the analysis. This can result in offsets among different studies, which, while internally homogeneous, might have systematic differences in the derived parameters (and abundances) due to different sets of assumptions.

For the derivation of the uncertainties associated to the stellar parameters we adopt the approach in Epstein et al. (2010).

Considering the following quantities:

O_1: slope of the log (Fe I) versus E.P.

O_2: slope of log (Fe I) versus log (EW/λ)

O_3: | log(Fe I)-log(Fe II)| (derived FeI and FeII)

O_4: |[Fe/H]$_{output}$-[Fe/H]$_{input}$| (where input is the [Fe/H] of the model atmosphere)

As temperature is derived flattening the slope O_1, the error T_{eff} is derived considering the error on the derived slope, based on the scatter of the abundance of Fe I lines. The procedure is analogous for microturbulence, that is also derived by flattening the slope of O_2, with uncertainties are corresponding to the error of the fit.

The surface gravity measurement is based on the gas pressure part related to Saha equation, the ion equilibrium assumption requests the abundance of the elements derived from neutral lines are compatible with that from ionized lines, within their respective random uncertainties. The range is reasonable when Eq.4.3 satisfied.

$$O_3 < \frac{\sigma_{FeII}}{\sqrt{N}} + \frac{\sigma_{FeI}}{\sqrt{N}} \tag{4.3}$$

which is used to define the acceptable log g range and hence the uncertainty (semiamplitude of the difference between the maximum and minimum acceptable log g).

The equation:

$$O_4 < \frac{\sigma_{FeI}}{\sqrt{N}} \tag{4.4}$$

is used to define the acceptability range of the metallicity of the model atmosphere, and its semiamplitude is the uncertainty associated with such value.

The error on the Fe abundance is derived combining the uncertainty arising from line-to-line scatter and that due to the uncertainties of T_{eff}, log g and v_{micro}, and on the model atmosphere metallicity, which are derived by changing the parameters (one at a time) by the corresponding uncertainty and repeating the Fe abundance derivation.

4.1.5 Comparison with literature

Two clusters, namely Collinder 350 and NGC 2682 (M67) have been included in the present sample for comparison purpose. The former has been investigated in a previous SPA paper (Casali et al., 2020), which reports results obtained with a slightly different approach for the same stars, therefore allowing the mapping of possible offsets. The latter, NGC 2682, is one of the most studied OCs and represents an ideal benchmark cluster. A few more clusters have some recently published analyses. One of them was purposely observed (Tombaugh 5) as the existing spectra were of moderate-resolution; for two more (Basel 11b, NGC 2548) the results were published after our observations had already been taken. Finally, we note that some other clusters (ASCC 11, Alessi-Teusch 11, Collinder 350, NGC 2548, and NGC 2682) were observed within the LAMOST survey, at R=1800 (Zhang et al., 2019).

However, we will not discuss this last case, limiting comparisons only to spectra with at least moderate resolution (R> 10000).

We give details below and briefly summarise how our results compare to literature. In particular, Fig. 4.2 gives a visual comparison, while Tab. 4.4 presents detailed values for the benchmark cluster NGC 2682 and the other stars. We remark that, for NGC 2682, there are no systematic differences among the different studies.

Collinder 350 - In our sample, we collected and analysed spectra for two members of Collinder 350, one of the least studied open clusters in the solar neighborhood. For the coolest star (4200 K) we obtained [Fe/H]=−0.40 ± 0.08 dex, while for the hottest (5300 K) we found [Fe/H]=0.00 ± 0.05 dex. In the work of Blanco-Cuaresma & Fraix-Burnet (2018), the metallicity was estimated at 0.03 dex from the spectrum of one single star with a resolution about 80,000. In the SPA paper by Casali et al. (2020), the value of [Fe/H] was measured using two methods on the same stars as in our analysis. Even in this case the two stars show a difference in the measured metallicity, even if smaller than in the present analysis. With ROTFIT (i.e. fitting of spectral libraries) they get 0.03 ± 0.07 dex (cooler star) and −0.02 ± 0.09 dex (hotter star) while with FAMA (i.e. automatic method based on EWs analysis) they derive −0.24 ± 0.02 dex (cooler star) and −0.03 ± 0.06 dex (hotter star).

Comparing to the present paper, the results are overall in fair agreement. The hotter star shows [Fe/H]=0, a value consistent with that from both methods in Casali's work. For the cooler star, our result is more metal poor than that measured by Casali's paper using either method. Casali et al. (2020) ascribes the differences in the quantities derived with FAMA and ROTFIT to the challenges posed by placements of the continuum in these stars, as they are very rich in absorption lines, leading to the less accurate metallicities for star with low temperature (T_{eff} < 4300 K, *log* g < 1.8 dex). Collinder 350_1 has RV in good agreement with Gaia, while Collinder 350_2 shows a difference from the Gaia value, hinting at the possibility that the object has an undetected companion, which might also have affected the parameter determinations, possibly more when using automated approaches. We also note that Cantat-Gaudin et al. (2018) indicates very high membership probability (¿ 0.9) for both objects.

NGC 2682 (M67) - This is one of the most studied open clusters and has solar metallicity and age (see e.g. Bertelli Motta et al., 2018; Bossini et al., 2019). We observed four stars, two on the red clump and single, and two red giants known to be binary systems (see Tables 3.3 and 4.4). In particular, the two single-lined binaries (stars 3, 4 in our list) were studied by Mermilliod et al. (2007, 2008) and Geller et al. (2021), who derived their orbital parameters. Star NGC 2682 3 (aka S1237) is a yellow straggler (Leiner et al., 2016), i.e. a star falling between the blue stragglers (BSS) and the red giants, above the subgiant branch level in optical CMDs. Leiner et al. (2016) used Kepler K2

data to derive a mass of 2.9±0.2 $M_\odot$, about twice the mass of turn-off stars, corroborating the notion that yellow stragglers are a later evolutionary phase of BSS. We collected results of spectral analysis from multi-work and list them in Table 4.4. The parameters are in overall good agreement with the literature.

Tombaugh 5 -   A metallicity estimate based on moderate-resolution spectroscopy also exists for Tombaugh 5. Baratella et al. (2018) reported atmospheric parameters (from mid-res spectra, R=13 000) for five members out of seven observed. In this case two stars are in common with our sample, as they were targeted on purpose. However, only one (Tombaugh 5_1 for us, 7701 in Baratella et al. 2018) is analyzed in both papers, as they considered the second (Tombaugh 5_2 for us, 8099 in Baratella et al. 2018) a possible non member on the basis of its RV and previous literature. The latter star has a high probability of being a member according to Cantat-Gaudin et al. (2018) and the RVs measured by us and Gaia RVS upport its membership. In Baratella et al. (2018) temperature and gravity were derived spectroscopically and abundances were measured using EWs, with estimated errors of 0.15-0.20 dex. They found an average metallicity of 0.06 ± 0.11 dex. The mean value from our analysis is 0.05 ± 0.05 dex. The agreement between the analyses for all atmospheric parameters is reasonable, given the large difference in resolution between the data sets (see Fig. 4.2).

NGC 2548 -   A recent paper Sun et al. (2020) is based on moderate-resolution spectra. They report the radial and rotational velocities for nearly 300 stars in NGC 2548 (M48), measured with Hydra@WIYN spectra (R~13500) in a region about 40 nm wide, around the Li ɪ 670.8 nm line. The candidate cluster stars were selected from CMDs based on UBVRI photometry and about two thirds resulted member, both single or in binary/multiple systems, combining the spectroscopic data and Gaia DR2 results. Temperature and gravity were derived from photometric data. For a subsample of 99 well behaved, low rotational velocity, single cluster members, the value of the metallicity was derived using 16 Fe ɪ lines, finding an average metallicity [Fe/H]=−0.06 ± 0.007 dex. This is in agreement with −0.02 ± 0.04 dex from 4 stars in our work.

Two stars are in common, for which Sun et al. (2020) report T_{eff}'s of 4912 K and 4549 K, with $\log g$ 4.64 and 4.69 respectively. We obtained T_{eff}'s 5370±110 K and 4930±60 K and our values for $\log g$ are much lower, 3.67±0.1 dex and 2.68±0.05 dex respectively, consistent with the stars being evolved rather than in the main sequence. The gravities in Sun et al. (2020) are derived using the Yale-Yonsei isochrones, an approach that leads to two possible solutions, corresponding to an evolved or a main sequence star. Sun et al. (2020) adopted the dwarf solution, and the reason behind this choice is not discussed in the paper. However, given the position on the CMD of the observed stars (see Fig. 3.2), we expect that the solution corresponding to an evolved (and thus brighter) star is the most appropriate one.

Basel 11b -   Finally, among the 128 OCs published in Donor et al. (2020) and based on SDSS/APOGEE DR16, there is Basel_11b. The paper presents the metallicity based on one single star, [Fe/H]=0. For this star we determined [Fe/H]=-0.04 and the mean iron abundance, based on 3 stars, is of −0.013 ± 0.034 dex.

Further details on the comparison of atmospheric parameters is found in Tab. 4.4.

Table 4.1: Initial parameters from photometric data.

Name	T_{eff} (K)	log g (dex)	[Fe/H] (dex)	v_{micro} (km s^{-1})
ASCC 11	4867	2.36	-0.25	1.0
Alessi 1_1	4677	2.39	-0.25	1.0
Alessi 1_2	4600	2.28	-0.25	1.0
Alessi 1_3	4804	3.50	-0.25	1.0
Alessi 1_4	4578	2.25	-0.25	1.0
Alessi-Teusch 11	4790	3.40	0.10	1.0
Basel 11b_1	6259	1.70	0.01	1.0
Basel 11b_2	5917	1.59	0.01	1.0
Basel 11b_3	5693	1.83	0.01	1.0
COIN-Gaia 30	5231	1.70	-0.25	1.0
Collinder 463_1	4730	2.12	-0.25	1.0
Collinder 463_2	4730	2.30	-0.25	1.0
Gulliver 18	4598	1.50	-0.25	1.0
Gulliver 24	4567	1.62	-0.25	1.0
Gulliver 37	5095	1.80	-0.25	1.0
NGC 2437_1	4792	2.24	0.00	1.0
NGC 2437_2	5218	3.38	0.00	1.0
NGC 2437_3	5206	3.38	0.00	1.0
NGC 2437_4	5087	2.39	0.00	1.0
NGC 2437_5	4990	2.37	0.00	1.0
NGC 2437_6	4848	2.29	0.00	1.0
NGC 2437_7	4549	1.95	0.00	1.0
NGC 2509	4705	2.27	0.00	1.0
NGC 2548_1	5114	2.50	-0.24	1.0
NGC 2548_2	5047	2.50	-0.24	1.0
NGC 2548_3	4853	2.35	-0.24	1.0
NGC 2548_4	5327	2.70	-0.24	1.0
NGC 7082	4994	1.56	-0.01	1.0
NGC 7209_1	4799	2.50	0.01	1.0
NGC 7209_2	4142	1.50	0.01	1.0
Tombaugh 5_1	5024	2.42	0.06	1.0
Tombaugh 5_2	5021	2.40	0.06	1.0
Tombaugh 5_3	5270	2.44	0.06	1.0
UPK 219	5203	3.01	-0.25	1.0
Comparison clusters				
Collinder 350_1	4200	1.30	0.10	1.0
Collinder 350_2	5300	3.20	0.10	1.0
NGC 2682_1	4537	3.61	0.00	1.0
NGC 2682_2	4601	2.50	0.00	1.0
NGC 2682_3	4823	2.90	0.00	1.0
NGC 2682_4	4967	3.36	0.00	1.0

Table 4.2: Final atmospheric parameters. $\sigma_1[Fe/H]$ is the uncertainty associated to line scatter, $\sigma_2[Fe/H]$ is the total uncertainty.

Name	Gaia ID	T_{eff} (K)	$\sigma\,T_{eff}$	log g (dex)	σ log g	[Fe/H] (dex)	σ_1 [Fe/H]	σ_2 [Fe/H]	log ϵ Fe I	std	Nlines Fe I	log ϵ Fe II	std	Nlines Fe II	v_{micro} (km s⁻¹)	σ v_{micro}
ASCC 11	2417304188055573760	5250	70	2.15	0.10	-0.14	0.05	0.06	7.360	0.159	46	7.360	0.210	10	2.4	0.3
Alessi 1_1	4025063691360008832	5000	70	2.65	0.15	-0.10	0.05	0.05	7.392	0.181	74	7.391	0.136	16	1.5	0.1
Alessi 1_2	4025059917889075 2	5200	70	3.20	0.10	0.08	0.10	0.10	7.583	0.135	75	7.587	0.128	15	1.5	0.2
Alessi 1_3	4028675930657772288	5250	65	3.27	0.10	0.07	0.06	0.06	7.576	0.105	75	7.575	0.098	15	1.6	0.1
Alessi 1_4	402880684126058880	5120	60	3.09	0.06	-0.05	0.10	0.10	7.470	0.122	72	7.476	0.089	16	1.6	0.1
Alessi-Teusch 11	2184332753719499904	4560	50	2.10	0.15	-0.19	0.05	0.05	7.310	0.172	75	7.311	0.219	16	2.1	0.2
Basel 11b_1	3424056131485038592	5180	50	3.15	0.13	0.00	0.05	0.05	7.500	0.093	68	7.507	0.127	13	2.2	0.1
Basel 11b_2	3424055921028900736	5220	30	3.07	0.10	0.02	0.03	0.03	7.525	0.141	72	7.529	0.135	15	2.2	0.2
Basel 11b_3	3424057540234289408	4950	50	2.83	0.10	-0.04	0.05	0.05	7.464	0.136	77	7.467	0.116	15	2.1	0.1
COIN-Gaia 30	53253368228608384	5200	50	3.40	0.05	0.03	0.05	0.05	7.538	0.158	71	7.552	0.163	15	2.3	0.2
Collinder 463_1	534207555539397888	4730	30	2.12	0.10	-0.20	0.05	0.05	7.310	0.130	72	7.310	0.180	16	2.5	0.1
Collinder 463_2	534363067715447680	4730	30	2.30	0.15	-0.10	0.05	0.05	7.410	0.131	70	7.410	0.207	16	2.4	0.1
Gulliver 18	1836389309820904064	4590	100	2.60	0.17	-0.10	0.04	0.05	7.409	0.212	76	7.395	0.281	16	2.8	0.3
Gulliver 24	43003524979499264	4450	50	2.50	0.15	-0.18	0.03	0.03	7.317	0.145	74	7.316	0.240	16	2.0	0.2
Gulliver 37	2024469226291472000	4850	50	3.65	0.12	0.10	0.03	0.04	7.602	0.213	62	7.604	0.403	10	0.8	0.6
NGC 2437_1	3029609393042459392	5050	50	2.77	0.12	0.04	0.05	0.05	7.546	0.142	64	7.548	0.109	12	2.1	0.1
NGC 2437_2	3029202711180744832	5250	75	3.32	0.10	0.07	0.05	0.05	7.572	0.140	62	7.578	0.171	13	2.2	0.2
NGC 2437_3	3030364134752459904	5300	110	3.13	0.10	-0.05	0.05	0.05	7.450	0.176	62	7.447	0.149	13	2.3	0.2
NGC 2437_4	3029132686034894592	5085	65	2.90	0.10	0.00	0.05	0.05	7.508	0.111	62	7.498	0.089	15	1.7	0.1
NGC 2437_5	3029156222454419072	5030	75	2.85	0.15	0.00	0.10	0.10	7.503	0.163	74	7.505	0.161	16	1.7	0.1
NGC 2437_6	3029207006148017664	4990	65	2.72	0.10	0.00	0.05	0.06	7.443	0.238	72	7.444	0.266	15	2.1	0.1
NGC 2437_7	3029226694277998080	4650	90	2.27	0.20	-0.07	0.08	0.08	7.440	0.216	73	7.440	0.272	16	1.2	0.1
NGC 2509	5714209934411718784	4705	40	2.53	0.20	-0.10	0.05	0.06	7.394	0.213	72	7.392	0.330	16	1.5	0.3
NGC 2548_1	3064481400744808704	5370	70	3.67	0.15	0.00	0.05	0.05	7.507	0.131	60	7.504	0.155	15	2.0	0.2
NGC 2548_2	3064537647636773760	5050	50	2.65	0.10	-0.02	0.04	0.04	7.479	0.068	62	7.480	0.101	15	1.6	0.1
NGC 2548_3	3064579703955646976	4930	50	2.70	0.10	-0.01	0.05	0.05	7.490	0.079	61	7.491	0.083	13	1.6	0.1
NGC 2548_4	3064486692144030336	5200	50	3.18	0.10	-0.07	0.07	0.07	7.434	0.110	62	7.439	0.142	14	0.4	0.1
NGC 7082	1972288740859811072	4994	50	2.25	0.1	-0.15	0.05	0.07	7.360	0.144	63	7.361	0.199	12	3.0	0.2
NGC 7209_1	1975004019170020736	4880	50	2.35	0.15	0.00	0.03	0.07	7.439	0.110	74	7.433	0.155	16	1.7	0.2
NGC 7209_2	1975002919658397568	4600	30	2.79	0.15	-0.07	0.05	0.05	7.433	0.136	67	7.435	0.316	16	2.5	0.2
Tombaugh 5_1	4732667799976916480	5010	50	3.17	0.15	0.04	0.05	0.05	7.543	0.166	72	7.546	0.185	15	2.2	0.1
Tombaugh 5_2	473275782228263296	4900	50	2.31	0.1	-0.07	0.05	0.01	7.438	0.080	74	7.436	0.073	14	2.0	0.2
Tombaugh 5_3	4732667799976916480	5150	50	3.08	0.15	0.07	0.05	0.05	7.570	0.095	69	7.576	0.147	15	2.2	0.2
UPK 219	2209440823287736064	5203	150	3.01	0.10	0.02	0.05	0.05	7.528	0.166	74	7.530	0.283	16	2.7	0.2
Collinder 350_1	4372743213795720704	4200	50	1.30	0.20	-0.40	0.08	0.08	7.120	0.149	71	7.130	0.256	16	2.2	0.1
Collinder 350_2	4372572888274176768	5300	50	3.15	0.1	0.02	0.05	0.05	7.521	0.079	71	7.526	0.095	15	1.6	0.1
NGC 2682_1	604921512005266048	4687	50	2.37	0.07	-0.05	0.05	0.05	7.454	0.174	75	7.453	0.181	16	1.5	0.2
NGC 2682_2	604920202039656064	4900	110	2.76	0.1	0.02	0.05	0.05	7.520	0.132	69	7.528	0.168	15	1.7	0.2
NGC 2682_3	604904950611554432	5000	50	2.77	0.1	-0.03	0.03	0.03	7.467	0.096	67	7.467	0.082	14	1.2	0.2
NGC 2682_4	604917728138508160	5195	50	3.25	0.10	0.00	0.05	0.03	7.501	0.108	67	7.502	0.164	14	1.3	0.2
SUN		5770	40	4.44	0.08	-0.03	0.03	0.03	7.477	0.077	76	7.477	0.083	16	1.0	0.1

Table 4.3: Mean metallicity for the observed clusters.

Cluster	[Fe/H] (dex)	σ[Fe/H] (dex)	N
ASCC 11	-0.14	0.05	1
Alessi 1	0.00	0.08	4
Alessi-Teusch 11	-0.19	0.05	1
Basel 11b	-0.01	0.05	3
COIN-Gaia 30	0.03	0.05	1
Collinder 463	-0.15	0.05	2
Gulliver 18	-0.10	0.05	1
Gulliver 24	-0.10	0.05	1
Gulliver 37	0.10	0.05	1
NGC 2437	0.00	0.04	7
NGC 2509	-0.10	0.06	1
NGC 2548	-0.02	0.03	4
NGC 7082	-0.15	0.05	1
NGC 7209	-0.04	0.04	2
Tombaugh 5	0.05	0.05	3
UPK 219	0.02	0.05	1
Comparison clusters			
Collinder 350	0.00	0.05	1
NGC 2682	0.03	0.03	4
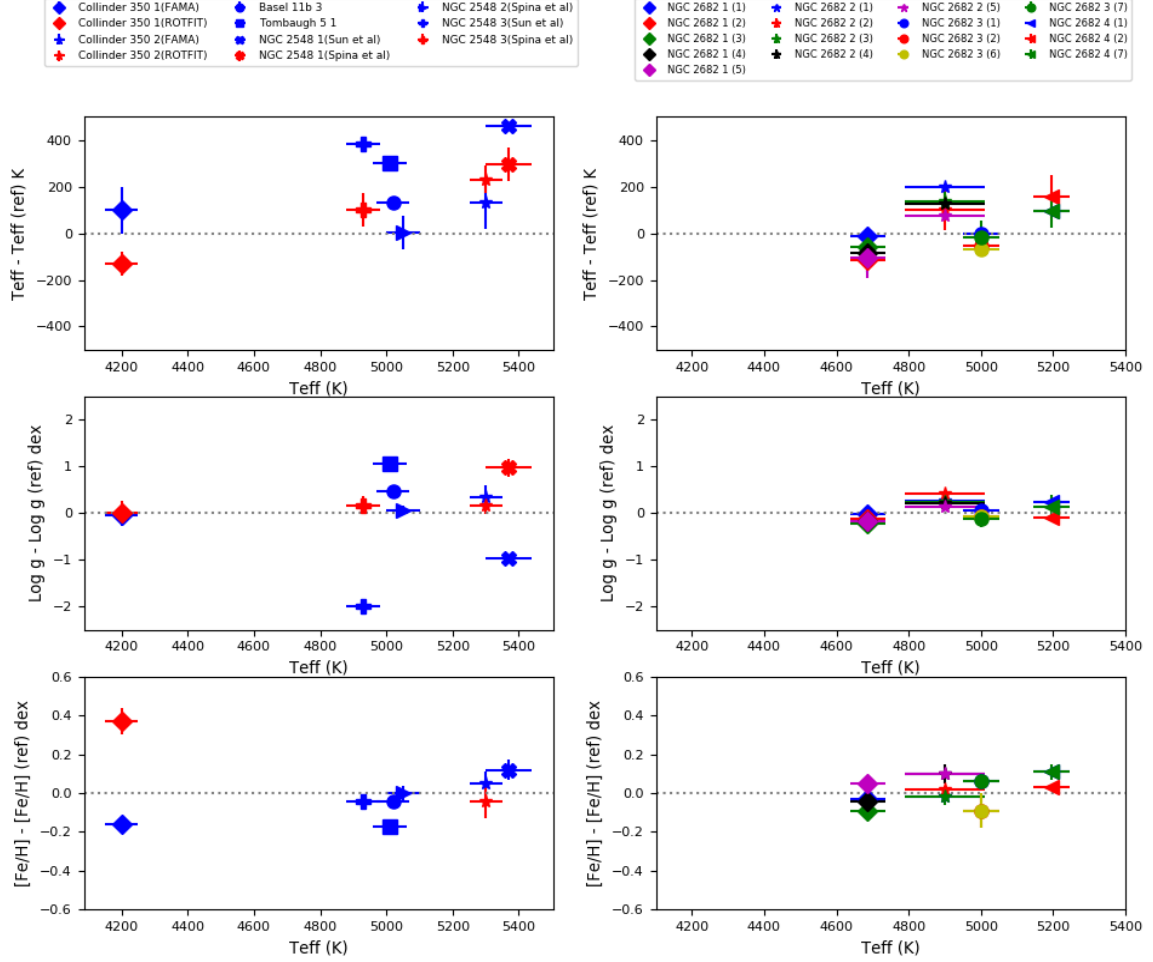
Figure 4.2: Comparison of atmospheric parameters for targets with high resolution spectroscopic determinations. We plot out T_{eff} in the x axis and the difference (our minus literature) and the error from literature on the y-axis. In the right column we show the different sources in NGC 2682 and in the left column all other clusters. Ref: (1) Jacobson et al. (2011); (2) APOGEE DR16; (3) (Casamiquela et al., 2017) EW; (4) Casamiquela et al. (2017) SS; (5) Gao et al. (2018); (6) Luck (2015);(7) Spina et al. (2021)

Table 4.4: Comparison of atmospheric parameters with literature.

star	T_{eff} (K)	σT_{eff}	log g (dex)	σlog g	[Fe/H] (dex)	σ[Fe/H]	Reference
NGC 2682_1	4687	50	2.37	0.07	-0.05	0.05	Present study
	4700		2.40		-0.02		Jacobson et al. (2011)
	4803	84	2.48	0.04		0.01	APOGEE DR16
	4745	57	2.59	0.09	0.04	0.04	Casamiquela et al. (2017) EW
	4771	13	2.55	0.03	-0.04	0.05	Casamiquela et al. (2017) SS
	4793		2.55		-0.10		Gao et al. (2018)
NGC 2682_2	4900	110	2.76	0.10	0.02	0.05	Present study
	4700		2.50		0.04		Jacobson et al. (2011)
	4802	84	2.34	0.04	0.00	0.01	APOGEE DR16
	4762	37	2.53	0.07	0.04	0.04	Casamiquela et al. (2017) EW
	4776	13	2.54	0.03	-0.08	0.05	Casamiquela et al. (2017) SS
	4824		2.62		-0.08		Gao et al. (2018)
NGC 2682_3	5000	50	2.77	0.10	-0.03	0.03	Present study
	5000		2.70		-0.09		Jacobson et al. (2011)
	5056		2.85		0.06	0.09	APOGEE DR16
	5067		2.85		0.06	0.09	Luck (2015)
	5018	71	2.88	0.19	-0.09	0.04	Spina et al. (2021)
NGC 2682_4	5195	50	3.25	0.10	0.00	0.05	Present study
	5100		3.00		-0.11		Jacobson et al. (2011)
	5040	92	3.34	0.06	-0.03	0.01	APOGEE DR16
	5098	71	3.12	0.26	-0.11	0.04	Spina et al. (2021)
Collinder 350_1	4200	50	1.30	0.20	-0.40	0.08	Present study
	4100	100	1.35	0.23	-0.24	0.01	Casali et al. (2020) FAMA
	4330	50	1.28	0.24	-0.03	0.07	Casali et al. (2020) ROTFIT
Collinder 350_2	5300	50	3.15	0.10	0.02	0.05	Present study
	5170	110	2.85	0.27	-0.03	0.06	Casali et al. (2020) FAMA
	5070	60	2.99	0.19	-0.02	0.09	Casali et al. (2020) ROTFIT
Basel 11b_3	4950	50	2.83	0.10	-0.04	0.05	Present study
	4817	86	2.37	0.04	0.00	0.01	APOGEE DR 16
Tombaugh 5_1	5010	50	3.17	0.15	0.04	0.05	Present study
	4710		2.10		0.21	0.05	Baratella et al. (2018)
NGC 2548_1	5370	70	3.67	0.15	0.00	0.05	Present study
	4912		4.64				Sun et al. (2020)
	5074	73	2.69	0.19	-0.12	0.05	Spina et al. (2021)
NGC 2548_2	5050	50	2.65	0.10	-0.02	0.04	Present study
	5049	72	2.59	0.10	-0.02	0.04	Spina et al. (2021)
NGC 2548_3	4930	50	2.70	0.10	-0.01	0.05	Present study
	4549		4.69				Sun et al. (2020)
	4829	72	2.53	0.19	0.03	0.04	Spina et al. (2021)

NGC 2682_1 RC, single

NGC 2682_2 RC, single

NGC 2682_3 SB1, $P \sim 700^d$ (Geller et al. 2021) yellow straggler (Leiner et al. 2016)

NGC 2682_4 SB1, $P \sim 43^d$ (Mermilliod et al. 2007

Basel 11b_3 2M05581816+2158437

$\sigma[Fe/H]$ is the error from metallicity measurement for present study;

EW is the result obtained by the equivalent widths-based GALA software;

SS is the results obtained from spectral synthesis using iSpec

Chapter 5

Chemical composition

Once the atmospheric parameters are derived, the chemical composition of the stars can be probed through the study of their spectra.Throughout the paper we use the standard spectroscopic notation, that is, for any given species X, $[X] = \log \epsilon(X)_{star} - \log \epsilon(X)_{\odot}$, $[X/Fe] = [X/H] - [Fe/H]$, and $\log \epsilon(X) \equiv A(\epsilon) = \log(N_X/N_H) + 12.0$ for absolute number density abundances.

5.1 Line list and EWs measurement

The optical spectral allows determining the full elements that contain iron-peak elements, α-elements, and neutron-capture elements. However, abundances for Li, Na, Al, and α-elements O, Mg, Si, Ca, and Ti are presented in this chapter.

We used a combination of spectral synthesis (Li) and EW based analysis (Na, Al, O, Mg, Ca and Ti) to derive the abundances. Li is measured with spectral synthesis. As Li abundance is easily destroyed in the giant phase and has a shallow profile, often only an upper limit can be set Li with spectral synthesis (SS) analysis. Yoichi et al(2015) mentioned the abundance of EW(Li) with an appropriate atmosphere model is comparable with that derived from SS(Li). However, the atmospheric model is inadequate for young giants, in this work the spectral synthesis analysis is adopted.

The line list used to derive the abundances is from D'Orazi et al. (2020), and covers the range between 3940 Å and 6900 Å. Equivalent widths (EWs) were measured with ARES (Sousa et al., 2015). Manual measurements with IRAF were performed for strong lines (EW > 150 mA), lines with high fitting errors from ARES, and lines whose ARES EW resulted in highly discrepant abundances. This check was done to account for the possible bad automatic fitting or for line blending. The determination of line list concluded below:

Li : Measurements for Li abundances are derived by the synthesis method using MOOG (line near 670 nm from D'Orazi et al. (2015)), NLTE correction from Lind et al. (2011) (correction value from 0.094 to 0.361 dex)

α-elements (O, Mg, Si, Ca, and Ti), Na and Al : Measurements of the abundances of these elements were based on EW analysis. The line list used to derive the abundances is from Manual measurements with IRAF were performed for strong lines (EW > 150 mA), lines with high fitting errors from ARES, and lines whose ARES EW resulted in highly discrepant abundances. This check was done to account for the possible bad automatic fitting or for line blending. And using the LTE

code MOOG code combined with the ATLAS9 atmospheric grid. For more details on target selection observations, data reduction, and stellar parameters derivation we refer the reader to Zhang et al. (2021).

- O: The two oxygen lines (630 nm and 636 nm)

- Mg and Si: abundances are derived from typically five lines

- Ca: is based on at least ten lines, are in excellent agreement

- Ti: Two ionised states Ti I and II ; typically 30 TiI lines and 20 TiII; we use only TiI for our measurement

- Na: use the lines at 475nm, 514nm, 568nm, 568nm, 615nm, and 616nm (NLTE correction line by line Lind et al. (2011))

- Al: doublet at 669.6nm, 669.8nm (NLTE correction calculated according to Nordlander & Lind (2017))

The detail information for each elements are in following section, for Li the abundance are obtained by the minimize the synthesis fitting error in specific lines after adjusting the spectral velocity shift, rescale, and smoothing Fig 5.1. The Fig 5.2 shows the synthesis fitting with 5 Li input abundance.

5.2   Adopted Solar Abundance

As solar reference abundance we adopt the default one in MOOG, i.e. Asplund et al. (2009)[1]. We have, however, performed the analysis of a solar spectrum, also obtained with HARPS-N, using the same steps as the SPA stars, deriving the following values for the elements under discussion:
A(Li)=0.96±0.10,
A(O)=8.74±0.04,
A(Na)=6.18±0.08,
A(Mg)=7.58±0.09,
A(Al)=6.44±0.07,
A(Si)=7.52±0.03,
A(Ca)=6.26±0.05,
A(Ti)=4.89±0.06
(and A(Fe)=7.50, as discussed in Chapter 4.

The values are in generally in good agreement with those in Asplund et al. (2009). An exception is O, which is in marginal agreement (the discrepancy may be also due to the different modelling of Asplund, that is 3D versus 1D). Its abundance was derived from the two forbidden lines for the SPA stars, which yield A(O)=8.715 from 6300.31 Å and A(O)=8.768 from 6363.79 Å for the Sun. It is worth noticing that in fact, the 6300 A line is affected by blending with a Ni line and the 6363 Å by a CN line. Caffau et al. (2008) also finds a discrepancy between the two lines, using spectra of much higher resolution (R> 300,000), and estimates the blends to account for up to 37% and 19% respectively (Caffau et al., 2013) of the two lines. The O abundance in our solar abundance is the average of the abundances from the two lines.

---

[1]The difference of solar abundance from Grevesse & Sauval (1998) and Asplund et al. (2009) is around 0.005 dex, in the accepted error range. However, in this part, the in order to excluded the error in chemical elements determination, we adopted the latest solar Fe abundance.

5.3 Derivation of chemical abundances
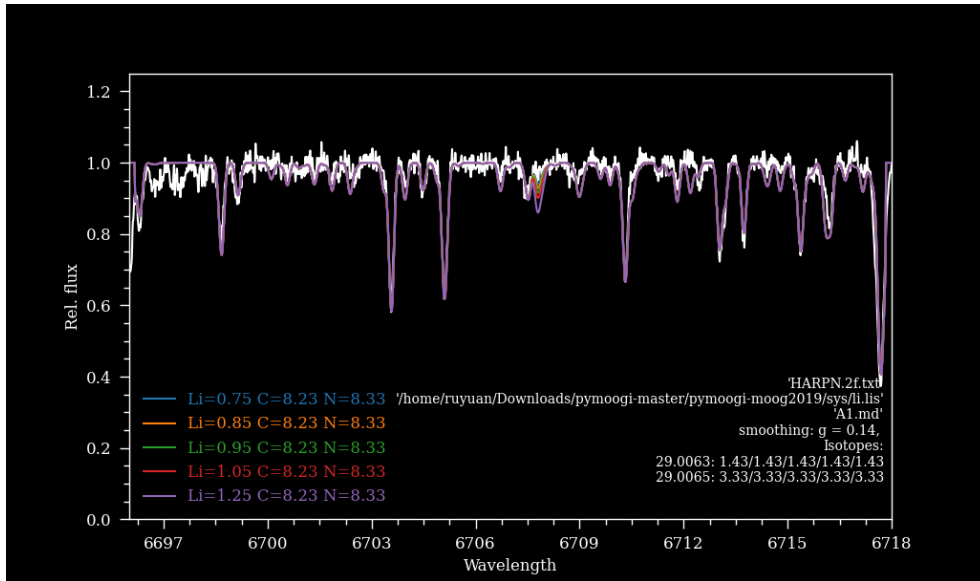
Figure 5.1: The synthesis fitting after adjusting the spectral velocity shift, rescale, and smoothing.

5.3.1 Lithium

In our spectra, the Li I line near 6707.81 Å is generally weak and mildly affected by blending with Fe I and CN lines. Measurements for Li abundances are derived by the synthesis method using MOOG and the line list from D'Orazi et al. (2015).

For five stars in our sample we could only place upper limits to the Li abundances, three of them belonging to the oldest open cluster we have, NGC 2682; they are all, however, less evolved objects. Non local thermodynamic equilibrium (NLTE) corrections for lithium were estimated using the same tool as for Na (see Sec. 2.4). All the corrections are positive, with values ranging from 0.094 to 0.361 dex. The uncertainty associated to the Li measurements is a combination of the synthesis fitting error and of the uncertainties of stellar parameters. Errors are listed in Table 5.1, while sensitivity to the parameters are in Table 5.4.

5.3.2 α elements

Oxygen required a particular care in line measurements. The two oxygen lines (6300.31 Å and 6363.79 Å), used to do the O abundance analysis in these stars, fall in a spectral range affected by telluric lines. Hence, depending on the radial velocity of the star, the O lines are affected by different degrees of blending. While modeling of telluric absorption is possible, in case of blending the resulting O lines (and in turn O abundances) have considerable uncertainties even after telluric absorption corrections have been applied.

However, the radial velocities for our sample excluded the contamination of the 6363 Å line, while the 6300 Å line was affected by telluric contamination in three cases. Therefore, we chose to discard the affected lines rather than subtract the modeled telluric absorption, and rely on the clean lines to derive the O abundances. We measured O abundance from one line in three stars and from
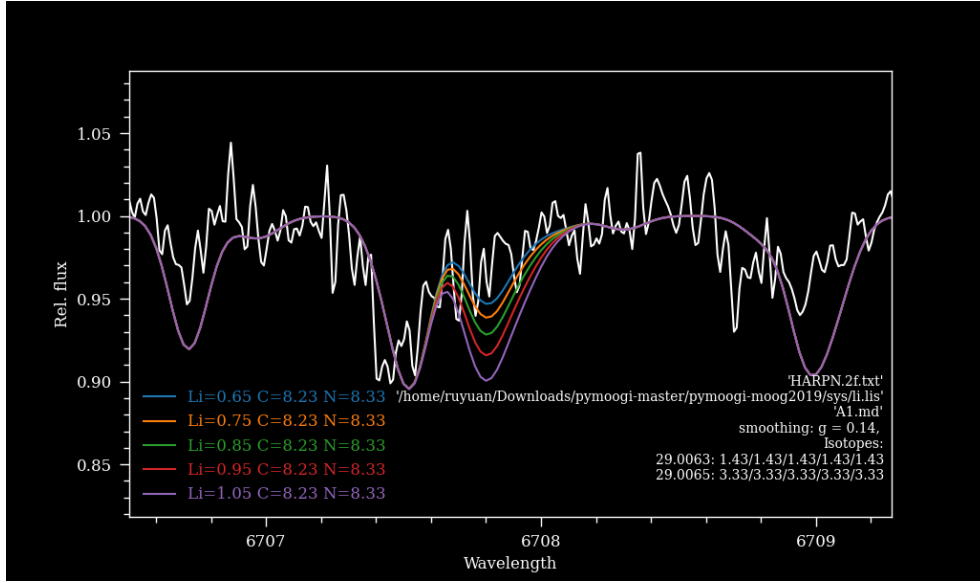
Figure 5.2: The synthesis fitting with 5 input Li abundance

two lines in 37 stars. We note that the oxygen abundance from 6300.31 Å is systematically lower than that from 6363.79 Å, consistently with the findings reported by the studies of Caffau et al. (2013).

Magnesium abundances are derived from typically five lines, for two of which (4703 and 5528) EWs were consistently measured manually. The lines were generally in good agreement with each other with no evidence for lines yielding systematically discrepant abundances. A similar number of lines, in excellent agreement with each other, were used for Si. Ca is based on at least ten lines in all the stars in the sample, and at least 18 in half of the sample. Lines are in excellent agreement.

Ti I and II are based on a good number of transitions (12 to 42 and 12 to 30, respectively). The agreement between the species in the two ionised states is less than optimal, with Ti II resulting systematically enhanced wrt to Ti I, with A(TI I)-A(Ti II)=-0.32±0.18 dex.

Baratella et al. (2020) also find Ti II overabundant wrt Ti I when using atmospheric parameters derived with the same traditional approach we use (1-D, LTE, Fe line based). In such paper, they argue that the traditional (1-D, LTE analysis based on Fe lines) is not optimal for very young dwarfs and developed an approach that uses both Ti and Fe lines to derive the parameters, considerably lessening the disagreement between the neutral and ionised species of Ti, which both result similar to the Ti I abundance derived with the traditional method.

We find a trend of the offset with age, with younger clusters having on average a worse match between the two ionisation states of Ti. However, the offset also correlates with evolutionary stage-gravity, suggesting that blends also play a role, given that low gravity, cooler stars have more crowded spectra. The spectra of cooler, low gravity stars are more crowded leading to larger uncertainties on the measurement of ionised Ti, which is based on fewer and weaker lines than its neutral counterpart. Lastly, it is worth mentioning that NLTE corrections might also play a role on this. For these reasons, we hence assume that the Ti II is the less reliable of the two measurements, using only Ti I in the further discussion.

5.3.3 Sodium and Aluminum

For sodium abundance analysis, the LTE is a poor assumption for line formation for the most used transitions in the optical. Abundance ratios [Na/Fe] from optical spectra for the stars of the kind under discussion are generally overestimated in LTE, leading to different LTE and NLTE trends of chemical abundance with Galactocentric distance (see e.g Lind et al., 2011). We use the lines at 4751Å, 5148Å, 5682Å, 5688Å, 6154Å, and 6160Å, and for each star, derived the NLTE corrections using the tool at http://inspect-stars.com/ on a line-by-line basis, applied to the individual line abundances that were then averaged to determine the Na abundance for the star. All the corrections are negative and vary from −0.216 to −0.005 dex.

The Al abundance was calculated based on the doublet at 6696.03, 6698.67 Å. NLTE corrections for Al were calculated according to the prescriptions in Nordlander & Lind (2017), using the code kindly provided by the authors. In general the corrections are negative. The Al line at 6696.03 Å has a range of NLTE corrections, between −0.03 and −0.09 dex, while the corrections range from −0.02 to −0.06 dex for the 6698.67 Å line.

5.4 Uncertainties on measured abundance ratios

Uncertainties associated with the abundances were derived taking into account the random error (calculated as the scatter from different lines) and the errors associated to the uncertainties in the atmospheric parameters.

In order to derive the sensitivity to the atmospheric parameters of the measured abundances, we selected nine stars as representative of the sample (one for each 100 K bin). The variations used were ΔT_{eff}=200 K, $\Delta \log g$=0.2 dex, Δ[Fe/H]=0.2 dex and Δv_{micro}=0.4 km/s. The derived Abundances for the α-elements are in Tables 5.2 and 5.3, while abundances for Li, Na, and Al, that is, elements requiring NLTE correction, are listed in Table 5.1. The sensitivity to the parameters uncertainties is in Table 5.4 for Li, Na, and Al and Table 5.5 for the α-elements, respectively.

5.5 Comparison with the literature

The abundance of Li is known to change considerably throughout the evolution of the star, therefore a comparison is meaningful only in the case of stars of very similar atmospheric parameters. There is very limited literature on the Li content in the present OC sample (with the exception of NGC 2682). Just another star has Li measurement previously reported in the literature in our entire sample: Collinder 350_2. The star has $\log\epsilon$(Li)=1.41±0.03 dex from Casali et al. (2020), which is compatible within the error with our result 1.58±0.14 dex. Out of the four NGC 2682 stars in our sample, we could measure Li only in one star, with a value of 0.461±0.30 dex. We place upper limits on the other three. However, while the Li content of NGC 2682 has been extensively studied in the literature (see e.g. Pace et al., 2012; Carlos et al., 2020; Magrini et al., 2021a), there are no reported Li measurements for any of these stars, nor for stars of very similar atmospheric parameters. Therefore, a direct comparison is not meaningful.

Figure 5.3 shows the comparison for α elements, Na, and Al in young clusters, while Fig. 5.4 shows the comparison for the well studied NGC 2682, an older cluster. The relevant literature is listed in Table 5.6 and Table 5.7

For [O/Fe], we have a good agreement for Basel11b, but the comparison for NGC 2548 is less than optimal, hinting to a possible offset with (Spina et al., 2021). For NGC 2682, on the other

hand, where more literature sources are present, there is a large scatter but no significant offset. It is worth noticing, in this context, that Spina et al. (2021) use a combination of optical (GALAH) and IR (APOGEE) data, and both atomic and molecular features to derive the abundances, which might lead to systematic effects in (some) abundances. Moreover, given the above discussed challenges associated with the derivation of O, some scatter is to be expected.

In Fig 5.3, our Na abundances are slightly lower than those from Spina et al. (2021), which however do not account for NLTE corrections. The average NLTE correction to the Na abundances for the two NGC 2548 stars in common with Spina et al. (2021) is −0.16 dex very similar to the Na offset abundance observed, which is ∼ −0.18 dex. On the other hand, there is good agreement with Casali's result, which does not take into account the NLTE correction. For NGC 2682, there are similar offsets in Na for studies that did not take into account NLTE corrections. There is again an offset between our result and those from Spina et al. (2021), and also similarly with Luck (2015), who also did not apply NLTE corrections. But the abundance of Na is compatible with the values reported by (Gao et al., 2018), who applies NLTE corrections, but interestingly also in good agreement with the Jacobson's work, who does not.

For Mg, the comparison with the literature in Fig. 5.3 suggests the presence of an offset. For Collinder350_2 the difference might be due to differences in the analysis wrt Casali et al. (2020). The parameters are different ($\Delta T_{\rm eff}$=130 K, Δlog g=0.3 dex, Δ[Fe/H]=0.05 dex, which correspond to a change of ~0.2 dex) and the atomic parameters for the transitions are also slightly different (log gf on average 0.06 dex lower than ours). A similar offset is also observed wrt what reported by APOGEE (Donor et al., 2020) (or Spina et al. 2021 who, indeed, combined GALAH and APOGEE clusters).

However, in NGC 2682, our analysis is mostly in fair agreement with literature values, with the exception of Jacobson et al. (2011), which have systematically higher abundances, generally higher than what is reported in the literature. We note that Jacobson et al. (2011) uses moderate resolution (R∼ 18000) spectra and one single Mg line, at 6319 Å, in a spectral range affected by telluric absorption features. The systematically high Mg abundance suggest the presence of blending that has not been accounted for. It is worth noticing also that Jacobson et al. (2011) uses MARCS rather than Kurucz models. However, this should lead to abundance differences which are negligible with respect to the observational errors associated with the measurements under discussion.

For Al, we are in good agreement with APOGEE results (Basel11b and NGC 2682, Donor et al. 2020), but find various degrees of offset with respect to the works of Spina et al. (2021) (NGC 2548 and NGC 2682), Jacobson et al. (2011) (NGC 2682), Gao et al. (2018) (NGC 2682), and Casali (Collinder 350). Some of them can be fully explained by the fact that they are LTE (Spina et al., 2021; Jacobson et al., 2011; Casali et al., 2020), and the NLTE correction can account for the differences. Gao et al. (2018), on the other hand, did include NLTE corrections in their analysis, using the approach described in Nordlander & Lind (2017), the same we adopt. The difference is therefore more likely to arise from the difference in atmospheric parameters (see Paper I), in the line list adopted and from the fact that Gao et al. use the GALAH pipeline, that performs an overall spectral fitting, rather than by individual lines analysis.

Our values for [Si/Fe] are in good agreement with literature results for all targets in common. This indicates its suitability to be used (along with Ca and Ti, see below) as a probe of α elements in combined samples.

The Ca abundance is in good agreement for all the stars in common with all literature sources, with the exception of Spina et al. (2021), that report values systematically larger for NGC 2548 and, to a lesser degree, for NGC 2682. As there are no systematics for what concerns the atmospheric parameters adopted (see Zhang et al. 2021), we do not have any explanation for this, except a possible offset due to those abundances being the result of the combination of optical and IR data.

Finally, the measured Ti abundances are in good agreement with the literature. All these comparisons are shown in Figs. 5.3 and 5.4.
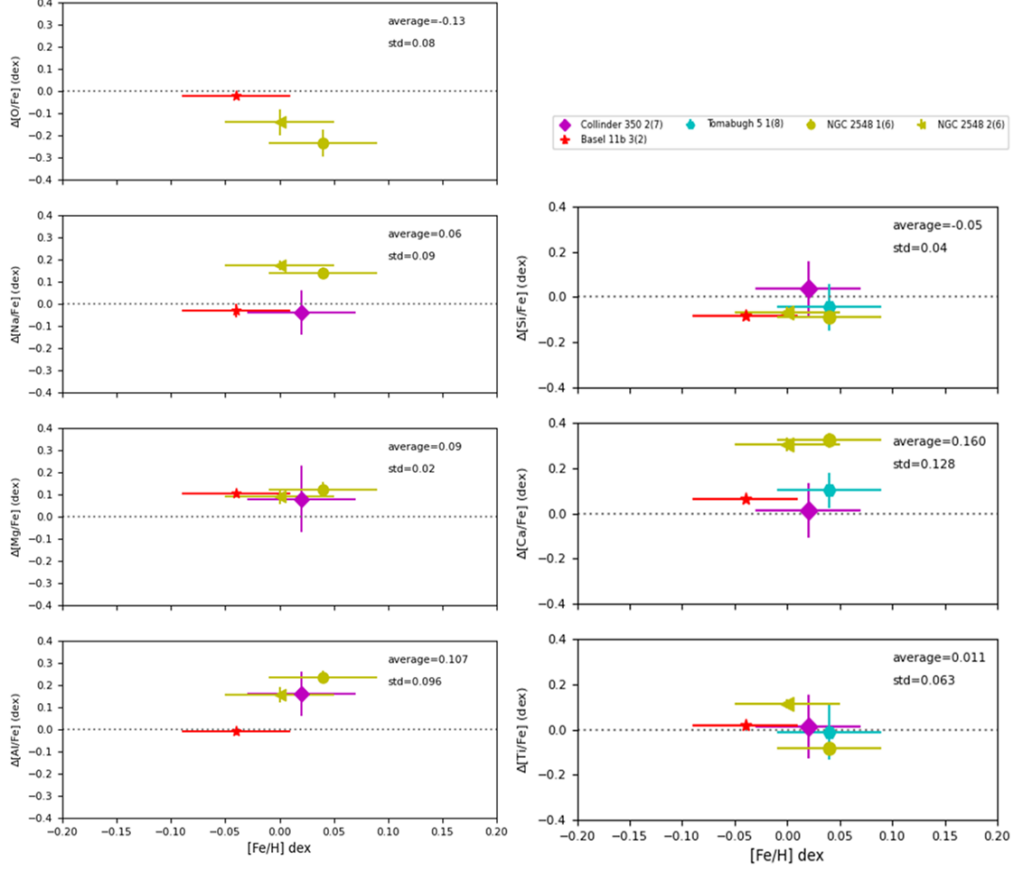
Figure 5.3: Comparison result of chemical abundance for young OCs with high resolution determination, We plot our [Fe/H] in the x axis and the difference (our minus literature) and the error from literature on the y-axis. The numbers between parenthesis close to the star's names are the literature references, based on Table 5.6 and Table 5.7: (2) APOGEE DR16; (6) Spina et al. (2021); (7) Casali et al. (2020); (8) Baratella et al. (2018).

5.6 Li, Na and Al and stellar evolution.

5.6.1 Li content

Lithium is destroyed at rather low temperatures, $\sim 2.5 \times 10^6$ K, which roughly correspond to the temperature at the base of the convective zone in a solar-mass stars. As stars evolve, Li gets depleted by mixing episodes (e.g. first dredge up) that mix the outer envelope with the interior. Lithium
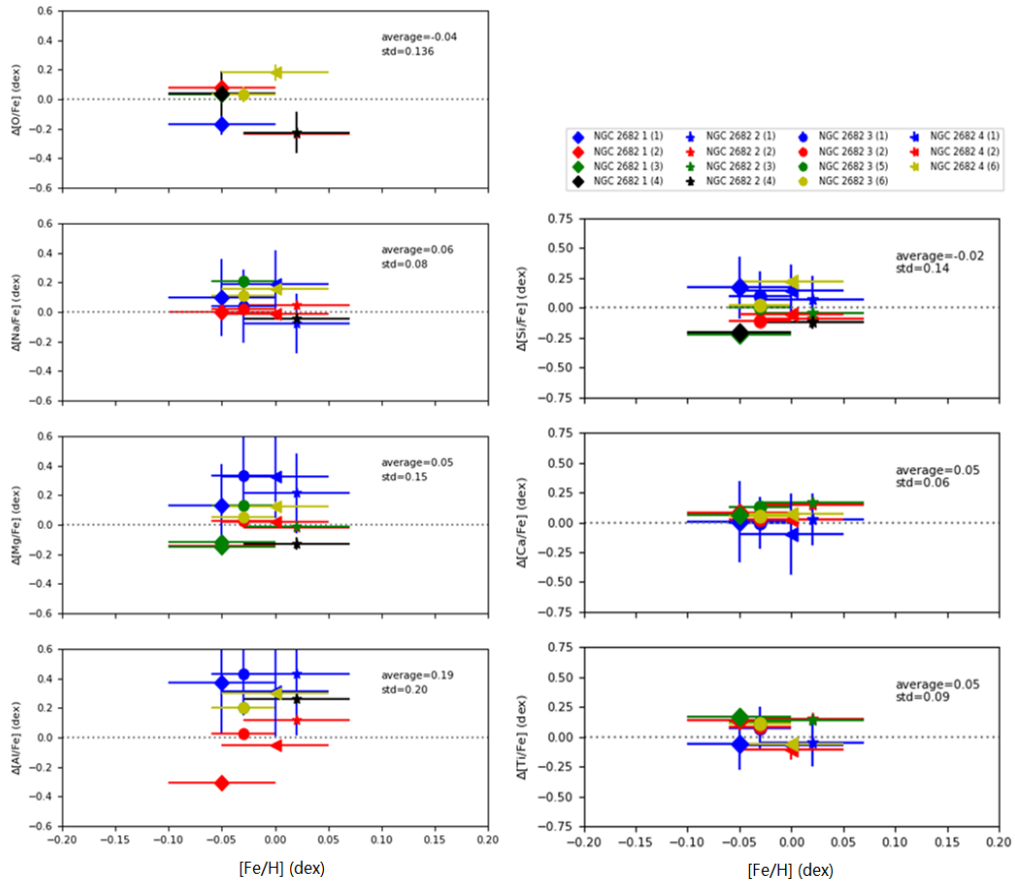
Figure 5.4: Comparison of chemical elements for targets in NGC 2682, The x-axis and y-axis are as in the previous figure. In the legend we show the different sources: (1) Jacobson et al. (2011); (2) APOGEE DR16; (3) (Casamiquela et al., 2019); (4) Gao et al. (2018); (5) Luck (2015); (6) Spina et al. (2021)

abundance is usually lower than ~1.5 dex for stars on the red giant branch (RGB) (see e.g. Casey et al., 2016). Lithium-rich giants have been detected both in the field and in clusters (see e.g Magrini et al., 2021a, where both open cluster and field stars where analysed homogeneously in the context of Gaia-ESO), but the reason for Li enrichment in these objects is still unclear.

Figure 5.5 shows the behavior of NLTE $\log \epsilon(Li)$ against T_{eff} and logg in our sample. Similar positive trend with LTE Li have been reported, for instance, by Delgado Mena et al. (2016); Magrini et al. (2021b); Franciosini et al. (2020). The four stars in our sample whose temperatures are higher than 5200 K (COIN-Gaia 30, Collinder 350_2, NGC 2437_3, and NGC 2548_1) have $\log \epsilon(Li) > 1.5$ dex, consistent with the result in Delgado's work from the hottest group of main-sequence stars ($T_{eff} > 5000$ K). We notice that some targets have high Li abundance for their evolutionary stage. ASCC 11 and NGC7082_2 have Li contents somewhat higher compared with the counterpart with similar log g, and Gulliver 37 and NGC 7209_2 also have a slightly high lithium for their effective temperature.

Our results show that our sample does not contain Li-rich stars. It is however clear that scatter in Li abundance is present at all temperatures, see also Fig 5.6, that exemplifies the observed differences, showing the comparison of the spectral Li line for two stars with similar atmospheric parameters and different Li abundances. This hints to other factors playing a role on the Li abundances in members of young clusters (e.g. age, metallicity, binarity, planet etc), consistently with what discussed, for instance, by Gutiérrez Albarrán et al. (2020).
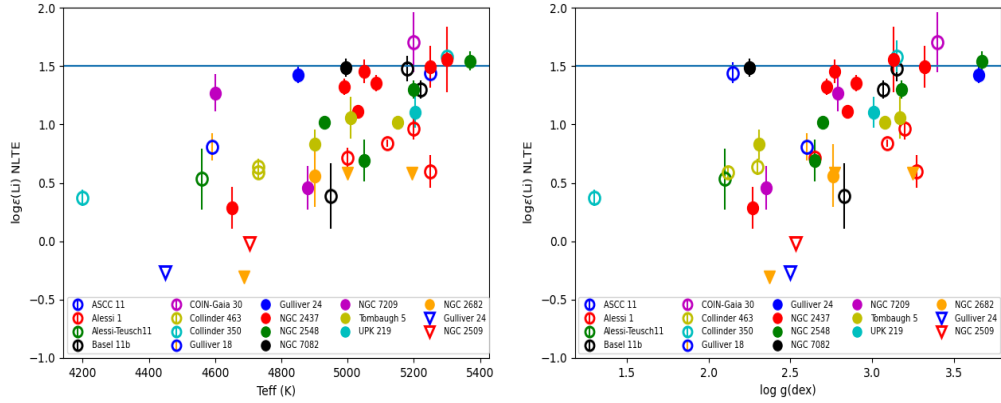
Figure 5.5: The distribution of Li abundance versus T_{eff} and log g for all samples. The inverted triangles are four stars with upper limit measurement, and the blue line is the value of standard definition Li-rich giant, i.e. $\log \epsilon(Li) = 1.5$ dex.

5.6.2 Sodium and Aluminum content in giants

Sodium and Aluminum are odd-Z elements, mainly produced by SNII (Kobayashi et al., 2020) and their production increases with increasing metallicity. On longer timescales, low to intermediate mass stars, during their asymptotic giant branch (AGB) phase, can reach the temperatures to activate the NeNa and MgAl cycles, resulting in changes in Na and Al on the stellar surface and ultimately contributing to the galactic chemical evolution of these elements.

Therefore, Na and Al are of interest to probe both the stellar and Galactic chemical evolution. Several published works like Jacobson et al. (2007), Smiljanic (2012) and Smiljanic et al. (2016, 2018) used the giants in OCs to explore the relationship between Na and Al abundance and first
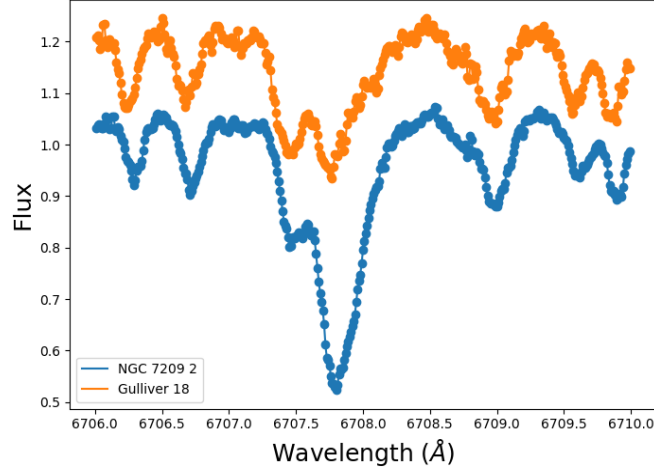
Figure 5.6: Comparison of spectra around the 6707.81 Å lithium line for two stars with similar stellar parameters and different Li abundance. They are the only star observed in Gulliver_18 (T_{eff}=4590 K, log g=2.60, [Fe/H]=-0.10 dex, log ϵ(Li)=0.8) and NGC_7209_2 (T_{eff}=4600 K, log g=2.79, [Fe/H]=-0.07 dex, log ϵ(Li)=1.27).

dredge-up. Our sample is more numerous and has a somewhat wider age range, therefore allowing to probe this issue on a wider stellar mass range. Figure 5.7 shows the comparison of our measurements for Na and Al with models. Turn-off masses for each OC were derived using the isochrones of Padova (PARSEC release v1.2s, Marigo et al. 2017 and COLIBRI, Pastorelli et al. 2020). The input age and metallicities of OCs are based on Table 1 and Table 4 in Zhang et al. (2021). The models are from Ventura et al. (2013) ([Fe/H]−0.4 dex and 0) and from Lagarde et al. (2014) (−0.54 and 0 dex) [2]. The Lagarde et al. (2014) models are calculated with and without rotation, assuming in the first case a rotation initially 30% of the critical velocity at the zero-age main sequence (see Lagarde et al. (2014). The model predictions would be different for a different value of initial rotation, reflecting a different effect of the rotation-induced mixing. Therefore, at a given mass the predictions are expected to show some scatter, the magnitude of which, however, cannot be estimated for the lack of available model predictions. Note that our comparison relies on the assumption that the stars had solar scaled Na and Al during their main sequence phase. While we have no direct information about the composition of these stars during their main sequence, Na and Al are known to be solar scaled among field disk dwarfs in the metal range relevant to this discussion. The left panel of Fig.5.7 shows the Na abundance as a function of Turn-off mass. Models for low mass stars, with M below ∼1–2 $M_{\odot}$, agree in predicting a modest, if any, Na variation in giants after the first dredge-up (as the ones we observed in our OCs). Instead, [Na/Fe] changes are expected for more massive star, with Na remaining at a constant (enhanced) level for M > 3 $M_{\odot}$ in the Ventura et al. (2013) models, while continuing to increase with increasing mass in the Lagarde et al. (2014) models, with the uptick being more pronounced in the rotating models.

Our results for Na span the same general range indicated by the models, however a detailed look at the plot provides some interesting pieces of information. Indeed, the lowest mass stars do not show any Na enhancement. However, already just below 2$M_{\odot}$, two of the clusters, NGC 2509 and

---

[2]The metallicities were derived assuming $Z_{\odot}$=0.014 from Asplund et al. (2009).
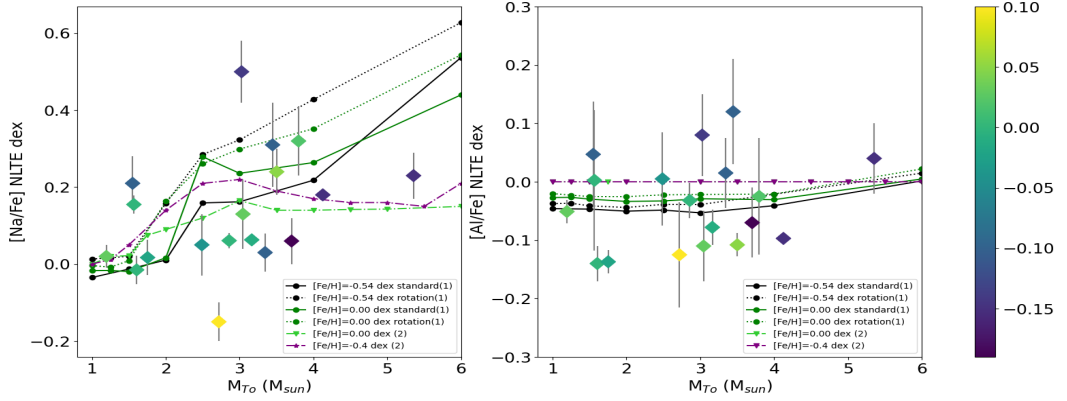
Figure 5.7: Comparison between the composition expected by stellar evolution models and observation for the abundances of Na and Al (both in NLTE). The points are colour-coded according to the cluster's metallicity and the lines colours indicate also the metallicity. References for models: (1) Lagarde et al. (2012); (2) Ventura et al. (2013).

Collinder 350, show a Na abundance higher than the predicted ones. For both these clusters the measurements are based on a single star, however we note that in a previous study, Smiljanic et al. (2016), presented Na and Al abundances for six OCs (no overlap with our sample), finding a mild Na enhancement in a cluster with Turn-off mass ~1.2$M_\odot$. For OCs with Turn-off mass larger than 2$M_\odot$, we observe enhanced Na content, even if with considerable scatter. In the 2-4 $M_\odot$ interval the Na abundances span a larger range than that of the models. At the high end, the [Na/Fe]= 0.5 dex of ASCC 11, is considerably higher than the Ventura et al. (2013) predictions, but could be likely accounted for by a Legarde model with a higher rotational velocity. At the low end, there are several clusters with Na abundances which are below than any of the predictions. The most extreme case is Gulliver 37, where Na is actually under-abundant (value is based on a single star, likely a binary, with [Fe/H]=0.1, and is the highest iron abundance in the sample), but several other clusters in this mass range have 0<[Na/Fe]<0.1, while the even the lowest prediction, the solar metallicity Ventura et al. (2013) model, are around 0.15-0.20 dex. This might suggest that the assumption of solar scaled main sequence Na abundance might not be appropriate.

We note that Smiljanic et al. (2016), who performed a similar study, did not find any clusters below the Ventura et al. (2013) predictions, nor did Smiljanic et al. (2018), who added 10 further clusters to the comparison. Jacobson et al. (2007) also measured Na and Al in three OCs, finding high values ([Na/Fe]> 0.4 dex) without NLTE corrections. Above 4 $M_\odot$ we have one single cluster, NGC 7082, whose Na is in fair agreement with the Ventura et al. (2013) models, and not matched at all by any of the Legarde models. Smiljanic et al. (2018) sample has two clusters above 4 $M_\odot$, with two having a modest Na enhancement, similar to that observed by us in NGC7082, a reasonable match to the Ventura models, while the third seems to favor the Legarde tracks.

The right panel of Fig. 5.7 shows the Al abundance vs Turn-off mass. The Ventura et al. (2013) models show no variation across the mass range considered, while the Lagarde et al. (2014) models predict a very modest increase above 4 $M_\odot$. The observations show more scatter than the predictions, even if most of the measurements are characterized by rather large uncertainties. Smiljanic et al. (2016) present less scatter, but their abundances lie all above the models level. In particular, at odds with us, they find no subsolar Al in their clusters. We note, however, that they report LTE Al

abundances, while we accounted for the NLTE effects, which are negative and can be quite large in stars like those under discussion (see Section 2.4). However, Smiljanic et al. (2018) increases the sample and applies NLTE corrections, finding a somewhat larger scatter and a possible upturn at high masses (based on two clusters), but no evidence of subsolar Al in their clusters.

Table 5.1: Lithium and Sodium abundance with NLTE correction.

Name	$\log \epsilon(Li)$	$\sigma_{log(Li)}$	[Na/Fe]	$\sigma_{[Na/Fe]}$	[Al/Fe]	$\sigma_{[Al/Fe]}$	T_{eff}	$\log g$	[Fe/H]	v_{micro}
	(dex)	(dex)	(dex)	(dex)	(dex)	(dex)	(K)	(dex)	(dex)	(km/s)
ASCC 11	1.44	0.09	0.50	0.08	0.18	0.07	5250	2.15	-0.14	2.4
Alessi 1_1	0.71	0.09	0.09	0.06	-0.17	0.06	5000	2.65	-0.10	1.5
Alessi 1_2	0.97	0.10	-0.12	0.10	-0.06	0.11	5200	3.20	0.08	1.5
Alessi 1_3	0.60	0.14	-0.03	0.06	-0.22	0.07	5250	3.27	0.07	1.6
Alessi 1_4	0.83	0.03	0.00	0.10	-0.11	0.11	5120	3.09	-0.05	1.6
Alessi-Teusch 11	0.53	0.26	0.06	0.06	-0.07	0.06	4560	2.10	-0.19	2.1
Basel 11b_1	1.47	0.11	0.05	0.05	-0.02	0.06	5180	3.15	0.00	2.2
Basel 11b_2	1.30	0.08	0.07	0.03	-0.16	0.04	5220	3.07	0.02	2.2
Basel 11b_3	0.38	0.28	0.07	0.05	-0.07	0.05	4950	2.83	-0.04	2.1
COIN-Gaia 30	1.70	0.26	0.13	0.09	-0.11	0.06	5200	3.40	0.03	2.3
Collinder 463_1	0.58	0.06	0.17	0.05	-0.11	0.05	4730	2.12	-0.20	2.5
Collinder 463_2	0.63	0.07	0.19	0.05	-0.08	0.05	4730	2.30	-0.10	2.4
Gulliver 18	0.80	0.12	0.31	0.11	0.12	0.09	4590	2.60	-0.10	2.8
Gulliver 24	-0.26	upper limit	0.03	0.05	0.02	0.06	4450	2.65	-0.18	2.0
Gulliver 37	1.42	0.07	-0.15	0.05	-0.13	0.09	4850	3.65	0.10	0.8
NGC 2437_1	1.45	0.10	0.08	0.06	-0.05	0.06	5050	2.77	0.04	2.1
NGC 2437_2	1.49	0.18	-0.04	0.06	0.07	0.06	5250	3.32	0.07	2.2
NGC 2437_3	1.55	0.28	0.11	0.07	0.08	0.08	5300	3.13	-0.05	2.3
NGC 2437_4	1.35	0.07	0.11	0.07	-0.08	0.06	5085	2.90	0.00	1.7
NGC 2437_5	1.11	0.04	0.08	0.10	-0.17	0.11	5030	2.85	0.00	1.7
NGC 2437_6	1.32	0.07	0.09	0.06	0.02	0.06	4990	2.72	0.00	2.1
NGC 2437_7	0.28	0.18	0.00	0.11	-0.10	0.10	4650	2.27	-0.07	1.2
NGC 2509	-0.02	upper limit	0.21	0.07	0.05	0.09	4705	2.53	-0.10	1.5
NGC 2548_1	1.59	0.08	0.07	0.05	-0.19	0.08	5370	3.67	0.00	2.0
NGC 2548_2	0.69	0.18	0.01	0.05	-0.12	0.04	5050	2.65	-0.02	1.6
NGC 2548_3	1.02	0.05	0.12	0.05	-0.06	0.06	4930	2.70	-0.01	1.6
NGC 2548_4	1.29	0.08	-0.13	0.06	-0.17	0.07	5200	3.18	-0.07	0.4
NGC 7082	1.52	0.08	0.23	0.06	0.04	0.06	4994	2.25	-0.15	3.0
NGC 7209_1	0.45	0.19	-0.07	0.05	-0.11	0.05	4880	2.35	0.00	1.7
NGC 7209_2	1.27	0.16	0.18	0.05	0.12	0.06	4600	2.79	-0.07	2.5
Tombaugh 5_1	1.06	0.18	0.22	0.05	-0.12	0.06	5010	3.17	0.04	2.2
Tombaugh 5_2	0.82	0.13	0.20	0.06	-0.05	0.06	4900	2.31	-0.07	2.0
Tombaugh 5_3	1.01	0.04	0.31	0.06	-0.14	0.06	5150	3.08	0.07	2.2
UPK 219	1.10	0.13	0.32	0.09	-0.02	0.10	5203	3.01	0.02	2.7
			Comparison clusters							
Collinder 350_1	0.37	0.07	0.12	0.09	0.18	0.09	4200	1.30	-0.40	2.2
Collinder 350_2	1.58	0.14	0.19	0.05	-0.17	0.06	5300	3.15	0.02	1.6
NGC 2682_1	-0.30	upper limit	0.00	0.06	0.00	0.07	4687	2.37	-0.05	1.5
NGC 2682_2	0.56	0.27	0.09	0.09	-0.13	0.11	4900	2.76	0.02	1.7
NGC 2682_3	0.58	upper limit	0.06	0.05	-0.04	0.05	5000	2.77	-0.03	1.2
NGC 2682_4	0.57	upper limit	-0.07	0.14	-0.02	0.04	5195	3.25	0.05	1.3
SUN	0.96	0.01	-0.03	0.07	-0.03	0.07	5770	4.44	0.03	1.0

Table 5.2: Chemical abundance (O and Mg) of observed targets

Name	Gaia ID	T_{eff}	log g	[Fe/H]	v_{micro}	[O/Fe]	σ_1	N	[Mg/Fe]	σ_1	N
		(K)	(dex)	(dex)	km/s	(dex)	(dex)		(dex)	(dex)	
ASCC 11	241730418805573760	5250	2.15	-0.14	2.4	-0.179	0.05	1	0.055	0.12	4
Alessi 1_1	402506369136008832	5000	2.65	-0.10	1.5	0.005	0.15	2	-0.039	0.06	5
Alessi 1_2	402505991178890752	5200	3.20	0.08	1.5	0.125	0.08	2	-0.195	0.15	4
Alessi 1_3	402867593065772288	5250	3.27	0.07	1.6	0.080	0.07	2	-0.184	0.07	5
Alessi 1_4	402880684126058880	5120	3.09	-0.05	1.6	0.121	0.09	2	-0.115	0.10	5
Alessi-Teusch 11	2184332753719499904	4560	2.10	-0.19	2.1	0.143	0.07	1	-0.170	0.06	4
Basel 11b_1	3424056131485038592	5180	3.15	0.00	2.2	0.108	0.06	2	-0.140	0.06	5
Basel 11b_2	3424055921028900736	5180	3.15	0.02	2.2	0.150	0.04	2	-0.184	0.05	5
Basel 11b_3	3424057540234289408	4950	2.83	-0.04	2.1	0.003	0.13	2	-0.143	0.05	5
COIN-Gaia 30	532533682228608384	5200	3.40	0.03	2.3	0.307	0.06	2	-0.184	0.06	4
Collinder 463_1	534207555539397888	4730	2.12	-0.20	2.5	0.080	0.12	2	-0.172	0.05	5
Collinder 463_2	534363067715447680	4730	2.30	-0.10	2.4	0.051	0.06	2	-0.143	0.05	4
Gulliver 18	1836389309820904064	4590	2.60	-0.10	2.8	0.340	0.08	2	-0.278	0.07	5
Gulliver 24	430035249779499264	4450	2.65	-0.18	2.0	0.258	0.07	1	-0.169	0.04	4
Gulliver 37	2024469226291472000	4850	3.65	0.10	0.8	0.046	0.07	2	-0.290	0.09	4
NGC 2437_1	3029609393042459392	5050	2.77	0.04	2.1	0.007	0.05	2	-0.213	0.05	4
NGC 2437_2	3029202711180744832	5250	3.32	0.07	2.2	0.171	0.07	2	-0.235	0.07	3
NGC 2437_3	3030364134752459904	5300	3.13	-0.05	2.3	0.107	0.05	2	-0.165	0.08	5
NGC 2437_4	3029132686034894592	5085	2.90	0.00	1.7	0.049	0.07	2	-0.134	0.09	4
NGC 2437_5	3029156222454419072	5030	2.85	0.00	1.7	0.026	0.09	2	-0.168	0.10	5
NGC 2437_6	3029207006148017664	4990	2.72	0.00	2.1	-0.028	0.05	2	-0.292	0.06	4
NGC 2437_7	3029226694277998080	4650	2.27	-0.07	1.2	-0.085	0.10	2	-0.219	0.08	4
NGC 2509	5714209934411718784	4705	2.53	-0.10	1.5	-0.028	0.13	2	-0.038	0.09	3
NGC 2548_1	3064481400744808704	5370	3.67	0.00	2.0	0.289	0.16	2	-0.190	0.07	3
NGC 2548_2	3064537647636773760	5050	2.65	-0.02	1.6	0.019	0.16	2	-0.138	0.05	5
NGC 2548_3	3064579703955646976	4930	2.70	-0.01	1.6	0.001	0.07	2	-0.115	0.07	4
NGC 2548_4	3064486692144030336	5200	3.18	-0.07	1.2	0.084	0.09	2	-0.184	0.07	3
NGC 7082	1972288740859811072	4994	2.25	-0.15	3.0	-0.019	0.07	2	-0.120	0.08	4
NGC 7209_1	1975004019170020736	4880	2.35	0.00	1.7	-0.067	0.09	2	-0.132	0.06	5
NGC 7209_2	1975002919658397568	4600	2.79	-0.07	2.5	0.421	0.09	2	-0.149	0.10	5
Tombaugh 5_1	473266779976916480	5010	3.17	0.04	2.2	0.110	0.11	2	-0.148	0.05	3
Tombaugh 5_2	473275782228263296	4900	2.31	-0.07	2.0	-0.040	0.14	2	-0.024	0.07	3
Tombaugh 5_3	473266779976916480	5150	3.08	0.07	2.2	0.211	0.07	2	-0.094	0.07	4
UPK 219	2209440823287736064	5203	3.01	0.02	2.7	0.076	0.06	2	-0.174	0.11	4
Collinder 350_1	4372743213795720704	4200	1.30	-0.40	2.2	-0.003	0.08	2	0.060	0.07	5
Collinder 350_2	4372572888274176768	5300	3.15	0.02	1.6	0.083	0.10	2	-0.029	0.11	5
NGC 2682_1	604921512005266048	4687	2.37	-0.05	1.5	0.089	0.15	2	-0.001	0.06	3
NGC 2682_2	604920202039656064	4900	2.76	0.02	1.7	0.167	0.14	2	0.008	0.08	4
NGC 2682_3	604904950611554432	5000	2.77	-0.03	1.2	0.036	0.08	2	-0.049	0.08	4
NGC 2682_4	604917728138508160	5195	3.25	0.05	1.3	0.084	0.12	2	-0.057	0.07	4
SUN		5770	4.44	0.03	1.0	0.082	0.04	2	0.011	0.09	5

Table 5.3: Chemical abundance (Si, Ca, and Ti) of observed targets

Name	[Si/Fe] (dex)	σ_1 (dex)	N	[Ca/Fe] (dex)	σ_1 (dex)	N	[Ti/Fe] (dex)	σ_1 (dex)	N
ASCC 11	0.174	0.07	3	0.129	0.15	12	-0.171	0.12	70
Alessi 1_1	0.184	0.05	9	0.027	0.10	26	-0.132	0.11	70
Alessi 1_2	0.112	0.12	9	-0.054	0.14	24	-0.101	0.15	70
Alessi 1_3	0.087	0.05	9	-0.049	0.09	24	-0.028	0.11	70
Alessi 1_4	0.184	0.17	9	-0.026	0.12	25	-0.135	0.14	65
Alessi-Teusch 11	0.267	0.07	9	-0.143	0.13	25	-0.132	0.13	60
Basel 11b_1	0.064	0.04	6	-0.063	0.13	24	-0.020	0.07	50
Basel 11b_2	0.124	0.04	7	-0.108	0.09	23	-0.040	0.08	30
Basel 11b_3	0.092	0.04	7	-0.076	0.09	25	-0.070	0.09	50
COIN-Gaia 30	0.000	0.04	9	-0.151	0.09	25	0.093	0.10	50
Collinder 463_1	0.141	0.05	8	-0.179	0.07	21	-0.074	0.08	30
Collinder 463_2	0.171	0.04	8	-0.173	0.08	23	-0.173	0.07	30
Gulliver 18	0.164	0.09	6	-0.176	0.17	22	0.227	0.22	100
Gulliver 24	0.288	0.08	6	-0.123	0.12	22	0.097	0.15	50
Gulliver 37	0.077	0.07	7	-0.214	0.19	15	-0.199	0.27	50
NGC 2437_1	0.080	0.04	9	-0.128	0.08	22	-0.066	0.09	50
NGC 2437_2	0.113	0.05	6	-0.097	0.11	22	-0.084	0.13	75
NGC 2437_3	0.104	0.06	7	-0.079	0.12	21	-0.023	0.16	110
NGC 2437_4	0.126	0.06	9	-0.022	0.15	25	-0.063	0.14	65
NGC 2437_5	0.167	0.08	8	-0.104	0.14	25	-0.160	0.15	75
NGC 2437_6	0.078	0.04	6	-0.146	0.10	22	-0.172	0.11	65
NGC 2437_7	0.170	0.07	7	-0.153	0.14	22	-0.160	0.19	90
NGC 2509	0.269	0.10	7	0.024	0.17	24	-0.020	0.12	50
NGC 2548_1	0.062	0.04	7	-0.025	0.11	23	0.010	0.10	40
NGC 2548_2	0.057	0.04	8	-0.044	0.11	25	-0.097	0.13	70
NGC 2548_3	0.099	0.05	9	0.025	0.11	26	-0.073	0.09	50
NGC 2548_4	-0.017	0.04	9	-0.123	0.08	20	-0.195	0.09	50
NGC 7082	0.085	0.05	6	0.021	0.10	20	-0.041	0.10	50
NGC 7209_1	0.103	0.05	9	-0.102	0.12	24	-0.086	0.12	50
NGC 7209_2	0.186	0.09	7	-0.07	0.18	22	0.045	0.12	30
Tombaugh 5_1	0.086	0.07	7	-0.171	0.10	21	-0.078	0.10	50
Tombaugh 5_2	0.137	0.04	6	-0.038	0.09	21	0.053	0.12	50
Tombaugh 5_3	0.121	0.05	7	-0.095	0.11	23	0.075	0.11	50
UPK 219	0.073	0.05	8	-0.167	0.13	22	0.059	0.16	150
Collinder 350_1	0.125	0.07	8	0.009	0.12	23	0.024	0.13	50
Collinder 350_2	-0.008	0.05	6	-0.024	0.10	23	-0.013	0.09	50
NGC 2682_1	0.098	0.06	6	-0.086	0.14	23	-0.067	0.15	50
NGC 2682_2	0.094	0.03	8	-0.144	0.08	23	-0.097	0.19	110
NGC 2682_3	0.091	0.04	8	-0.044	0.08	24	-0.070	0.12	50
NGC 2682_4	0.056	0.05	8	0.031	0.09	21	0.030	0.12	50
SUN	0.05	0.03	9	-0.053	0.05	25	-0.033	0.06	130

Table 5.4: Sensitivity matrix of Li, Na, and Al

Name	$\Delta\log\epsilon(Li)/\Delta\ T_{eff}$	$\Delta\log\epsilon(Li)/\Delta\log g$	$\Delta\log\epsilon(Li)/\Delta[Fe/H]$	$\Delta\log\epsilon(Li)/\Delta\ v_{micro}$
Collinder 350_1	0.028	0.013	0.020	-0.003
Alessi-Teausch 11	-0.026	0.030	0.030	-0.023
Collinder 463_1	0.090	0.020	-0.007	0.001
Gulliver 37	0.068	0.030	-0.003	0.004
NGC 2548_3	0.079	0.021	-0.043	0.000
Tombaugh 5_1	0.091	-0.002	0.001	0.000
Alessi 1_4	0.036	0.014	-0.012	0.013
UPK 219	0.072	-0.031	-0.086	-0.069
NGC 2548_1	0.060	-0.001	0.030	0.049
Name	$\Delta[Na/Fe]/\Delta\ T_{eff}$	$\Delta[Na/Fe]/\Delta\log g$	$\Delta[Na/Fe]/\Delta[Fe/H]$	$\Delta[Na/Fe]/\Delta\ v_{micro}$
Collinder 350_1	0.011	0.073	-0.049	-0.004
Alessi Teusch 11	0.037	-0.013	-0.047	-0.028
Collinder 463_1	0.021	-0.009	-0.047	0.002
Gulliver 37	0.034	-0.015	-0.026	-0.028
NGC2548_3	0.031	-0.008	-0.036	-0.017
Tombaugh 5_1	0.032	-0.020	-0.043	0.001
Alessi 1_4	0.000	0.042	-0.092	-0.012
UPK219	0.084	-0.012	-0.047	0.000
NGC2548_1	0.021	-0.011	-0.044	0.000
Name	$\Delta[Al/Fe]/\Delta\ T_{eff}$	$\Delta[Al/Fe]/\Delta\log g$	$\Delta[Al/Fe]/\Delta[Fe/H]$	$\Delta[Al/Fe]/\Delta\ v_{micro}$
Collinder 350_1	0.027	-0.002	-0.053	-0.087
Alessi Teusch 11	0.036	0.007	-0.051	-0.027
Collinder 463_1	0.021	0.002	-0.050	-0.008
Gulliver 37	0.031	-0.007	-0.029	-0.09
NGC2548_3	0.064	0.000	-0.052	-0.012
Tombaugh 5_1	0.030	0.000	-0.051	-0.011
Alessi 1_4	0.045	0.000	-0.051	-0.011
UPK219	0.093	0.000	-0.050	-0.015
NGC2548_1	0.064	0.000	-0.052	-0.012

Table 5.5: Sensitivity matrix of α-elements

Name	Δ[O/Fe]/Δ T_{eff}	Δ[O/Fe]/Δ log g	Δ[O/Fe]/Δ[Fe/H]	Δ[O/Fe]/Δ v_{micro}
Collinder 350_1	0.011	0.073	-0.049	-0.004
Alessi Teusch 11	0.007	0.065	-0.030	-0.002
Collinder 463_1	0.004	0.044	-0.030	-0.001
Gulliver 37	0.009	0.048	-0.018	-0.004
NGC2548_3	0.006	0.042	-0.023	-0.001
Tombaugh 5_1	0.006	0.063	-0.029	0.000
Alessi 1_4	0.006	0.024	-0.064	-0.003
UPK219	0.023	0.046	-0.030	-0.001
NGC2548_1	0.005	0.085	-0.030	-0.002

Name	Δ[Mg/Fe]/Δ T_{eff}	Δ[Mg/Fe]/Δ log g	Δ[Mg/Fe]/Δ[Fe/H]	Δ[Mg/Fe]/Δ v_{micro}
Collinder 350_1	0.019	-0.010	-0.068	-0.031
Alessi Teusch_11	0.025	-0.003	-0.045	-0.040
Collinder 463_1	0.019	-0.004	-0.046	-0.020
Gulliver 37	0.017	-0.011	-0.023	-0.085
NGC2548_3	0.030	-0.010	-0.045	0.054
Tombaugh 5_1	0.029	-0.015	-0.045	-0.021
Alessi 1_4	0.036	-0.008	-0.092	-0.017
UPK219	0.094	-0.012	-0.049	-0.034
NGC2548_1	0.039	-0.023	-0.047	-0.027

Name	Δ[Si/Fe]/Δ T_{eff}	Δ[Si/Fe]/Δ log g	Δ[Si/Fe]/Δ[Fe/H]	Δ[Si/Fe]/Δ v_{micro}
Collinder 350_1	-0.030	0.030	-0.058	-0.012
Alessi Teusch 11	-0.020	0.048	-0.043	-0.049
Collinder 463_1	-0.001	0.025	-0.042	-0.011
Gulliver 37	-0.020	0.022	-0.020	-0.087
NGC2548_3	-0.001	0.024	-0.037	-0.051
Tombaugh 5_1	-0.006	0.040	-0.059	-0.020
Alessi 1_4	0.003	0.011	-0.082	-0.018
UPK219	0.022	0.020	-0.043	-0.033
NGC2548_1	0.013	0.025	-0.035	-0.017

Name	Δ[Ca/Fe]/Δ T_{eff}	Δ[Ca/Fe]/Δ log g	Δ[Ca/Fe]/Δ[Fe/H]	Δ[Ca/Fe]/Δ v_{micro}
Collinder 350_1	0.060	-0.010	-0.082	-0.058
Alessi Teusch 11	0.000	-0.002	-0.216	0.000
Collinder 463_1	0.030	-0.003	-0.055	-0.039
Gulliver 37	0.047	-0.034	-0.026	-0.186
NGC2548_3	0.054	-0.013	-0.050	-0.049
Tombaugh 5_1	0.051	-0.019	-0.051	-0.037
Alessi 1_4	0.057	-0.087	-0.106	-0.040
UPK219	0.134	-0.008	-0.054	-0.069
NGC2548_1	0.056	-0.027	-0.050	-0.062

Name	Δ[Ti/Fe]/Δ T_{eff}	Δ[Ti/Fe]/Δ log g	Δ[Ti/Fe]/Δ[Fe/H]	Δ[Ti/Fe]/Δ v_{micro}
Collinder 350_1	0.087	0.010	-0.078	-0.066
Alessi Teusch 11	0.077	0.000	-0.051	-0.100
Collinder 463_1	0.045	0.000	-0.051	-0.023
Gulliver 37	0.064	-0.007	-0.029	-0.262
NGC2548_3	0.067	-0.002	-0.042	-0.051
Tombaugh 5_1	0.066	-0.004	-0.051	-0.039
Alessi 1_4	0.082	-0.002	-0.106	-0.034
UPK219	0.201	-0.006	-0.0555	-0.038
NGC2548_1	0.048	-0.008	-0.055	-0.075

Table 5.6: Comparison of chemical abundance with literature. The source information are listed in next table

star Gaia ID	[Mg/Fe] (K)	σ[Mg/Fe]	[Si/Fe] (dex)	σ[Si/Fe]	[Ca/Fe] (dex)	σ[Ca/Fe]	[O/Fe] (dex)	σ[O/Fe]
NGC 2682_1	-0.001	0.060	0.098	0.060	-0.086	0.140	0.089	0.150
604921512005266048	0.130	0.280	0.270	0.260	-0.080	0.340	-0.080	0.070
	-0.011	0.009	0.055	0.009	0.003	0.009	0.001	0.010
	-0.023	0.014	0.044	0.034	-0.016	0.045	-0.049	0.069
	0.010	0.040	0.060	0.040			-0.040	0.150
NGC 2682_2	0.008	0.080	0.094	0.030	-0.144	0.080	0.167	0.140
604920202039656064	0.220	0.270	0.160	0.200	-0.120	0.220		
	-0.009	0.009	0.003	0.009	0.002	0.010	-0.070	0.010
	-0.002	0.027	0.052	0.033	0.022	0.027	0.115	0.069
	-0.120	0.040	-0.030	0.050			-0.060	0.140
NGC 2682_3	-0.049	0.080	0.091	0.030	-0.044	0.080	0.036	0.080
604904950611554432	0.280	0.270	0.190	0.210	-0.050	0.220		
	-0.020	0.010	-0.020	0.010	-0.020	0.010		
	0.080		0.090		0.080			
	0.003	0.032	0.114	0.027	0.011	0.029	0.068	0.054
NGC 2682_4	-0.057	0.070	0.056	0.050	0.031	0.090	0.084	0.120
6049177728138508160	0.270	0.280	0.200	0.220	-0.070	0.340		
	-0.04	0.010	0.005	0.010	0.050	0.010		
	0.068	0.032	0.280	0.027	0.103	0.031	0.264	0.057
Collinder 350_2	-0.029	0.110	-0.008	0.050	-0.024	0.100	0.083	0.100
4372572888274176768	0.050	0.150	0.030	0.120	-0.010	0.120		
Basel 11b_3	-0.143	0.050	0.092	0.040	-0.076	0.090	0.003	0.130
3424057540234289408	-0.040	0.009	0.006	0.009	-0.015	0.010	-0.02	0.010
Tombaugh 5_1	-0.148	0.050	0.086	0.100	-0.171	0.100	0.110	0.110
4732667779976916480			0.040	0.102	-0.070	0.08		
NGC 2548_1	-0.190	0.070	0.062	0.040	-0.025	0.110	0.289	0.160
3064481400744808704	-0.067	0.033	-0.026	0.028	0.299	0.033	0.054	0.061
NGC 2548_2	-0.138	0.050	0.057	0.040	-0.044	0.110	0.019	0.160
3064537647636773760	-0.047	0.033	-0.012	0.027	0.260	0.031	-0.121	0.058

Table 5.7: Comparison of chemical abundance with literature. The last column contains the reference and information on NLTE correction for Na and Al:(1) Jacobson et al. (2011); (2) APOGEE DR16; (3) (Casamiquela et al., 2019);(4) Gao et al. (2018);(5) Luck (2015);(6) Spina et al. (2021);(7) Casali et al. (2020);(8) Baratella et al. (2018)

star Gaia ID	[Ti/Fe] (K)	σ[Ti/Fe]	[Na/Fe] (dex)	σ[Na/Fe]	[Al/Fe] (dex)	σ[Al/Fe]	Ref (NLTE)
NGC 2682_1	-0.067	0.150	0.002	0.060	0.000	0.070	Present study
604921512005266048	-0.130	0.210	0.100	0.260	0.370	0.350	(1)(NO)
	0.005	0.010	0.100	0.030	0.066	0.016	(2)(NO)
	0.036	0.034					(3)(NO)
			0.140	0.050	0.100	0.040	(4)(YES)
NGC 2682_2	-0.097	0.190	0.087	0.090	-0.130	0.110	Present study
604920202039656064	-0.150	0.200	0.010	0.200	0.300	0.420	(1) (NO)
	-0.050	0.010	0.130	0.030	-0.009	0.017	(2)(NO)
	0.044	0.033					(3)(NO)
			0.040	0.050	0.130	0.030	(4) (YES)
NGC 2682_3	-0.070	0.120	0.061	0.050	-0.040	0.050	Present study
604904950611554432	0.000	0.180	0.100	0.250	0.390	0.280	(1) (NO)
	0.010	0.010	0.080	0.040	-0.014	0.018	(2)(NO)
	0.050		0.270		0.160		(5)(NO)
	0.037	0.018	0.169	0.023	0.159	0.024	(6)(NO)
NGC 2682_4	0.030	0.120	-0.068	0.140	-0.020	0.040	Present study
604917728138508160	-0.040	0.240	0.120	0.230	0.290	0.310	(1)(NO)
	-0.080	0.020	-0.080	0.040	-0.025	0.018	(2)(NO)
	-0.027	0.023	0.091	0.023	0.277	0.026	(6) (NO)
Collinder 350_2	-0.013	0.090	0.190	0.050	-0.170	0.060	Present study
4372572888274176768	0.000	0.140	0.250	0.100	-0.010	0.100	(7) (NO)
Basel 11b_3	-0.070	0.090	0.069	0.050	-0.060	0.050	Present study
3424057540234289408	-0.050	0.010	0.040	0.030	-0.071	0.017	(2)(NO)
Tombaugh 5_1	-0.078	0.100	0.222	0.050			Present study
473266779976916480	-0.090	0.132					(8)
NGC 2548_1	0.010	0.100	0.065	0.050	-0.190	0.080	Present study
3064481400744808704	-0.071	0.020	0.205	0.024	0.045	0.028	(6) (NO)
NGC 2548_2	-0.097	0.130	0.012	0.050	-0.120	0.040	Present study
3064537647636773760	0.018	0.018	0.186	0.023	0.035	0.026	(6) (NO)

Chapter 6

Probing the Galactic Disk

The average metallicities for our sample of OCs are given in Tab. 4.3. These are combined with the clusters positions (in the following, Galactocentric distance and height on the plane) to discuss the metallicity distribution in the disc, adding literature data to increase the sample and the coverage of disc properties.

6.1   Metallicity distribution in the disc

The study of the radial and vertical fossil gradients such as age and composition is one of the main approaches in probing the Galactic disc(s).

In this section, we discuss the observed behaviour of OCs' metallicity, age and Galactocentric distance and what information can be gained by the comparison with models for the disc. First we derive the classical radial gradient in metallicity (e.g. Friel et al. 2002), then we compare observations with models. Our sample is distributed essentially on the Galactic plane, the SPA clusters are all within 0.5 kpc (Cantat-Gaudin et al., 2020), and generally in the solar neighbourhood, with Galactocentric distance ranging between 7.7 to ~10 kpc. With one single exception – NGC 2682, which was observed for comparison purposes – the clusters are quite young, with 14 out of 18 clusters being younger than 0.5 Gyr.

By combining our data with results from some selected surveys and studies, we can widen the sample to clusters with larger ages and/or distances from the Galactic centre, building a sample that allows us to probe the properties of the Galactic disc, and can be used to constrain models of the chemo-dynamical evolution of the disc. The SPA sample currently includes the present analysis as well as four more OCs in Casali et al. (2020), one from D'Orazi et al. (2020), and another one in Frasca et al. (2019). We include the results from the large spectoscopic surveys, namely: a) APOGEE [1] (Donor et al., 2020), with more than 120 OCs, mostly in the 6-15 kpc range in R_{gc} and with [Fe/H] from -0.5 to 0.4 dex; b) GES, covering the wide range of Galactocentric distance from 5.8 to 20 kpc, and the metallicity range -0.5 to 0.4 dex; c) and GALAH (Spina et al., 2021), keeping only clusters whose parameters are based on HERMES spectra and excluding those based on the recalibration of APOGEE (see Spina et al. 2021 for details). Moreover, we include the OCCASO sample (Casamiquela et al., 2017), whose OCs are located at Galactocentric distances similar to those of the SPA project (6.5 to 10.5 kpc) and with metallicities around the solar value, ranging from −0.1 dex to 0.17 dex.

---

[1]We downloaded the Value Added Catalog for the Open Clusters Chemical Abundance and Mapping project (OCCAM), at https://data.sdss.org/sas/dr16/apogee/vac/apogee-occam/

The relationship between metallicity and Galactocentric distance, classically called metallicity gradient, is shown in Fig. 6.1 for the combined sample, dividing it in three age intervals (selected because they are the same in Minchev et al. 2014b, see below). The metallicities come from the cited sources (averaging values when more than one was available for a given cluster) and the R_{gc} values come from Cantat-Gaudin et al. (2020) where $R_{gc,Sun}$=8.34 form Reid et al. (2014). Table 6.1 contains the corresponding gradients, for the whole sample and separated in age bins. As the slope shows a change at about R_{gc} =14 kpc, we use that limit for inner/outer regions. The same was done in past works, as can be seen from Tab. 6.2, where we list some selected literature papers. We show the values in Friel et al. (2002), since this is possibly the first analysis of an homogeneous and large spectroscopic sample, albeit based on low resolution spectra, and in a few recent papers. As every work uses different age bins and R_{gc} ranges, we can make only a qualitative assessment of the results. However, the values in the two tables compare generally well; a few discrepant values are commented in the notes of Tab. 6.2.

Figure 6.2 shows metallicity as a function of distance from the Galactic plane, divided in age bin like the previous figure. The calculated values are listed in Table 6.1 as well. Note that, overall, the trends with |z|, even in well populated bins (e.g. young clusters in the inner disk), is far less statistically relevant than the corresponding slope wrt galactic radius. Figure 6.3 is the metallicity distribution with respect to age, but there are no obvious trends between [Fe/H] and age.

We also explored possible residual azimuthal gradient (only for well populated bins), finding extremely weak and moderately significant trends. For the overall sample within 14 kpc, we found 0.0028±0.0007, while for the sample below 2 Gyr within the same radius we found 0.0022±0.0009.

Table 6.1: Observed slope of the metallicity gradient.

Age (Gyr)	R_{gc} (kpc)	d[Fe/H]/dR_{GC} (dex kpc^{-1})	d[Fe/H]/d$|z|_{GC}$	$N_{clusters}$
all ages	Rgc<14	-0.066±0.005	-0.249 ± 0.062	157
all ages	Rgc>14	-0.032±0.007	-0.040 ± 0.028	4
age<2	Rgc<14	-0.059±0.006	-0.236 ± 0.119	133
2<age<4	Rgc<14	-0.089±0.007	-0.195 ± 0.144	13
age>4	Rgc<14	0.008±0.041	0.081 ± 0.117	11

6.1.1   Metallicity of Clusters and field stars

The recent APOGEE data release contains analysis for a large sample of young field stars, that might provide a more suitable comparison sample for our purposes. Figure 6.4 shows the measured metallicity with respect to Galactocentric distance and distance from the mid-plane. We used the latest result from APOGEE in DR 17 with distances and age estimates from the `astroNN` catalog based on deep-learning code combined with multiple methods (Leung & Bovy, 2019). We selected a sample of thin disk giants ($1.5 < \log g < 3.5$) spanning the same spatial range as our clusters, $|Z| < 0.5$ kpc, $7 < R_{gc} < 11$ kpc. We also applied quality cuts for Mg and age analogous to those for the HARPS-GTO sample. These criteria resulted in a sample of ~67000 stars. The average iron abundance of present OCs is comparable with that of APOGEE samples and does not show an obvious gradient.

Figure 6.1: The distribution of metallicity with Galactocentric distance in three age bins (the same used in Minchev et al. 2014, see Sec. 5.2). Beside our clusters, we show data from APOGEE (Donor et al., 2020), GES (Casali et al., 2019), OCCASO (Casamiquela et al., 2017),and GALAH (Spina et al., 2021) plus SPA results already published (Frasca et al., 2019; Casali et al., 2020; D'Orazi et al., 2020).
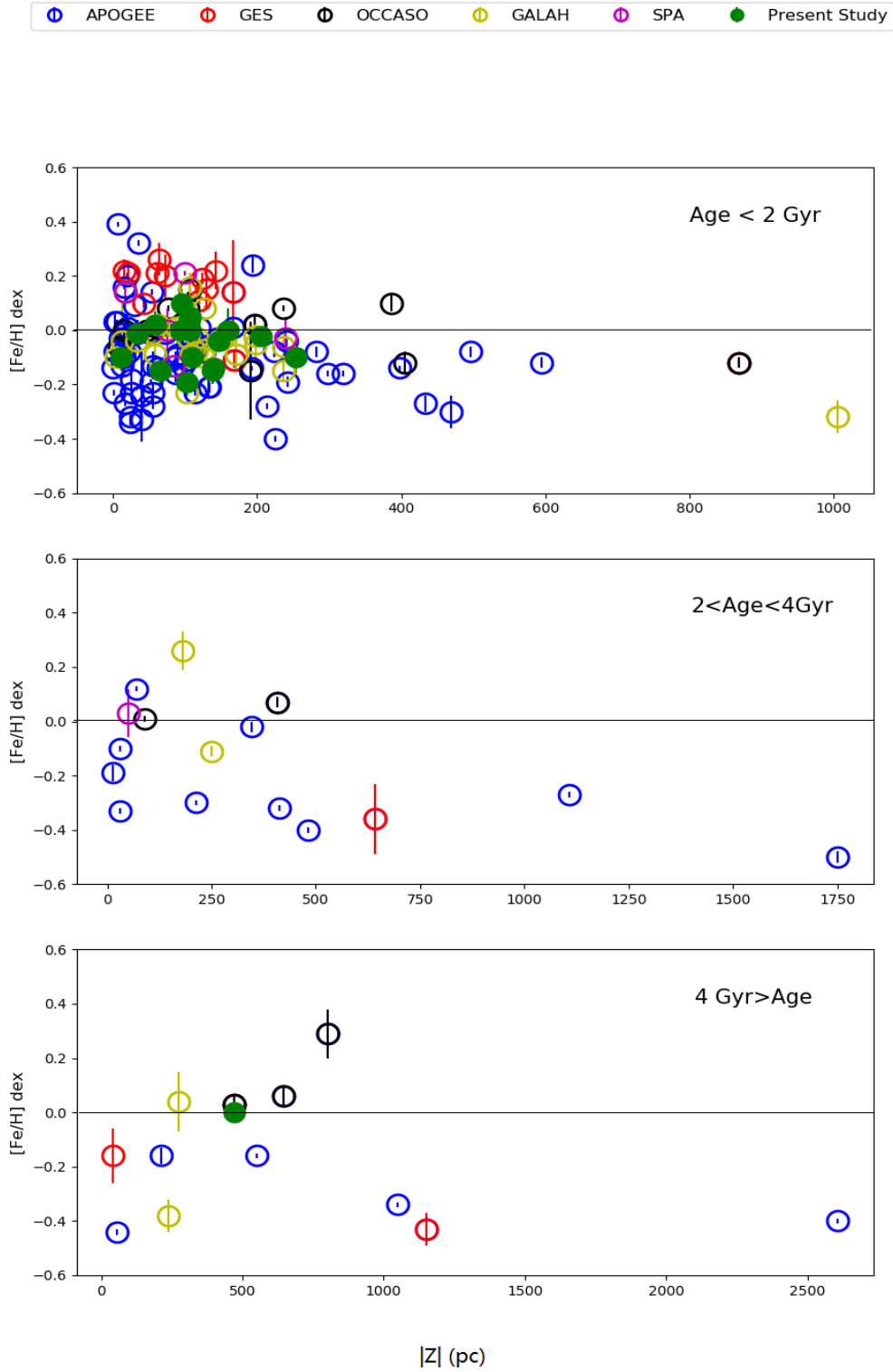
Figure 6.2: The distribution of metallicity with distance from mid-plate in three age bins (the same used in Minchev et al. 2014, see Sec. 5.2). Beside our clusters, we show data from APOGEE (Donor et al., 2020), GES (Casali et al., 2019), OCCASO (Casamiquela et al., 2017),and GALAH (Spina et al., 2021) plus SPA results already published (Frasca et al., 2019; Casali et al., 2020; D'Orazi et al., 2020).
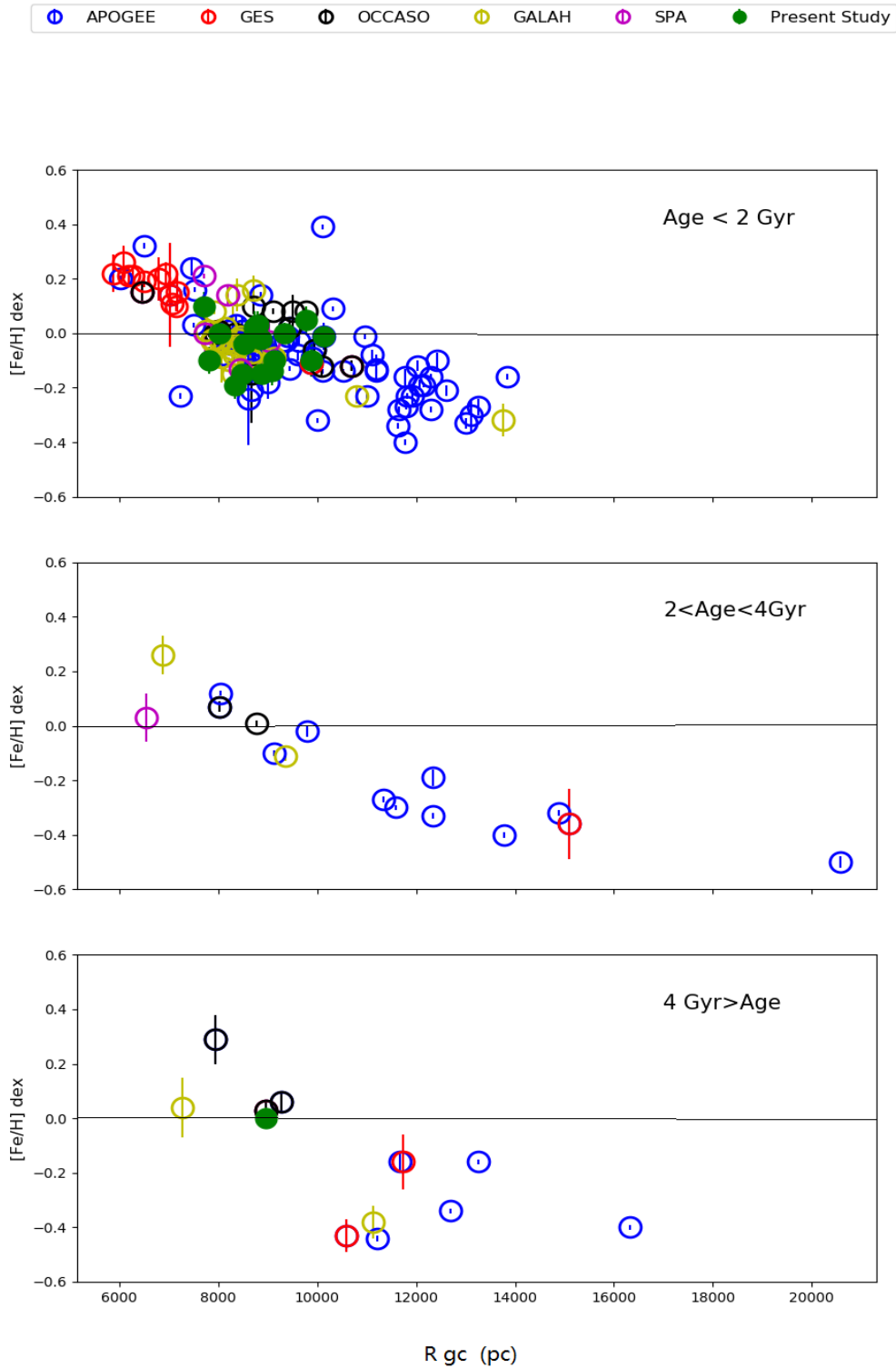
Figure 6.3: The distribution of metallicity with clsuters' age in three age bins (the same used in Minchev et al. 2014, see Sec. 5.2). Beside our clusters, we show data from APOGEE (Donor et al., 2020), GES (Casali et al., 2019), OCCASO (Casamiquela et al., 2017),and GALAH (Spina et al., 2021) plus SPA results already published (Frasca et al., 2019; Casali et al., 2020; D'Orazi et al., 2020).
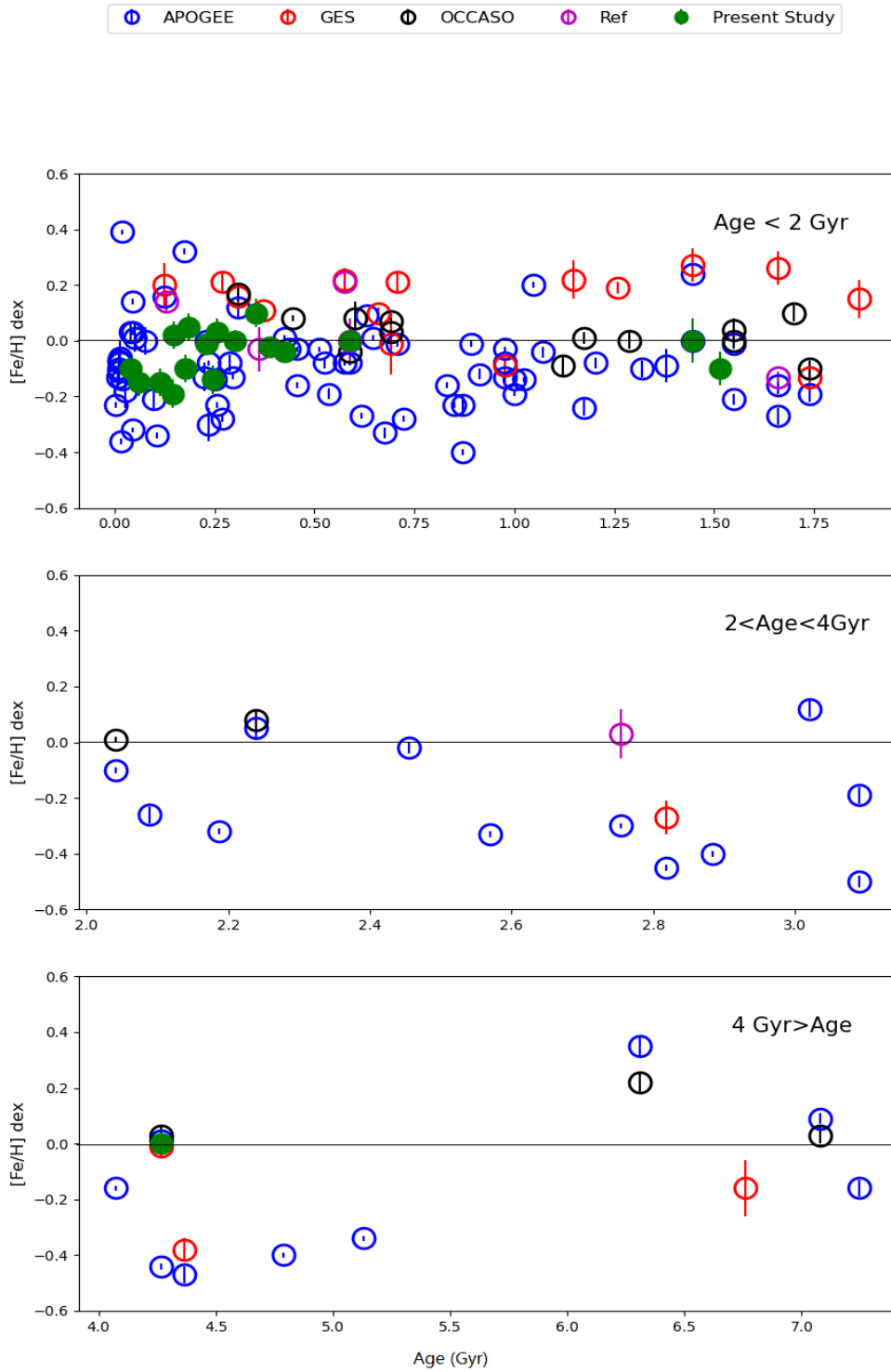
Table 6.2: Slope of the metallicity gradient from selected literature papers.

Reference	sample	d[Fe/H]/d R_{gc}	N OCs	Comment
Friel et al. (2002)	low-res optical spectra	-0.059±0.010	39	7<R_{gc} <16 kpc, all ages[a]
Reddy et al. (2016)	high-res optical spectra	-0.052±0.011	67	6<R_{gc} <12 kpc and $\|z\|$ <500 pc
		-0.015±0.007	12	12<R_{gc} >24 kpc[b]
Carrera et al. (2019)	APOGEE DR14, GALAH DR2	-0.052±0.003	46	6<R_{gc} <13 kpc[c]
		-0.077±0.007		6<R_{gc} <11kpc[c]
		0.018±0.009		11<R_{gc} <13 kpc[c]
Casamiquela et al. (2019)	high-res optical spectra	-0.056±0.011	18	R_{gc} <12 kpc, all ages[d]
Donor et al. (2020)	APOGEE DR16	-0.068±0.004	68	R_{gc} < 13.9 kpc, all ages[e]
		-0.009±0.011	3	R_{gc} >13.9 kpc, all ages

[a] the slope is also given in different age ranges, with a gradient steepening for increased age: -0.023, -0.053, -0.075 for age <2, 2-4, and >4 Gyr, respectively (a similar result was found by Andreuzzi et al. (2011) using [Fe/H] from high resolution spectroscopy, who found values of -0.07 and -0.15 for age lower and larger than 4 Gyr, respectively).
[b] They do not consider it representative of the disc midplane (their Sec. 5)
[c] The first value is obtained for OCs where at least 4 stars were measured, the second and third to the whole sample. The gradient in the outer bin becomes -0.04±0.01 if the two low metallicity OCs close to R_{gc}11 kpc are excluded.
[d] No significant difference in the age ranges covered.
[e] Also divided for age: -0.50 (13 OCs, age<0.4 Gyr), -0.073 (16 OCs, 0.4-9,7 Gyr), -0.066 (27 OCs, 0.8-2 Gyr), and -0.094 (12 OCs, >2 Gyr).

6.2   Comparison with chemo-dynamical models for iron

It must be kept in mind that the chemo-dynamical evolution of the Galactic disc(s) is a rather complex process and the expectation is that much of the initial information will be diluted through the dynamical evolution and radial mixing of the disc. This is expected to affect differently populations of different ages: broadly speaking, the older a cluster is, the more it has undergone dynamical evolution and radial mixing, even if other factors come into play, like the details of the formation environment and more in general the shape and mass of the disc at the time of formation and early evolution.

Recent models for the Galactic thin disc, e.g. Minchev et al. (2013, 2014a,b), taking into account sophisticated simulations in the cosmological context (Martig et al., 2009, 2012) along with a detailed knowledge of the chemical evolution of the disc have been able to generate theoretical gradients to compare with the observations at different ages. However, uncertainties exist, also due to model assumptions (e.g. initial gradient of chemical abundance), especially with regard to the oldest clusters and those furthest from the Galactic plane, which have undergone a large amound of dynamical evolution during their lives.

Minchev et al. (2014a) provide gradients calculated for different age intervals and ranges of distance from the Galactic plane. Figure 6.5 shows the comparison between the combined sample predictions from chemo-dynamical thin-disc model by (Minchev et al., 2014, the so-called MCM model). These models are calculated taking into account cosmological and dynamical properties, and chemical evolution, combining the effects of migration, the distance above the disc midplane, and then
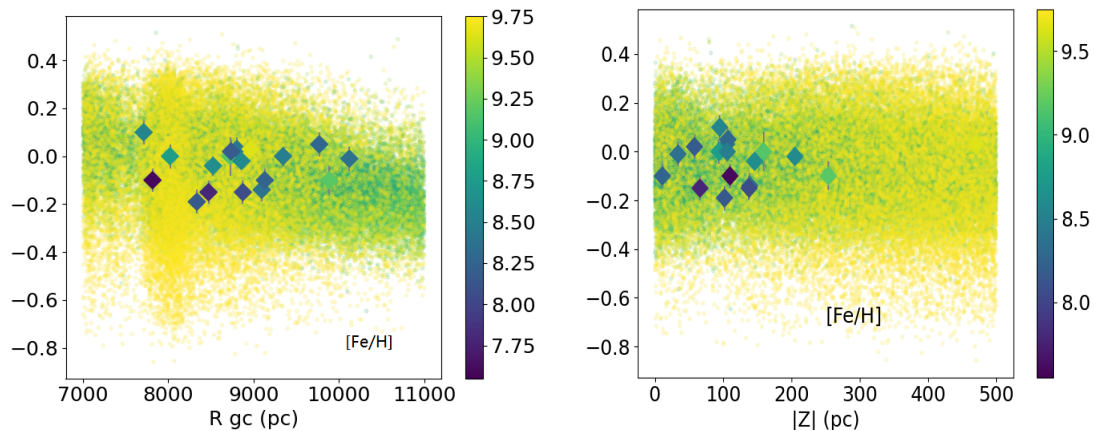
Figure 6.4: Average iron abundance with respect to R_{gc} and $|Z|$ for the SPA OCs and the samples selected from APOGEE DR17 as the previous figure shows.

extending the model beyond the solar neighborhood. Furthermore, the uncertainties of observation, and the evolution of Galactic disc was considered. From the MCM models we consider the range 0-0.8 kpc in terms of distance from the Galactic plane, which is appropriate for clusters in SPA, but also for the vast majority of the literature sample. We plot the predictions for both $|z| < 0.3$ kpc and for 0.3 kpc$< |z| < 0.8$ kpc.

Figures 6.5 and 6.6 show the comparison between MCM predictions and results from observation data, grouped according to age in bins of 0.3 and 0.5 Gyr, respectively, up to 4.5 Gyr. Predictions are generally a good match for the observation in the age range from 0.3 Gyr to 4.5 Gyr. It is worth noting that in the oldest age bin, two of the three discrepant clusters have $|z| > 1$ kpc, larger than the range the models have been calculated for, while the third has a metallicity based on one single star. On the other hand, in the youngest bin the fitting is very poor, even if the clusters lie closer than 0.5 kpc from the Galactic plane; we will come back to this problem later. For a more quantitative comparison with the Minchev et al. (2014b) results we derived the gradients in our sample following the bins in age and Z in their Table 1, considered the error of metallicities in the fitting process. We employed their same separations in R_{gc} and $|z|$ and computed the corresponding gradients for the observed sample. Interestingly, the gradient computed for age younger than 2 Gyr and $|z| < 0.25$ kpc, i.e. the bin comprising the vast majority of our sample (97 OCs), is comparable to that from the prediction: -0.066 ± 0.008 versus -0.057 for observed and predicted slope, respectively (see below, however, for a caveat on the very young clusters). Values are instead different in the other bins, which are, however, very scarcely populated, so it is difficult to assess if the discrepancy is important.

Coming back to the very different distribution of OC metallicity for young ages (already noticed in past work, e.g. Spina et al. 2017), several possible factors might be the source(s) of the poor fit. On the observational side, inaccurate measurements of the parameters could cause the issue. For example, a systematic underestimate in the Galactic distances would lead to outer disc clusters being compared to solar neighborhood predictions. A systematic underestimate in Z, on the other hand, would mean that we would be using predictions unsuitable for the sample. R_{gc} and Z are based on Gaia DR2 data, with typical uncertainties of around 5% to 10% for distance (Cantat-Gaudin et al., 2020), which is not large enough to generate the observed effect. Moreover, if such a systematic errors existed, they would very likely affect similarly clusters in the other age bins, a phenomenon of which there is no

evidence. We note that a systematic error in the adopted age could not in any way explain the poor fit: the discrepant clusters with < 0.3 Gyr would not be reproduced by predictions of any of the plotted ages.

Another possibility is that (part of) the metallicities we are using in the plot are not enough accurate. In particular we have checked in more detail APOGEE cluster from Donor et al. (2020). Firstly, we have detected that for several cluster there are significant difference between the two latest data releases, DR16 (Donor et al., 2020) and DR14 (Donor et al., 2018; Carrera et al., 2019), even if the same stars are used in both cases. This is for instance the case of King 7, with [Fe/H]=-0.13±0.05 and -0.04±0.01 in DR16 and DR14, respectively. These differences may be explained by the different methodologies used in the two releases to obtain the final abundances (see Jönsson et al., 2018, 2020, for a detailed explanation). For several clusters the values are based only on a single star with either low astrometric membership probability from Cantat-Gaudin et al. (2018), e.g. Berkeley 79, Czernik 23, FSR 852, King 12, NGC 1857 and/or with discrepant radial velocities in comparison with the literature, e.g. Czernik 23, NGC 2311, NGC 6383. Additionally, the star observed in NGC 2311 lies well out of the cluster sequence and the star in NGC 6383 has a high rotation velocity (>20 km s^{-1}) which complicates its analysis. In principle the APOGEE sample includes two stars in NGC 2232 with giants atmospheric parameters but this cluster does not have giants. In fact, they have a negligible astrometric membership probability from Cantat-Gaudin et al. (2018) and their radial velocities (~82 km s^{-1}) are in disagreement with the average value derived from 19 stars (~25 km s^{-1}) with very high astrometric probabilities from Gaia DR2 by Soubiran et al. (2018). In the case of the star forming region NGC 1977, the DR16 metallicity [Fe/H]=-0.21 dex, derived from 3 stars (there is no determination in DR14), is in disagreement with the value reported in the high quality high resolution spectroscopy by Netopil et al. (2016) of [Fe/H]=-0.06 dex from 2 stars obtained from Cunha, Smith, & Lambert (1995). In the case of NGC 2264, again without astrometric membership probabilities available there is good agreement between APOGEE DR16 ([Fe/H]=-0.18 dex from 23 stars) and the value determined by King et al. (2000) ([Fe/H]=-0.18 dex from 3 stars) but they disagree with the recent determination by Baratella et al. (2020) of [Fe/H]=+0.11 dex from a single star observed with UVES as part of Gaia-ESO. Baratella et al. (2020) amply discusses the problems of analysing spectra of MS stars in young stars and tries to devise a more robust method. In contrast, there are other cases, such as Berkeley 33, NGC 136, and SAI 116, whose metallicities seem reliable although they are based only on 4, 1 and 2 stars, respectively. These stars have a very high astrometric membership probability from Cantat-Gaudin et al. (2018) and the derived radial velocities are in good agreement with other values reported in the literature.

All these cases seem to indicate that we have to take the metallicity of young clusters with care. We also tried to understand which ages are more problematic. We show in Fig. 6.7 only clusters younger than 300 Myr, with the symbol size proportional to the number of stars available in each cluster. Apparently, the sample size is not the (main) source of the problem.

The clusters showing the larger discrepancy with respect to the model are younger than 200 Myr, and especially younger than 100 Myr. This is affecting analyses done both in the optical and the IR. As already discussed in literature (Yana Galarza et al., 2019; Baratella et al., 2020; Spina et al., 2020), in young dwarves chromospheric effects and considerable magnetic fields are at play, making a traditional 1-D LTE analysis based on minimising trends for Fe lines less than optimal. In fact, an intensification of strong absorption lines, those forming near the top of the stellar photosphere where the magnetic fields are more vigorous, has been observed as a function of the activity level during the stellar cycle (Yana Galarza et al., 2019; Spina et al., 2020). The cause of this effect can be imputed to Zeeman broadening of atomic lines or the effect of cool stellar spots. However, it is possible that many other phenomena related to the chromospheric activity, which are neglected in stellar models,

are simultaneously at work contributing to this spectral variability. Interestingly, these problems for young stars have essentially only been studied and discussed in the case of MS or PMS stars. Our sample allow to shows clearly for the first time that the effect(s) extend also to giants. Indeed, this is not surprising, as the challenges posed by the modeling of atmospheres and spectra for giants are even more severe than those for dwarfs.

6.3 Elemental ratios and the disk

The α-elements primary production site are SNII, whose progenitors are massive stars ($\gtrsim$8-10 M$_\odot$). In old Milky Way populations, stars are generally enriched in α elements, [α/Fe]=$\sim$ 0.3 − 0.6, dex while in younger populations the situation is more nuanced, with generations of SNIa having increased the Fe content, decreasing the [α/Fe] ratio (see Matteucci, 2021, and references therein). Therefore, probing the α-elements offers a way to gain insight on the history of the chemical enrichment of a population, and in this case, through the present sample, to investigate those processes in the thin disk.

Galactic chemical evolution models can be constrained by trends in the chemical abundances with Galactocentric radius and age, as well as by variations of these trends with time and with metallicity. Our SPA sample of OCs is distributed over the range $7700 < R_{GC} < 10000$ pc, and within 0.5 kpc from the disk, with ages from 40 Myr to 4.2 Gyr. The distribution, however, is not uniform, with most objects in the sample being young (< 1.5 Gyr) and concentrated in the 8-10 kpc zone.

In the following subsections we discuss the distribution of α-elements, Na and Al with respect to their distances from the Galactic center and the Galactic plane, and age. Results are also complemented by measurements obtained by literature works on (APOGEE, Gaia-ESO, GALAH, OCCASO, see Zhang et al. 2021 for the appropriate references) and for field stars (APOGEE DR17, Leung & Bovy 2019 and the HARPS-GTO sample, presented in Adibekyan et al. 2012) and compared to the Minchev, Chiappini & Martig models (the chemo-dynamical thin-disc model by Minchev et al. (2013, 2014b).) for the formation of the Galactic disk.

6.3.1 Abundance of Clusters and field stars

It is interesting to compare our results for OC stars to those derived for field disk stars. The HARPS-GTO program provides high quality spectrum on dwarf field stars in solar vicinity. We adopt the atmospheric parameters and chemical abundance derived by Adibekyan et al. (2012), which provide measurements for all the elements relevant to the present paper, with the exception of O, and the age determined from Delgado Mena et al. (2019). We adopt the Minchev et al. (2018) temperature, age and Mg quality cuts (5300-6000 K and δ [Mg/Fe] < 0.07 dex, δ Age/Age<0.25 or δAge < 1 Gyr.), aimed at selecting a reliable sample representing the local field.

Figure 6.8 shows the behavior of α-elements, as a function of metallicity, in our clusters and in the HARPS-GTO field sample. Symbols are color coded according to age. We plot O, Mg, Si, Ca, Ti, and the average of [α/Fe], defined as the mean abundance of Si, Ca, Ti, and Mg weighted by the errors.

Our clusters belong to the thin disk and are typically quite young, while there is a general scarcity of stars of similar ages in the HARPS-GTO sample. The overall [α/Fe] distribution is in reasonable agreement with the lower edge of the distribution of the field stars (which, as can be seen from the plot, corresponds to the younger objects, which are however still considerably older than the bulk of
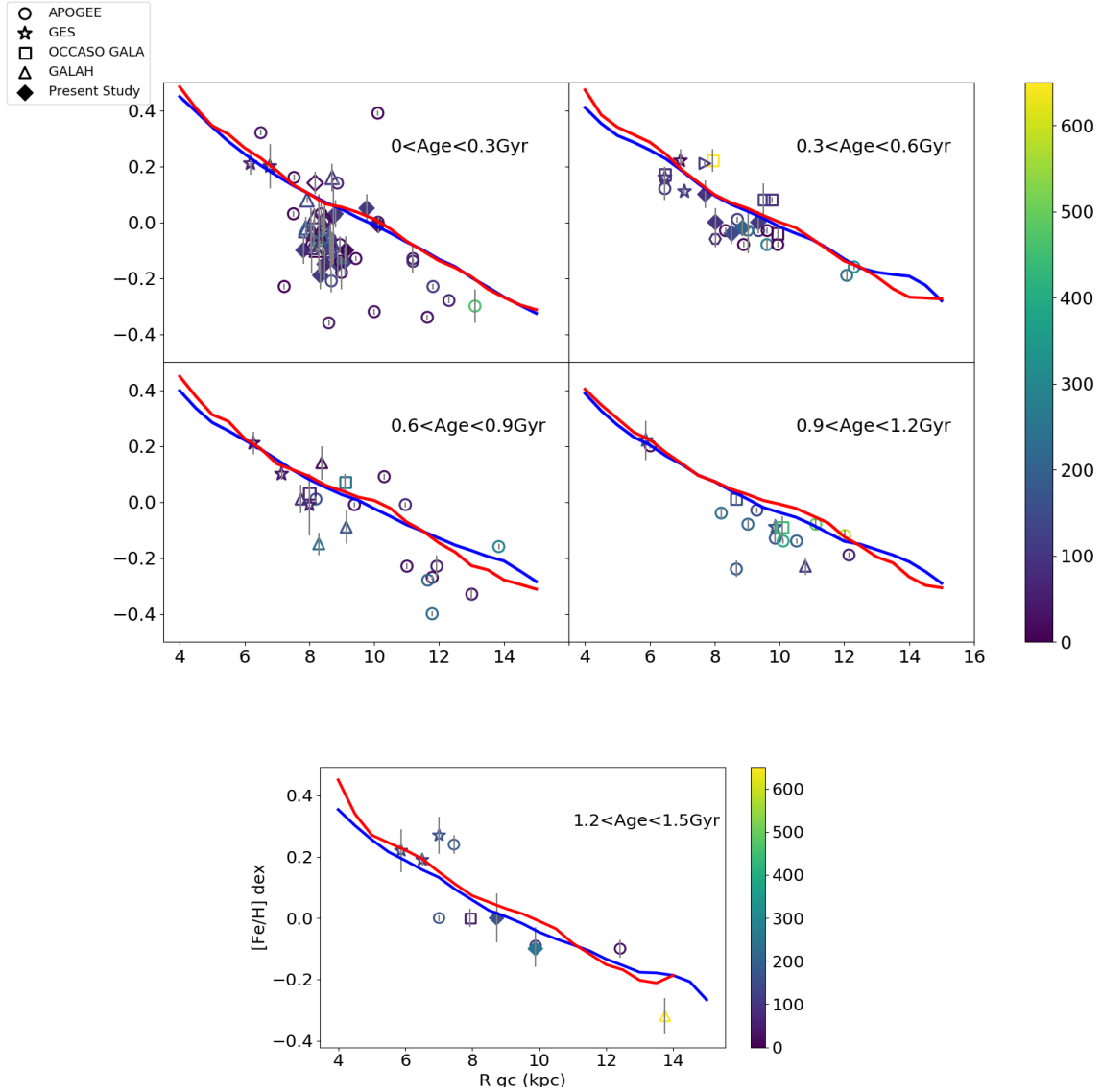
Figure 6.5: Comparison between model predictions (Minchev et al., 2014a,b) and observation for young clusters. The red and the blue lines are predictions from the MCM models for $|z| < 0.3$ kpc and $0.3 < |z| < 0.8$ kpc respectively. The colours in the symbol indicates the distance from the Galactic plane. All considered clusters are within 0.6 kpc from the Galactic plane, with SPA clusters being all within 0.5 kpc. The open 'diamond' in the first panel is ASCC 123 (Frasca et al., 2019) and the 'triangle' symbol in 0.3-0.6 Gyr range is NGC 2632 (D'Orazi et al., 2020) The fit is generally good for clusters older than 0.3 Gyr, but the predictions fail to reproduce the data among the very young clusters (see text).
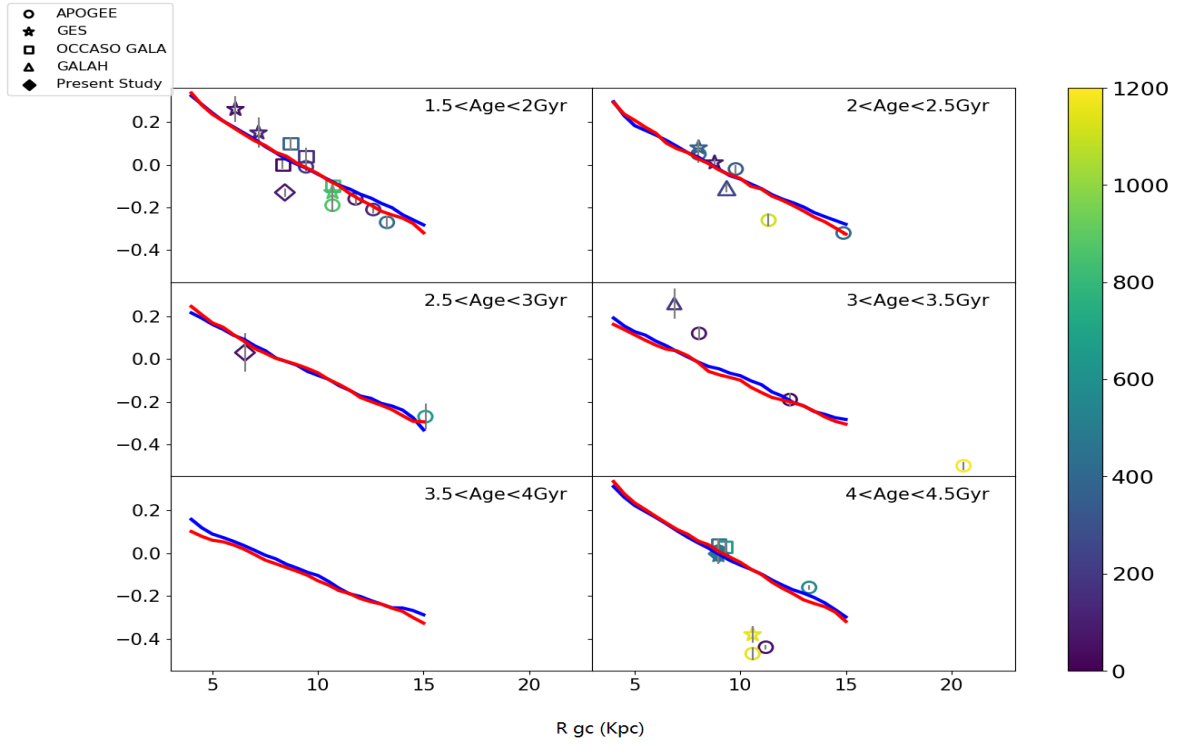
Figure 6.6: As in Fig. 6.5 for clusters bewteen 1.5 and 4.5 Gyr. Note the paucity of OCs older than 2.5 Gyr (in particular, only one SPA cluster is present, Ruprecth 171, from Casali et al. 2020). The data are quite well reproduced by the models; the exceptions are the old and very metal poor clusters which have $|z| > 1$ kpc, further away from the Galactic plane than the plotted models.
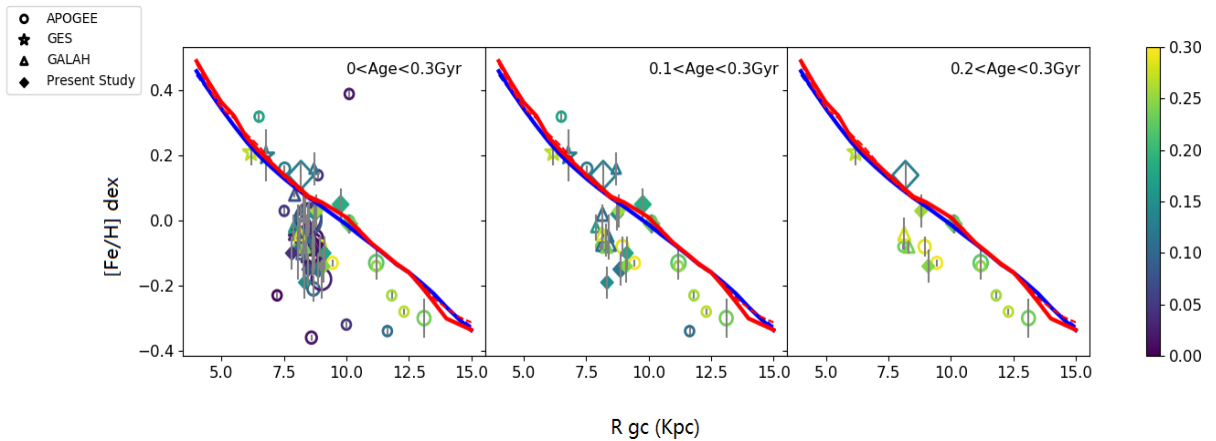
Figure 6.7: As in Fig 5, but colour coding the symbols by their age.The size of the symbols is proportional to the number of stars studied in the cluster to obtain the mean value reported here. (The open diamond represents ASCC 123 from Frasca et al. (2019)). The left panel shows all the clusters younger than 300Myr, while the middle and right panels show the fit without clusters younger than 100Myr and 200Myr, respectively. The fit to the models is quite reasonable when considering clusters older than 200Myr.

our sample). Magnesium and Ca are systematically lower, while Si appears a little higher, and Ti in good agreement.

Adibekyan et al. (2012) adopts Anders & Grevesse (1989) for the solar reference abundance, for which Mg, Si and Ca are in excellent agreement with Asplund et al. (2009).

A similar comparison was performed by Casamiquela et al. (2019) for the OCCASO data. They found better agreement for Ca and Mg in the OCCASO sample, however their sample has an older age distribution, with more than 60% of the clusters having Age >1 Gyr, while 15 out of our 18 clusters are below that age. It is worth noting, that the oldest clusters in our sample Alessi 1, NGC 2509 and NGC 2682, with ages 1.5, 1.4 and 4.3 Gyr, respectively, are generally in good agreement with behavior of the oldest among the field stars.

The mismatch between the elemental ratios for Mg, Ca, Si, and Ti in the clusters and in the field could be due to the lack of stars of suitable age in the field sample or to systematic effects related to the analysis of very young stars, or a combination thereof. Paper I discusses the effects on Fe measurements, this will also be discussed in section 3.4 regarding other elements.

The comparison with Na and Al shows a clear mismatch of Na, while for Al, cluster and field star are in fair agreement. We note, however, that Na is known to be affected by stellar evolution (see Section 3.2), with giants being enhanced to different degrees with respect to their main sequence phase. Therefore, we expect that our sample will be characterised by higher Na content with respect to dwarfs, which is consistent with the lower panel of Fig. 6.8.

The other comparison based on the field giant selected from APOGEE DR17 with the criterion from 6.1.1. The APOGEE thin disk giants sample is typically younger and shows a larger scatter in the abundances of all species compared to that observed for the HARPS GTO sample. Still, the thin disk giant sample contains just 300 stars below 500 Myr and just 7 below 300 Myr.

Overall, there is general agreement between the abundances measured in our sample and the APOGEE thin disk giants, as can be seen from Fig. 6.9, especially when considering the youngest among the disk stars. We note, however, that Mg and and Ca are still lower in the clusters than in their field counterpart, an effect that also affects the average [α/Fe]. The abundances of Mg and Ca seem to decrease in clusters closer to the Galactic Center. This trend is expected by chemo-dynamical models (see sec 4.4), but interestingly it seems to not to be consistent with the abundances found in the field. We note that Casamiquela et al. (2019) finds a discrepancy in the same direction in Mg their sample when comparing to APOGEE data. Similarly, Magrini et al. (2018), reported an enhancement, however this is found for clusters in an inner Galactic position than the SPA OCs. For O and Si, some of the youngest clusters reach values higher than observed in the field, while Ti is in good overall agreement, and the same is true for Na and Al, which however have very large scatters in the APOGEE, a fact possibly due to evolutionary effects but also to more uncertain measurements.

6.3.2   Distributions of elemental ratios with respect to $\mathbf{R}_{GC}$ and |$\mathbf{Z}$|

In order to explore the Galactic disk properties, probe its formation and provide constraints to model of its formation, elemental ratios for open clusters from multiple sources were collected in an extended sample, to cover a wider range of distances from the Galactic Center and the disk, metallicity and ages, than available in our SPA sample. We included results from APOGEE ([X/Fe] and distance from Donor et al. 2020, |Z| from Cantat-Gaudin et al. (2020)), Gaia-ESO ([X/Fe], distance, and |Z| are from Casali et al. 2019), GALAH ([X/Fe], distance and |Z| are from Spina et al. 2021 for all clusters not already in the APOGEE sample) and OCCASO (Casamiquela et al., 2019).

Furthermore, we included all the other clusters from the SPA project, as analysed by D'Orazi et al. (2020) Frasca et al. (2019), Casali et al. (2020), and Alonso-Santiago et al. (2021). The resulting
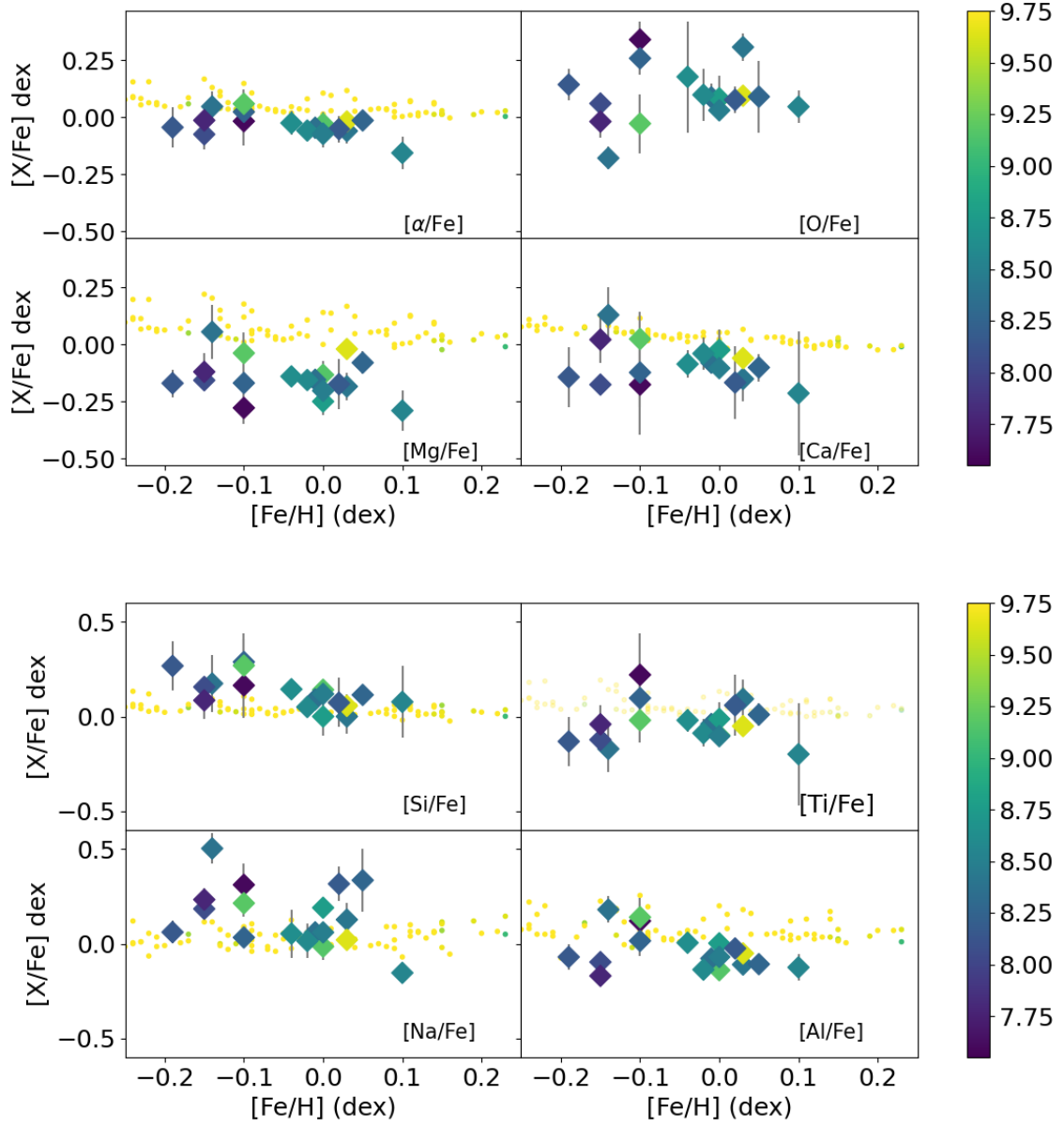
Figure 6.8: The relationships between [Fe/H], the α elements (including [α/Fe] defined as the average of Mg, Ca, Si and Ti indexed against Fe), Na and Al colored by log (Age). The small dots are for the HARPS-GTO samples. O abundances are not available for the HARPS-GTO sample.
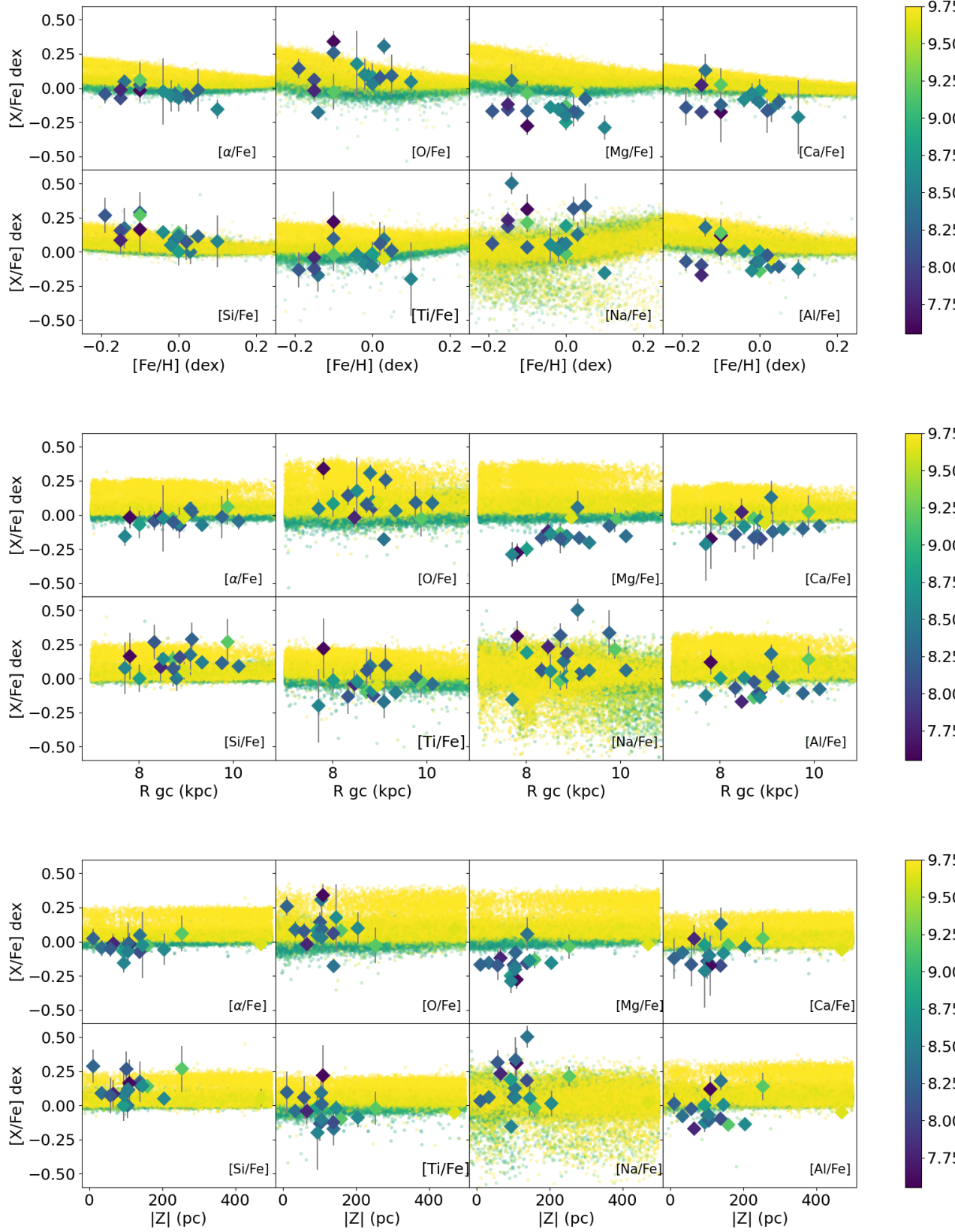
Figure 6.9: Average [X/Fe] as function of [Fe/H], R_{gc} and |Z| for the SPA OCs, colored by log (Age) and with uncertainties in chemical abundances indicated. The field giant stars (small dots, also colored with age) are selected from APOGEE DR17.

collection is made up of a total of 152 clusters, covering the age range 4 Myr-7 Gyr, the Galactocentric range from 5.8 to 20 kpc, distance from the Galactic plane |Z| up to 1750 pc, and a range from -0.5 to 0.4 dex in [Fe/H].

Figures 6.10 and 6.11 show the behavior of the measured abundance ratios with respect to R_{GC} and |Z|, split in three age bins, which have been chosen to match those used by Minchev et al. (2014b). Most of the objects in the combined sample are younger than 2 Gyr. The older age bins are populated mostly by APOGEE and GALAH OCs, with a small contribution from the present study (one cluster), Gaia-ESO (one cluster) and OCCASO (three clusters). We note that in the youngest bin there is not only more scatter, but also systematic differences among different sources. This will be discussed further .

We derived the Galactocentric and vertical gradients of α-elements, Na, and Al following the same approach of Paper I for what concerns grouping clusters by distance and age[2]. Abundances for clusters that had measurements from more than one source were combined using a weighed mean before deriving the gradients. Gradients were calculated using a linear fit, weighting according to the associated uncertainties. We note that the combination of data from different sources is very likely to be affected by systematic errors in ages, abundance ratios, and distances. We note that while we took the utmost care in minimising it, there were only a limited number of stars/clusters in common which could be checked for offsets, covering only a fraction of the relevant parameter space. Table 6.3 shows the gradients of [X/Fe] with distances. The bins for older clusters (>2 Gyr) and/or distant clusters are very scarcely populated, but we calculated the gradients in those bins for completeness.

Data for O, Na, Al, Si, and Ti are consistent with a flat distribution wrt Galactocentric distance and distance from the mid-plane. Casamiquela et al. (2019) reached the same conclusion for Si and Ti (they do not present the analysis for O, Na and Al). On the other hand, Donor et al. (2020), using the APOGEE sample, finds flat distributions for Si and Ti, but small positive statistically significant gradients for O and Al and negative for Na. It is worth noticing that the APOGEE sample has a different age distribution from the combined sample we are using, which contains a larger fraction of very young clusters. However, we do not find any significant trend for O, Na or Al even when computing the trends on the basis of clusters older than 1 Gyr in the combined sample.

For Mg and Ca we derive statistically significant gradients, and in both cases their values are consistent when considering the whole sample or just clusters younger than 2 Gyr, within the statistical errors. The value for the radial gradient of Mg is in perfect agreement with that reported in Casamiquela et al. (2019), 0.01±0.002 dex kpc^{-1}, and Donor et al. (2020), 0.009±0.001 dex kpc^{-1}. For Ca Casamiquela et al. (2019) finds no significant gradient, while we find a significant positive trend, a finding similar to Donor et al. (2020), who reports an even steeper value (0.012±0.0001 dex kpc^{-1}). Even in this case, excluding the 18 clusters from this paper from the combined sample does not significantly affect the value.

For the gradients with distance from the mid-plane, we also find significant trends only in Mg and Ca. Several literature works (e.g. Sharma et al., 2021; Lee et al., 2011; Bovy et al., 2012a,b,c) discuss how probing stars in a range of vertical mid-plane distances reveal the bimodality in [α/Fe]-[Fe/H] distribution giving indication on the structure of the disk(s).

Boeche et al. (2014) derived vertical gradients for α elements on the basis of a sample of field red giants from RAVE, Hayden et al. (2015) uses APOGEE data to investigate α content at different heights on the Galactic plane. They both find the α increases with increasing |Z|, consistently with the

---

[2]Note that for Si and Ca, Gaia-ESO clusters younger than 2 Gyr were excluded from the gradient derivation, as they seem affected by a negative offset (see next section for details). However, including them in the sample would not have affected the qualitative result.

gradients we determine for Mg and Ca.

6.4   Elemental ratios and age

Ages can be reliably determined in OCs, unlike in field stars. Therefore, they are ideal tools to investigate the chemical evolution of the disk. In this section, we explored the chemical trend with ages through the combination samples. To ensure homogeneity, all the ages for the SPA OCs and for the combined sample are from a single source, Cantat-Gaudin et al. (2020).

Figure 6.12 plots the abundance ratios of chemical abundance as a function of OCs' ages, colored according to their source. We note that for some elements the behaviours are quite different depending on their source. Aluminum and Na appear somewhat lower in APOGEE young clusters, an effect which might be due to the fact that both are derived without accounting for NLTE effects. For Si and Ca, Gaia-ESO reports abundances in very young clusters that are on average lower than those in the other works considered here. The average Gaia-ESO abundances for Si and Ca for clusters younger than 2 Gyr are -0.46 ± 0.14 and -0.23 ± 0.09. This has to be confronted to OCCASO (0.03 ± 0.05 and 0.04 ± 0.01, respectively), APOGEE (-0.02 ± 0.07 and 0.02 ± 0.08, respectively), GALAH (-0.02 ± 0.04 and 0.09 ± 0.05, respectively) and the SPA sample (0.13 ± 0.08 and -0.08 ± 0.09, respectively). Indeed, there is a considerable systematic difference, which is not observed for other elements. The disagreement seems much less severe among older clusters (age > 2 Gyr) and in particular all sources are in very good agreement for keystone clusters, such as NGC 2682 (keeping in mind the different approaches to the treatment of NLTE effects for Na and Al).

Even taking into account these offsets, and hence not considering the Gaia-ESO data for Si and Ca, it is clear that the scatter in the elemental ratio increases with decreasing age for all elements. This is expected to some extent: very young clusters are expected to have different composition depending on their birth position, with clusters at large R_{GC} being typically more metal poor and having higher $[\alpha/\text{Fe}]$ wrt those forming in the inner disk, see e.g. Chiappini (2009) and Figure 12 in Casamiquela et al. (2019). However, the effect should be of rather modest magnitude, smaller than what can be noted from Fig. 6.12, suggesting the existence of some other cause.

On the other hand, the disagreement could be related to the fact that traditional 1-D analysis is inadequate for very young stars, as discussed in Paper I in the case of Fe, see also next section for further discussion. However, we note that the differences extend beyond the range expected to be affected by these issues, hinting at the fact that the derivation of abundances in young stars might be particularly sensitive to the detailed assumptions made by different approaches to the analysis, including the choice of model atmospheres, path to the derivation of the atmospheric parameters and the specific transitions on which the abundance measurements rely.

We derive the gradients with age for the α-elements, Na, and Al for the combined sample, and for just our 18 clusters. Gradients are listed in Table 6.4. It is important to keep in mind in this context that the SPA sample is heavily biased towards young clusters, lessening the significance of age gradients based just on such sample.

Data are consistent with a flat distribution with age for Na, Si, and Ti, both for the combined sample and for just the 18 clusters presented in this paper. For O and Al, the combined sample shows a statistically significant positive gradients. For Mg and Ca, positive gradients are present both in the combined sample and in the sample of the 18 present clusters.

Our findings are in qualitative agreement with Casamiquela et al. (2019), who do not report the values of the derived trends but show the associated plots. Yong et al. (2012) measured the age gradients for a number of α, Fe-peak elements and n-capture elements, finding a significant gradient
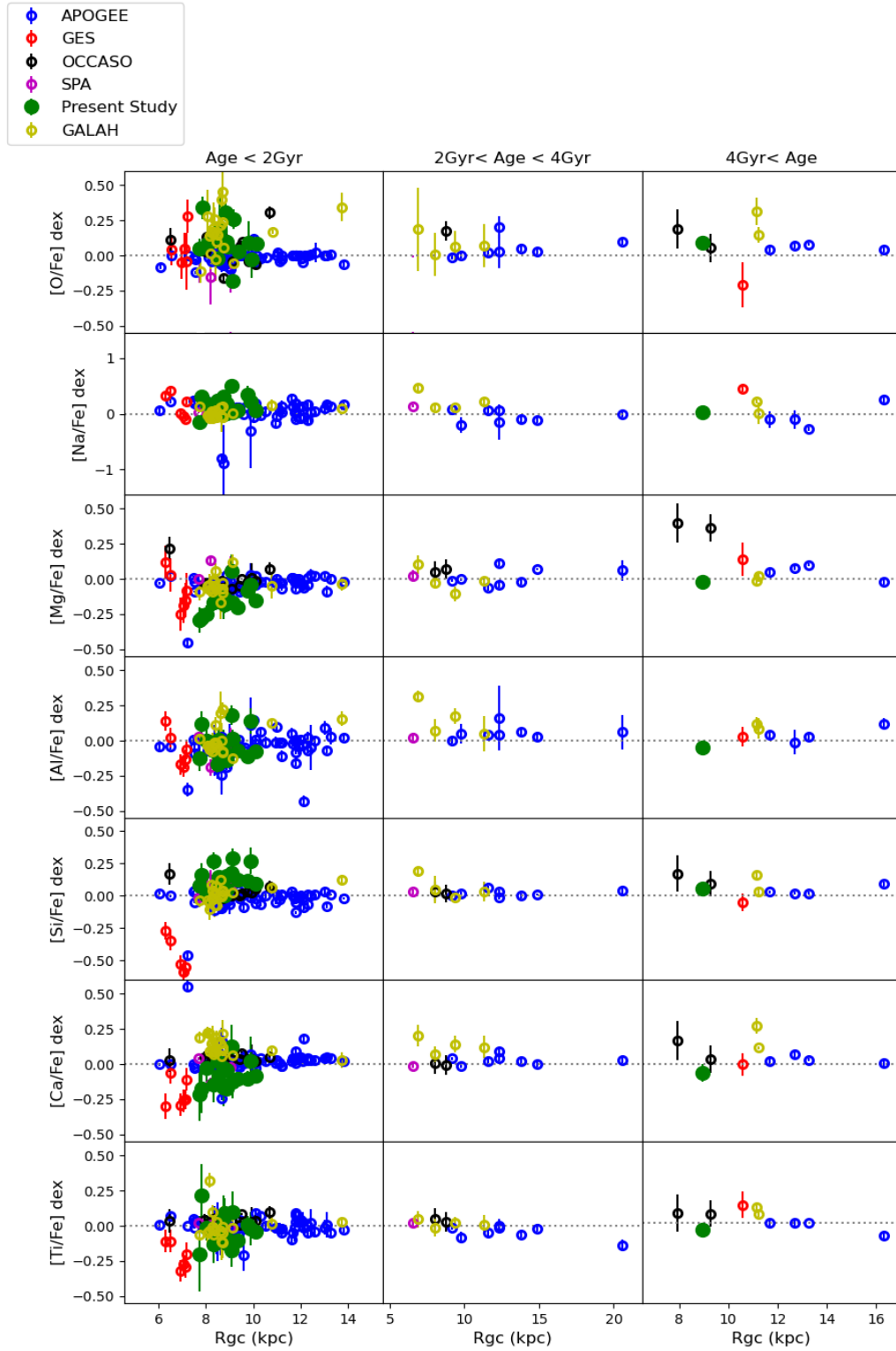
Figure 6.10: The distribution of abundance ratios with Galactocentric distance in three age bins (the same used in Minchev et al. 2014b, see Sec. 5.2). Beside our clusters, we show data from APOGEE (Donor et al., 2020), GES (Casali et al., 2019), OCCASO (Casamiquela et al., 2019),and GALAH (Spina et al., 2021) plus SPA results already published (Frasca et al., 2019; Casali et al., 2020; D'Orazi et al., 2020).
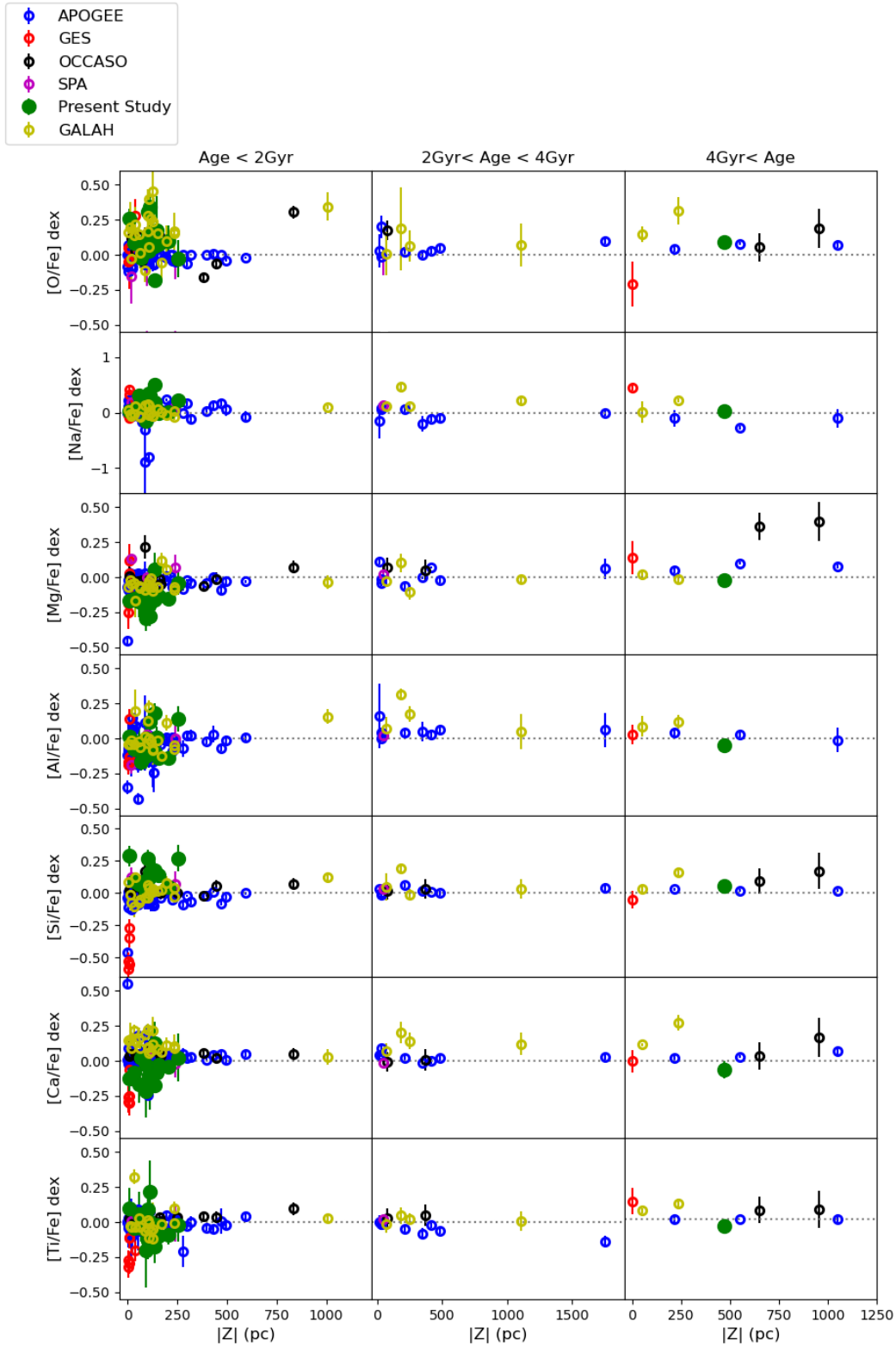
Figure 6.11: The distribution of abundance ratios with distance from mid-plate in three age bins (the same used in Minchev et al. 2014b, see Sec. 5.2). Beside our clusters, we show data from APOGEE (Donor et al., 2020), GES (Casali et al., 2019), OCCASO (Casamiquela et al., 2019),and GALAH (Spina et al., 2021) plus SPA results already published (Frasca et al., 2019; Casali et al., 2020; D'Orazi et al., 2020).
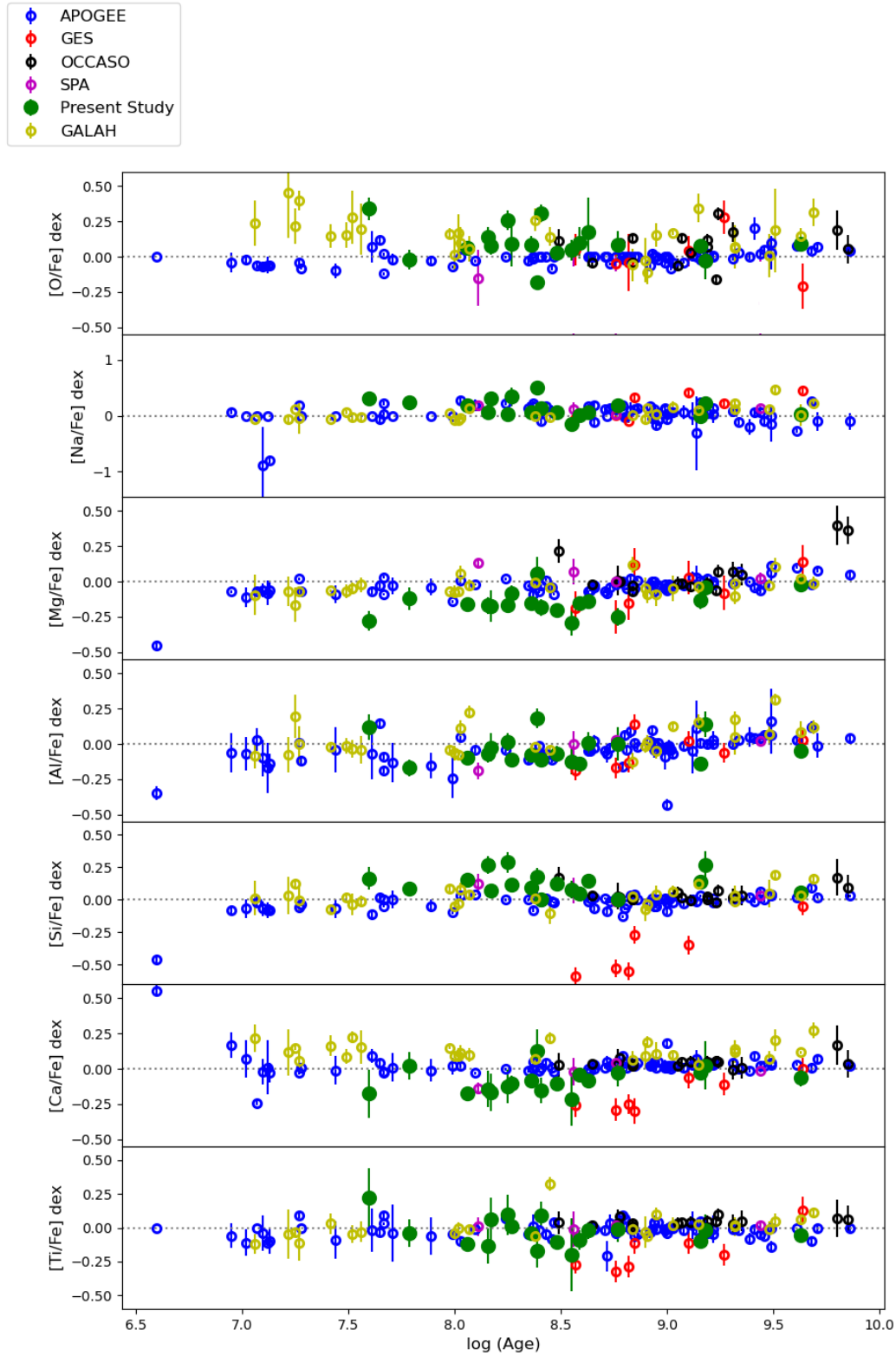
Figure 6.12: The distribution of abundance ratios with age. Beside our clusters, we show data from APOGEE (Donor et al., 2020), GES (Casali et al., 2019), OCCASO (Casamiquela et al., 2019),and GALAH (Spina et al., 2021) plus SPA results already published (Frasca et al., 2019; Casali et al., 2020; D'Orazi et al., 2020).

for Mg, even if flatter than ours, but not for Ca. They also found significant trends for Na and Al, derived without accounting for NLTE effects.

6.5   Comparison with chemo-dynamical models for Mg and O

Comparison of the measured abundance ratios with theoretical predictions provides insight on our understanding of the processes that lead to the formation of the disk. In this context, we use the state of the art chemo-dynamical models computed by Minchev et al. (2013, 2014b, hereafter MCM). They combine chemical evolution from Chiappini (2009), describing how the composition of stellar populations change with time, with the movement and mixing processes affecting stars and gas, including stellar migration and mergers.

Surveys of the disk field stars and large samples of stellar clusters, such as the our combined sample, generally span considerable ranges in distance, height on the Galactic mid plane and ages, and measured trends and gradients are affected by the motions experienced by stars and clusters. Therefore, the combination of dynamics and chemical evolution in the models is crucial for a meaningful comparison with the observations.

In the following plots, the MCM models of the thin disk are rescaled so that the most likely birth position for the Sun (R_{GC} = 6 kpc, 4.5 Gyr ago) matches the solar composition (see Minchev et al. 2013).

Figures 6.13, 6.14, 6.15, and 6.16 show the comparison of observational data with the predicted result for [Mg/Fe] and [O/Fe] in the age range from 0-4.5 Gyr. The age bins are 0.3 Gyr for the younger ages (up to 1.5 Gyr) and 0.5 Gyr for older objects. The MCM models are computed at two different distances from the midplane: $|Z|$ < 0.3 kpc (blue lines) and 0.3< $|Z|$ < 0.8 kpc (red lines).

We are limiting our comparison to O and Mg, as those are the only one fully published at this time. Magnesium seems to be overall well reproduced by models. For young clusters (age<0.6 Gyr), the data show a higher Mg content than predicted by the MCM models. It is worth noticing that our data (the 18 SPA OCs) are actually better reproduced by the model than the literature values (see upper left panel in Fig. 6.13), which report Mg abundances higher than the predictions for clusters younger than 0.6 Gyr.

The vertical Mg gradient for the MCM simulation for clusters with age < 2 Gyr, 0.028 dex kpc^{-1}, is in good agreement with the value calculated on the basis of the young clusters in the combined sample, 0.034±0.024 dex kpc^{-1}.

For O, the match of predictions is poorer, there is considerable scatter in the youngest bin, and generally the O abundances for our SPA sample and the literature are higher than what the models predict.

As mentioned in Section 6.4, the discrepancy between observations and model predictions, and the offsets among different sources, are found in particular among very young clusters.

In Paper I we discussed the issues in measuring Fe abundances in very young stars, likely related to effects that are generally neglected in modeling of stellar atmospheres (e.g. chromospheric activity, magnetic fields etc). These effects are discussed in the literature as being at play in very young dwarfs (Yana Galarza et al., 2019; Baratella et al., 2020; Spina et al., 2020), making inadequate the derivation of atmospheric parameters through the traditional 1-D LTE analysis based on minimising trends for Fe lines. Our sample showed how these effects extend to giants (see Paper I) for what concerns iron. It is thus reasonable to expect that similar issues would plague the derivation of other species, providing a possible explanation for the large scatter observed among the youngest objects (age below ∼200 Myr). Our data confirm this expectation.

This means that the mismatch between models and observations in very young clusters is of scarce astrophysical meaning; significant insight on the very young disk will require the application of a different path to abundance analysis, an approach taken by e.g. Baratella et al. (2020) for very young dwarfs, and/or more realistic model atmospheres accounting for chromospheric activities and magnetic fields.

We are not sure the model has such accurate, consider the error of the prediction, the systematic bias is expectation. Data for intermediate age and old clusters are generally in very good agreement with models for those ages, which are the evolution of the earlier (younger) models, making it unlikely that any fundamental issue is plaguing them.
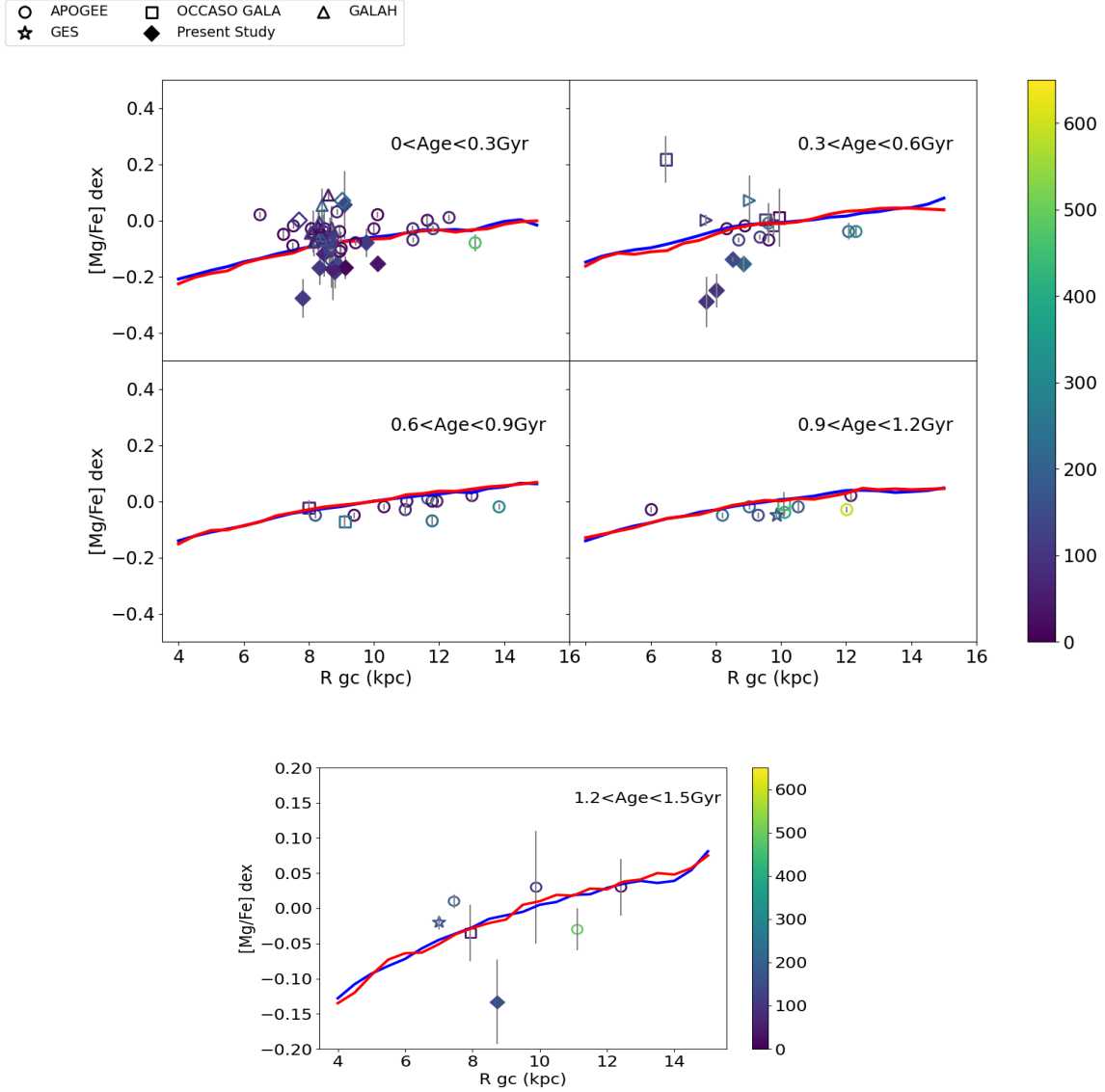
Figure 6.13: Comparison between model predictions of magnesium (MCM model) and observation for clusters younger than 1.5 Gyr. The red and the blue lines are simulations from the MCM models for $|z| < 0.3$ kpc and $0.3 < |z| < 0.8$ kpc respectively. The colours in the symbol indicates the distance from the Galactic midplane. All clusters are within 0.6 kpc from the Galactic plane, and SPA clusters are all within 0.5 kpc. The open 'diamond' in the first panel is ASCC 123 (Frasca et al., 2019) and the 'triangle' symbol in 0.3-0.6 Gyr range is NGC 2632 (D'Orazi et al., 2020)
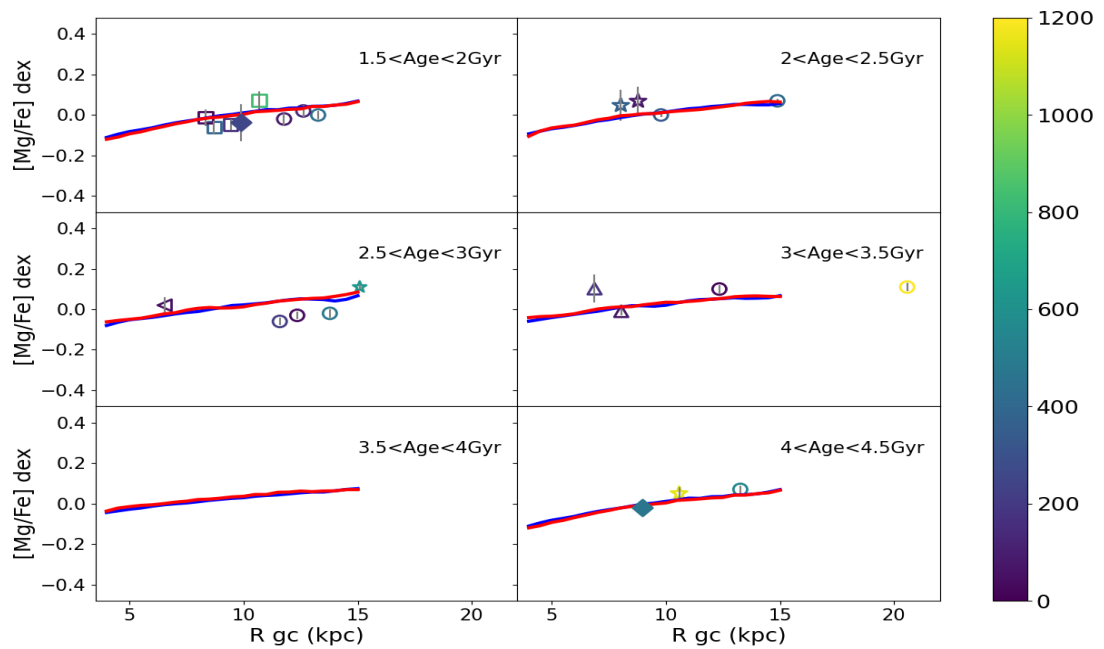
Figure 6.14: As in Fig. 6.13 for clusters between 1.5 and 4.5 Gyr. Only one SPA cluster is older than 4 Gyr, Ruprecth 171, from Casali et al. 2020).
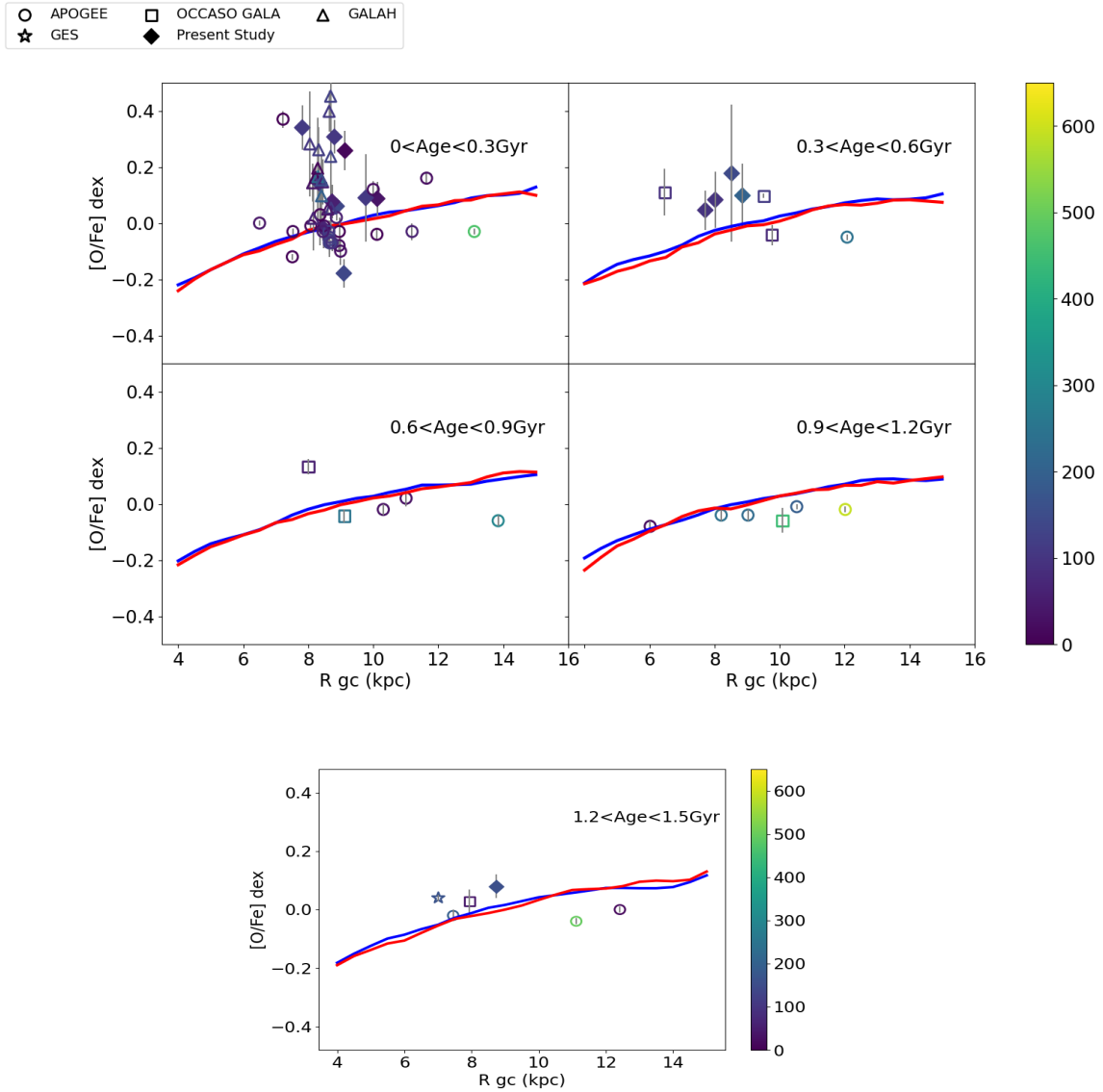
Figure 6.15: The comparison as Fig. 6.13 and 6.14 for oxygen between prediction (MCM model). and observation result for young samples.
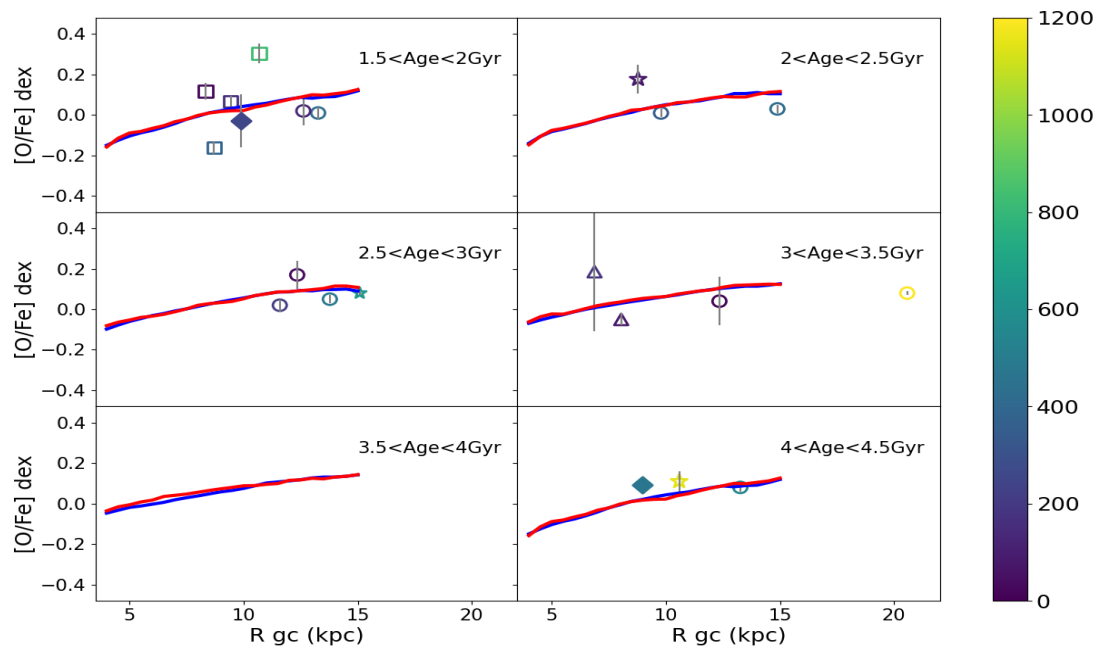
Figure 6.16: The comparison for oxygen between prediction and observation for OCs older than 1.5 Gyr.

Table 6.3: Observed gradients of α-elements and Na, Al (with NLTE correction).

Age range (Gyr)	R_{gc} (kpc)	d[O/Fe]/dR_{GC} (dex kpc^{-1})	d[O/Fe]/d$|z|_{GC}$ (dex kpc^{-1})	$N_{clusters}$
all ages	Rgc<14	0.0030 ± 0.0060	0.0506 ± 0.0271	111
age<2	Rgc<14	0.0506 ± 0.0271	-0.0261 ± 0.0266	91
2<age<4	Rgc<14	0.0121 ± 0.0028	0.0943 ± 0.0467	13
age>4	Rgc<14	0.0006 ± 0.0160	0.0130 ± 0.0531	9

Age range (Gyr)	R_{gc} (kpc)	d[Na/Fe]/dR_{GC} (dex kpc^{-1})	d[Na/Fe]/d$|z|_{GC}$ (dex kpc^{-1})	$N_{clusters}$
all ages	Rgc<14	0.0013 ± 0.0052	0.0026 ± 0.0057	117
age<2	Rgc<14	0.0064 ± 0.0058	0.0290 ± 0.0676	99
2<age<4	Rgc<14	0.0227 ± 0.0103	0.0271 ± 0.1176	11
age>4	Rgc<14	-0.1041 ± 0.0635	-1.0445 ± 0.2437	5

Age range (Gyr)	R_{gc} (kpc)	d[Mg/Fe]/dR_{GC} (dex kpc^{-1})	d[Mg/Fe]/d$|z|_{GC}$ (dex kpc^{-1})	$N_{clusters}$
all ages	Rgc<14	0.0099 ± 0.0017	0.0703 ± 0.0191	144
age<2	Rgc<14	0.0095 ± 0.0017	0.0340 ± 0.0244	122
2<age<4	Rgc<14	-0.0052 ± 0.0050	-0.0024 ± 0.0410	13
age>4	Rgc<14	0.0270 ± 0.0093	0.0713 ± 0.0708	9

Age range (Gyr)	R_{gc} (kpc)	d[Al/Fe]/dR_{GC} (dex kpc^{-1})	d[Al/Fe]/d$|z|_{GC}$ (dex kpc^{-1})	$N_{clusters}$
all ages	Rgc<14	0.0074 ± 0.0039	0.0961 ± 0.0354	127
age<2	Rgc<14	0.0079 ± 0.0031	0.1017 ± 0.0406	109
2<age<4	Rgc<14	0.0037 ± 0.0029	0.0941 ± 0.0696	11
age>4	Rgc<14	0.0188 ± 0.0075	-0.0741 ± 0.0737	7

| Age range (Gyr)	R_{gc} (kpc)	d[Si/Fe]/dR_{GC} (dex kpc^{-1})	d[Si/Fe]/d$|z|_{GC}$ (dex kpc^{-1})	$N_{clusters}$
all ages	Rgc<14	-0.0011 ± 0.0017	0.0148 ± 0.0157	135
age<2	Rgc<14	-0.0027 ± 0.0019	-0.0092 ± 0.0266	113
2<age<4	Rgc<14	-0.0035 ± 0.0026	0.0214 ± 0.0393	13
age>4	Rgc<14	-0.0089 ± 0.0030	-0.0142 ± 0.0211	9

Age range (Gyr)	R_{gc} (kpc)	d[Ca/Fe]/dR_{GC} (dex kpc^{-1})	d[Ca/Fe]/d$|z|_{GC}$ (dex kpc^{-1})	$N_{clusters}$
all ages	Rgc<14	0.0055 ± 0.0015	0.0424 ± 0.0188	135
age<2	Rgc<14	0.0050 ± 0.0018	0.0547 ± 0.0250	113
2<age<4	Rgc<14	0.0026 ± 0.0049	-0.0392 ± 0.0805	13
age>4	Rgc<14	-0.0282 ± 0.0224	-0.1015 ± 0.0664	9

Age range (Gyr)	R_{gc} (kpc)	d[Ti/Fe]/dR_{GC} (dex kpc^{-1})	d[Ti/Fe]/d$|z|_{GC}$ (dex kpc^{-1})	$N_{clusters}$
all ages	Rgc<14	-0.0033 ± 0.0021	0.0055 ± 0.0222	150
age<2	Rgc<14	-0.0027 ± 0.0025	0.0277 ± 0.0299	116
2<age<4	Rgc<14	-0.0104 ± 0.0029	-0.0767 ± 0.0413	13
age>4	Rgc<14	0.0030 ± 0.0198	-0.0639 ± 0.0587	8

Table 6.4: The chemical gradient for the combined sample (second column) along with the number of clusters it is calculated on. The gradient for the 18 SPA OCs in the present paper is given in the last column.

Species	Combined sample d[X/Fe]/d(Age) (dex/Gyr)	n	Present sample d[X/Fe]/d(Age) (dex/Gyr)
O	0.018±0.004	114	0.008±0.011
Na	0.013±0.013	120	-0.031±0.040
Mg	0.029±0.004	147	0.036±0.007
Al	0.027±0.005	130	0.009±0.008
Si	0.007±0.002	135	-0.014±0.006
Ca	0.013±0.003	135	0.082±0.028
Ti	0.000±0.004	140	0.002±0.010

Chapter 7

Summary and prospects

In this work, we studied high-resolution, high quality spectra for 40 red clump stars in 18 OCs covering the Galactocentric distance range 7.7<R_{gc} <10 kpc. Almost all of them are young clusters, with 15 OCs between 40 and 600 Myr, two around 1.5 Gyr, and one (NGC 2682) at 4.2 Gyr. Their parameters were measured with the EW method and 1D-LTE atmosphere models. Then determined the abundance ratio of four α elements, O, Mg, Si, and Ca, as well as those of Li, Na, Al, and Ti.

(i) Very precise radial velocities with uncertainties of 0.05-0.25 km s^{-1} were measured. The offset between our results and that from Gaia DR2 is -0.11± 1.9 km s^{-1}.

(ii) Accurate stellar parameters were derived. For the stars located in the effective temperature range of 4200-5800 K uncertainties in T_{eff} are around 60 K, and 0.12 dex in surface gravity. All of the clusters have metallicity close to solar, with a deviation within 0.05 dex.

(iii) We compared five of our clusters (Collinder 350, NGC 2682, Tombaugh 5, NGC 2548, Basel 11b) with results from previous work, finding no systematic bias in our determination. A few discrepant cases were examined.

(iv) We explored the trend between metallicities and Galactocentric distance combining our data with clusters from APOGEE, GES, OCCASO, GALAH, and other SPA OCs (ASCC 123, Gulliver 51, Ruprecht 171, NGC 2632, NGC 7044). We confirmed the variation of slope in the metallicity gradient near R_{gc}=14 kpc and found a gradient slope for the inner disc similar to other literature works.

(v) We used the combined sample to compare to the chemo-dynamical predictions by Minchev et al. (2014a), finding good agreement for clusters older than 0.3 Gyr. Conversely, younger clusters show a large dispersion, not predicted by models, with observed metallicities too low for the Galactocentric position (not explainable by radial mixing, given the young cluster age).

(vi) We examined the cases of young clusters with low metallicity, finding that some results may be doubtful. However, there seems to be a general difficulty in deriving accurate metallicities for clusters younger than about 200 Myr, both for dwarfs (confirming literature works) and giants. We tentatively ascribe this to the impropriety of the traditional analysis for young stars, as discussed in the previous section.

(vii) Our sample does not contain any Li-rich giant. While the behavior of Li follows the overall expected depletion during the stellar ascent on the giant branch, abundances do show a clear scatter in Li abundance at any given Teff (or logg) across the parameter range, hinting at other factors playing a role (e.g. age, metallicity, binarity etc). Given the small parameter space covered by our sample, no further deduction was tried and we defer to dedicated studies, such as, for instance, those based on Gaia-ESO data for clusters and field stars (Magrini et al., 2021a,b; Romano et al., 2021).

(viii) We perform extensive comparison with the literature, both directly in terms of previously

studied clusters and field stars (HARPS-GTO nearby dwarf sample and APOGEE field disk stars). Overall, our results are in good agreement with literature clusters (five clusters in common), and the only significant offset, even if small, is observed for Mg among younger clusters, while such an offset is not observed for the keystone cluster NGC 2682. The comparison with field stars is of limited value as both HARPS-GTO and APOGEE disk giants samples have an age distribution quite different from our cluster sample, with a very limited number of stars spanning the appropriate age range. However, we observe no major offsets when considering the youngest among the APOGEE disk giants.

(ix) We considered the Na and Al abundances in our clusters to explore the behaviour of these elements with respect to stellar evolution and nucleosynthesis. We observe an overall mild increasing trend of Na_{NLTE} with respect to mass, in qualitative agreement with theoretical predictions, that are however calculated at metallicities that cover only the metal poor end of the distribution of our clusters. Our data span a larger Na range than the predictions, and seem to confirm an earlier suggestion from Smiljanic et al. (2016, 2018), based on a smaller sample, of the presence of some Na enhancement even among stars below $2\,M_{\odot}$. We find no convincing trend for Al with stellar mass, and the observations present a larger scatter than that spanned by models, especially for what concerns the most metal rich among the clusters in our sample.

(x) We investigate the Galactic gradients of abundances as a function of Galactocentric radius, distance from the Galactic midplane and age. In order to have a larger sample with a wider age distribution, we take into considerations also clusters from other recent studies (APOGEE, Gaia-ESO, GALAH, OCCASO) as well as clusters previously studied within the SPA program. We find a significant Mg radial gradient both for present-day (calculated for young clusters) and including all ages, in excellent agreement with recent literature. For Ca we also find a significant radial gradient, a value between those of Casamiquela et al. (2019), who reports a flat trend, and Donor et al. (2020).

(xi) Significant vertical positive vertical gradients were found for Mg and Ca, in agreement with commonly reported findings of increasing α-elements moving away from the thin disk.

(xii) Mg and Ca also show a significant age gradient, while all other elements are consistent with a flat distribution, in qualitative agreement with Casamiquela et al. (2019).

Finally, we have compared the Galactocentric distribution of Mg and O in the combined sample with state-of-the-art chemodynamical models. For clusters older than ~ 0.6 Gyr the overall distribution is very good agreement with results of the MCM models for both O and Mg. For younger clusters the observations show a larger scatter and the agreement with the models becomes poorer for Mg and especially for O.

While there is naturally room for improvement in the chemo-dynamical models, it seems likely that at least part of this effect is due to the unsuitability of traditional 1-D analysis and model atmospheres to derive atmospheric parameters and abundance ratios in very young giants, as effects of phenomena such as chromospheric activity and magnetic fields are not accounted for. These problems in young stars have essentially only been examined in the case of main sequence or pre-main sequence stars. Our findings show clearly for the first time that the effect(s) extend also to the derivation of Mg and O elemental abundances in giants. This is not a surprising result, in fact the modeling of atmospheres and spectra for giants is even more challenging than for dwarfs.

The optical spectral provides opportunities to probe the whole chemical compositions. In addition to the chemical elements presented in this work (Li, O, Mg, Si, Ca, Ti, Na and Al), other elements like light elements C and N, Fe-peak (V, Ni, Cr etc), neutron-capture elements (Y, Zr, Ba, La, Ce, Nd, Sm, and Eu) will be derived in follow-up works. The chemical composition for stars in the OC metallicity is a result of enrichment by stars of several generations, and most of the chemical elements are produced by neutron capture elements (the supernovae explosion may provide the r-process elements

and the s-process composition are from AGB stars), which may allow more elements to explore the stellar evolution models and chemo-dynamical models. Due to the star may be formed from the different systems (Marsakov & Borkova, 2005), the main chemical features are the effective tools to trace the galactic formation and probe the chemical enhancement. Accurate n-capture elements provide a reliable way to study the detail of the galactic disk, and stellar compositions help to investigate the substructures of the Milky Way and the evolution process.

As previously discussed, our findings seem to suggest that traditional 1D, LTE analysis is not suitable for giants as young as those included in our sample. Similar conclusions have been drawn in the case of dwarfs (see e.g. Yana Galarza et al., 2019; Baratella et al., 2020; Spina et al., 2020), suggesting as possible causes unaccounted for magnetic fields near the top of the stellar photosphere, Zeeman broadening and chromospheric activity. In the future it would be interesting to develop new approaches for the analysis of these object, devising a different path to derivation of atmospheric parameters and chemical abundance, analogously to what Baratella et al. (2020) has done for dwarfs.

A better approach to the analysis of young giants will become of particular importance in the few years. In fact, the next decade will bring considerable advancement in the field of the probing of the disk and of the overall characterization of the MW OC system, thanks in large part to the WEAVE and 4MOST programs dedicated to OCs, studying their giants with HR (R~20,000).

They will yield homogeneously derived chemical composition for key elements (Fe-peak, α and p-capture elements) for the vast majority of the 2500+ of currently identified OCs (and also a fraction of those that will be discovered with Gaia DR3). This is expected to allow to study spatial and age gradients and trends on the basis of large, homogeneous samples covering the whole range of relevant parameters, hence minimising the offsets affecting the combined samples which have generally been used so far for this purpose (see e.g. 6.3.2). Therefore, it will become crucial to be able to accurately derive parameters and chemical composition in young giants, as those will be the main uncertainties affecting the large samples of OCs abundances derived by WEAVE and 4MOST, hampering the capabilities of providing accurate estimates of the trends and of providing reliable constraints to the next generation of chemo-dynamical models.

Appendix A

Galactic surveys

This section provides brief information regarding surveys that are mentioned in the text.

SDSS-APOGEE surveys:

SDSS (Sloan Digital Sky Survey) is a sky survey that uses a 2.5 m modified Richey-Chretien altitude-azimuth mount telescope located in the southern hemisphere. That telescope with two observation models including photometric and spectroscopic with two correction lenses (Gunn et al., 2006). From now, SDSS contains four projects, however, in order to collect more complete data, some projects combined other telescopes in the northern hemisphere, the combination telescope are the Irénée du Pont Telescope at Las Campanas Observatory (Bowen & Vaughan, 1973) and the NMSU 1 m dome at Apache Point Observatory (Holtzman et al., 2010) . Four missions consist of the projects, APOGEE, BOSS, MARVELS, and SEGUE-2, in which the SDSS-APOGEE mission aimed to investigate the Milky Way in both hemispheres. Which observation across the whole Milky Way with the high-resolution spectrum at R=22500 in the near-infrared wavelength, with star magnitude at H around 12. The goals of this project are trying to answer the time line of star formation and the Milky Way composition enhancement, the age distribution of stars and the dynamical characteristics of disk, bulge and halo for the Galaxy. Otherwise, that will help to explore the differences between host stars with planet and the star without planet. Nowadays, SDSS-APOGEE has released 17th data, which contains information on radial velocities, stellar parameters, and chemical abundance, derived from the automatic pipeline.

Gaia:

Gaia is an ESA mission based on HIPPARCOS experience, which aimed at obtain large and precise data to mapping the Galaxy in three-dimension using 100 billion stars obtained astromical data (position and distance), photometric (luminosity) and spectral data (stellar parameter, and extinction). Gaia includes two telescope sharing the same focal plane with the two field of view ($1.7° \times 0.6°$). The magnitude limitation is r = 20, and the Gaia will collected broad-band G magnitude in the wavelength range from 3300 Å to 10200 Å. This instrument can also observe spectral distribution with low resolution in blue (wavelength in 5200 Å) and red wavelength (at 8000 Å). This catalog provide the detail information of chemical and dynamical for explore the stars birth from different systems with diversity histories, and the merge process of our Galaxy.

GALAH:

GALactic Archaeology with HERMES (GALAH) is a large program aimed to collect high-resolution spectral to build the multi-dimension datasets to help to explore the galactic formation and evolution with the multi-object Anglo-Australian Telescope using HERMES, which telescope can obtain 400 stars at one time. This program started on 7 February 2014 and ended on 27 September 2021. Now

more than 700000 stars are located in the galactic disk and galactic bulge has been collected. Which stars provide enough samples to detect the history of galactic chemical evolution and dynamic information and some of them are related to the accretion procedure. However, GALAH data allowed to detection of chemical composition homogeneously. Which dataset provides opportunities to trace back birth information of star, that related to explore the nucleosynthetic channels from different sources.

2MASS:

2MASS (The Two Micron All-Sky Surveys) aimed at collecting data (471 million sources) for the entire sky in the near-infrared wavelength (at 12500 16500 and 21700 Å) with the magnitude limits are J=15.8, H=15.1, and K=14.3. Investigating the Milky Way structure and census of star population near the solar. Which data including the photometric image and the source position, full-sky near-IR observation allows 2MASS to obtain the data penetrate the interstellar dust on the galactic plane and halo. Moreover, 2MASS collected more than 1000000 galaxies, which provide rich statistics data, and the near-IR wavelength allowed 2MASS obtain the data of cool and extremely red objects.

RAVE:

The Radial Velocity Experiment (RAVE) is a wide-field sky survey using a 1.2 m Schmidt Telescope to obtain the spectral data (R=8000) for million stars in the southern hemisphere, covering the wavelength range from 8410 to 8795 Å, with the magnitude limitation in 9< I <12 (Siebert et al., 2008) . The RAVE catalog includes the stellar parameters, accurate chemical abundance with a mean error is 0.2 dex (Boeche et al., 2011), and radial velocities , that project aimed at understanding the formation and evolution of the Milky Way combined stellar position, dynamic information, distance and proper motions.

LAMOST:

The Large Ares Multi-Object fiber spectroscope Telescope (LAMOST) is a 4 m reflecting Schmidt telescope with 4000 fibers. Covering the wavelength range from 3700 to 9000 Å with the spectral resolution are 500, 1000, and 1500 (Luo et al., 2015) . That surveys obtained the spectrum for million objects, which also aimed at galactic disk and open clusters surveys. That datasets for 10 million samples in the disk and halo provide the large homogeneous catalog to explore the formation and structure of the Milky Way (Wang et al., 2018) . The LAMOST catalog provide the stellar parameters and chemical abundance, those information determined from LAPS automatic pipeline.

SEGUE:

Solan Extension for Galactic Understanding and Exploration (SEGUE) is one of the projects based on SDSS that contains two project runs (SEGUE-1 AND SEGUE-2). From now, more than 200000 stars have been obtained by SEGUE-1 which spectral are used to investigate the galactic structure, and more than 100000 stars in galactic halo cover from 10 kpc to 60 kpc. The stellar parameters are determined by automatic pipeline. SEGUE-1 aimed to explore the history, stars' formation, kinematic and dynamic evolution, and chemical composition of the Milky Way (Yanny et al., 2009). And the second run of SEGUE provides the data from distance halo targets at K-giants, M-giants, stars located at the blue horizontal branch, the ages of special objects like old, cool white dwarfs, and ultra-cool dwarfs can be measured. Combined with those two projects, the structure of the Galaxy and outer region is mapped, and the data can be used to constrain the galaxy formation simulations.

A.1   Additional table

Table A.1: Sensitivity matrix of Li for all targets

Name	Δlog (Li)/Δ T$_{eff}$ (K)	Δlog (Li)/Δ log g (dex)	Δlog (Li)/Δ[Fe/H] (dex)	Δlog (Li)/Δ v$_{micro}$ (km s^{-1})
ASCC_11	0.040	0.021	0.041	0.039
Alessi 1_1	0.129	0.070	0.055	0.025
Alessi 1_2	0.059	-0.001	0.063	0.001
Alessi 1_3	0.038	0.062	0.081	0.032
Alessi 1_4	0.036	0.014	-0.012	0.013
Alessi Teausch_11	0.132	0.198	0.081	0.139
Basel 11b_1	0.042	-0.001	0.031	-0.001
Basel 11b_2	0.010	-0.052	0.018	-0.051
Basel 11b_3	-0.032	-0.053	0.220	-0.024
COIN Gaia_30	0.018	-0.024	-0.008	-0.049
Collinder 463_1	0.090	0.020	-0.007	0.001
Collinder 463_2	0.082	0.030	-0.006	0.013
Gulliver_18	0.177	0.073	0.004	0.003
Gulliver_37	0.111	0.156	0.029	0.331
NGC2437_1	0.042	-0.031	-0.005	0.013
NGC2437_2	0.027	-0.074	0.019	-0.023
NGC2437_3	0.066	-0.001	0.018	0.002
NGC2437_4	0.070	-0.002	0.019	0.001
NGC2437_5	0.025	-0.003	0.014	0.025
NGC2437_6	0.069	-0.003	-0.018	0.001
NGC2437_7	0.128	-0.010	0.030	-0.007
NGC2548_1	0.060	-0.001	0.030	0.049
NGC2548_2	-0.107	-0.152	-0.014	-0.024
NGC2548_3	0.227	0.021	-0.043	0.001
NGC2548_4	0.030	-0.001	0.007	0.000
NGC7082	0.064	0.018	-0.008	0.023
NGC7209_1	0.140	0.120	0.004	0.001
MGC7209_2	0.060	0.067	0.006	0.002
Tombaugh 5_1	0.083	0.046	-0.125	-0.075
Tombaugh 5_2	0.102	0.071	-0.031	0.026
Tombaugh 5_3	0.054	0.034	-0.006	0.026
UPK219	0.375	0.115	0.039	0.116
Comparison clusters				
Collinder 350_1	0.028	0.013	0.020	-0.003
Collinder 350_2	0.032	-0.001	0.018	0.013
NGC2682_2	0.162	-0.003	-0.043	0.001

Table A.2: Sensitivity matrix of O for all targets

Name	$\Delta[\text{O/Fe}]/\Delta\,T_{\text{eff}}$ (K)	$\Delta[\text{O/Fe}]/\Delta\,\log g$ (dex)	$\Delta[\text{O/Fe}]/\Delta[\text{Fe/H}]$ (dex)	$\Delta[\text{O/Fe}]/\Delta\,v_{micro}$ (km s^{-1})
ASCC 11	0.017	0.042	-0.031	-0.003
Alessi 1_1	0.009	0.065	-0.029	-0.001
Alessi 1_2	0.009	0.042	-0.061	-0.006
Alessi 1_3	0.008	0.042	-0.036	-0.001
Alessi 1_4	0.006	0.024	-0.064	-0.003
Alessi Teusch 11	0.007	0.065	-0.030	-0.002
Basel 11b_1	0.007	0.055	-0.030	-0.000
Basel 11b_2	0.004	0.044	-0.018	-0.002
Basel 11b_3	0.006	0.042	-0.029	0.000
COIN GAIA 30	0.007	0.022	-0.030	-0.001
Collinder 463_1	0.004	0.044	-0.030	-0.001
Collinder 463_2	0.004	0.060	-0.029	-0.001
Gulliver 18	0.019	0.072	-0.024	-0.006
Gulliver 24	0.010	0.069	-0.018	-0.002
Gulliver 37	0.009	0.048	-0.018	-0.004
NGC2437_1	0.005	0.051	-0.030	-0.001
NGC2437_2	0.009	0.043	-0.030	-0.002
NGC2437_3	0.014	0.043	-0.030	-0.001
NGC2437_4	0.008	0.045	-0.030	-0.003
NGC2437_5	0.009	0.065	-0.059	-0.001
NGC2437_6	0.008	0.042	-0.029	-0.001
NGC2437_7	0.013	0.080	-0.046	-0.001
NGC2509	0.008	0.046	-0.041	-0.001
NGC2548_1	0.005	0.085	-0.030	-0.002
NGC2548_2	0.007	0.064	-0.030	-0.002
NGC2548_3	0.006	0.042	-0.023	-0.001
NGC2548_4	0.007	0.043	-0.030	0.000
NGC7082	0.007	0.043	-0.029	-0.002
NGC7209_1	0.006	0.064	-0.017	-0.003
NGC7209_2	0.002	0.038	-0.036	-0.016
Tombaugh 5_1	0.006	0.063	-0.029	0.000
Tombaugh 5_2	0.006	0.042	-0.029	-0.002
Tombaugh 5_3	0.006	0.066	-0.030	-0.002
UPK222	0.023	0.046	-0.030	-0.001
Comparison clusters				
Collinder 350_1	0.011	0.073	-0.049	-0.004
Collinder 350_2	0.006	0.043	-0.031	0.000
NGC2682_1	0.007	0.029	-0.029	-0.004
NGC2682_2	0.014	0.041	-0.029	-0.003
NGC2682_3	0.006	0.042	-0.017	-0.002
NGC2682_4	0.007	0.042	-0.030	-0.001

Table A.3: Sensitivity matrix of Na for all targets

Name	Δ[Na/Fe]/Δ T$_{eff}$ (K)	Δ[Na/Fe]/Δ log g (dex)	Δ[Na/Fe]/Δ[Fe/H] (dex)	Δ[Na/Fe]/Δ v$_{micro}$ (km s^{-1})
ASCC 11	0.039	-0.011	-0.048	-0.061
Alessi 1_1	0.041	-0.011	-0.046	0.000
Alessi 1_2	0.039	-0.010	-0.089	-0.021
Alessi 1_3	0.036	-0.010	-0.054	-0.012
Alessi 1_4	0.000	0.042	-0.092	-0.012
Alessi Teusch 11	0.037	-0.013	-0.047	-0.028
Basel 11b_1	0.028	-0.016	-0.045	0.000
Basel 11b_2	0.016	-0.010	-0.022	0.000
Basel 11b_3	0.022	-0.002	-0.046	-0.011
COIN gaia 30	0.029	0.023	-0.087	0.000
Collinder 463_1	0.021	-0.009	-0.047	0.002
Collinder 463_2	0.000	-0.014	-0.046	-0.016
Gulliver 18	0.062	-0.043	-0.044	-0.068
Gulliver 24	0.040	-0.015	-0.027	0.000
Gulliver 37	0.034	-0.015	-0.026	-0.028
NGC2437_1	0.021	-0.025	-0.053	-0.016
NGC2437_2	0.042	-0.009	-0.045	0.000
NGC2437_3	0.059	-0.010	-0.046	0.000
NGC2437_4	0.039	-0.009	-0.044	-0.038
NGC2437_5	0.043	-0.013	-0.091	-0.014
NGC2437_6	0.053	0.015	-0.035	0.008
NGC2437_7	0.064	-0.023	-0.092	-0.019
NGC2509	0.031	-0.013	-0.063	-0.019
NGC2548_1	0.021	-0.011	-0.044	0.000
NGC2548_2	0.005	-0.006	-0.045	-0.030
NGC2548_3	0.031	-0.008	-0.036	-0.017
NGC2548_4	0.022	-0.022	-0.051	-0.005
NGC7082	0.029	-0.006	-0.047	-0.026
NGC7209_1	0.031	-0.012	-0.027	-0.032
NGC7209_2	0.023	-0.011	-0.046	-0.024
Tombaugh 5_1	0.032	-0.020	-0.043	0.001
Tombaugh 5_2	0.032	-0.009	-0.047	-0.031
Tombaugh 5_3	0.029	-0.026	-0.047	0.000
UPK222	0.084	-0.012	-0.047	0.000
Comparison clusters				
Collinder 350_1	0.011	0.073	-0.049	-0.004
Collinder 350_2	0.027	-0.012	-0.046	-0.013
NGC2682_1	0.035	-0.007	-0.045	-0.037
NGC2682_2	0.071	-0.009	-0.045	-0.033
NGC2682_3	0.029	-0.009	-0.027	-0.031
NGC2682_4	0.079	0.088	0.007	0.077

Table A.4: Sensitivity matrix of Mg for all targets

Name	Δ[Mg/Fe]/Δ T_{eff} (K)	Δ[Mg/Fe]/Δ log g (dex)	Δ[Mg/Fe]/Δ[Fe/H] (dex)	Δ[Mg/Fe]/Δ v_{micro} (km s^{-1})
ASCC 11	0.057	-0.016	-0.049	-0.093
Alessi 1_1	0.044	-0.016	-0.045	-0.020
Alessi 1_2	0.040	-0.013	-0.092	-0.115
Alessi 1_3	0.038	-0.013	-0.055	-0.016
Alessi 1_4	0.036	-0.008	-0.092	-0.017
Alessi Teusch_11	0.025	-0.003	-0.045	-0.040
Basel 11b_1	0.030	-0.015	-0.047	-0.016
Basel 11b_2	0.018	-0.012	-0.028	-0.035
Basel 11b_3	0.026	-0.01	-0.045	-0.019
COIN Gaia 30	0.029	-0.006	-0.046	-0.032
Collinder 463_1	0.019	-0.004	-0.046	-0.020
Collinder 463_2	0.018	-0.009	-0.045	-0.020
Gulliver 18	0.044	0.000	-0.033	-0.051
Gulliver 24	0.018	0.002	-0.024	-0.032
Gulliver 37	0.017	-0.011	-0.023	-0.085
NGC2437_1	0.029	-0.010	-0.047	-0.018
NGC2437_2	0.046	-0.014	-0.046	-0.037
NGC2437_3	0.064	-0.012	-0.048	-0.033
NGC2437_4	0.040	-0.009	-0.046	-0.076
NGC2437_5	0.044	-0.016	-0.093	-0.02
NGC2437_6	0.040	-0.008	-0.047	-0.01
NGC2437_7	0.048	-0.015	-0.069	-0.022
NGC2509	0.039	-0.019	-0.042	-0.077
NGC2548_1	0.039	-0.023	-0.047	-0.027
NGC2548_2	0.029	-0.010	-0.038	-0.019
NGC2548_3	0.030	-0.010	-0.045	0.054
NGC2458_4	0.026	-0.004	-0.068	-0.009
NGC7082	0.030	-0.016	-0.053	-0.053
NGC7209_1	0.031	-0.012	-0.028	-0.043
NGC7209_2	0.002	-0.057	-0.055	-0.067
Tombaugh 5_1	0.029	-0.015	-0.045	-0.021
Tombaugh 5_2	0.032	-0.009	-0.047	-0.046
Tombaugh 5_3	0.030	-0.019	-0.047	-0.039
UPK222	0.094	-0.012	-0.049	-0.034
Comparison clusters				
Collinder 350_1	0.019	-0.010	-0.068	-0.031
Collinder 350_2	-0.002	-0.076	-0.079	-0.047
NGC2682_1	0.028	-0.005	-0.043	-0.046
NGC2682_2	0.061	-0.008	-0.045	-0.046
NGC2682_3	0.017	-0.037	-0.034	-0.062
NGC2682_4	0.031	-0.018	-0.045	-0.039

Table A.5: Sensitivity matrix of Al for all targets

Name	$\Delta[\text{Al/Fe}]/\Delta\,T_{\text{eff}}$ (K)	$\Delta[\text{Al/Fe}]/\Delta\,\log g$ (dex)	$\Delta[\text{Al/Fe}]/\Delta[\text{Fe/H}]$ (dex)	$\Delta[\text{Al/Fe}]/\Delta\,v_{micro}$ (km s^{-1})
ASCC 11	0.047	-0.002	-0.052	-0.033
Alessi 1_1	0.045	0.000	-0.051	-0.011
Alessi 1_2	0.042	0.000	-0.100	-0.025
Alessi 1_3	0.037	0.000	-0.063	-0.008
Alessi 1_4	0.036	0.000	-0.105	-0.011
Alessi Teutsch_11	0.036	0.007	-0.051	-0.027
Basel 11b_1	0.030	0.000	-0.052	0.012
Basel 11b_2	0.018	0.000	-0.030	0.020
Basel 11b_3	0.027	0.000	-0.051	-0.012
COIN Gaia30	0.031	0.000	-0.051	-0.017
Collinder4631	0.036	0.002	-0.050	-0.008
Collinder4632	0.020	-0.005	-0.051	-0.013
Gulliver18	0.021	0.007	-0.051	-0.016
Gulliver24	0.072	0.017	-0.042	-0.056
Gulliver37	0.031	-0.007	-0.029	-0.030
NGC2437_1	0.030	-0.003	-0.031	-0.105
NGC2437_2	0.030	0.003	-0.050	-0.006
NGC2437_3	0.043	-0.002	-0.052	-0.020
NGC2437_4	0.066	0.000	-0.052	-0.025
NGC2437_5	0.040	0.002	-0.051	-0.010
NGC2437_6	0.048	0.000	-0.102	-0.015
NGC2437_7	0.043	-0.002	-0.051	-0.011
NGC2509	0.065	0.010	-0.084	-0.022
NGC2548_1	0.046	0.000	-0.073	-0.006
NGC2548_2	0.024	0.000	0.038	-0.033
NGC2548_3	0.045	-0.007	-0.052	-0.032
NGC2548_4	0.031	0.000	-0.040	-0.006
NGC7082	0.033	0.000	-0.050	-0.005
NGC7209_1	0.032	-0.001	-0.052	-0.030
NGC7209_2	0.077	-0.005	-0.051	-0.037
Tombaugh 5_1	0.030	0.000	-0.030	-0.022
Tombaugh 5_2	0.032	-0.002	-0.051	-0.027
Tombaugh 5_3	0.030	0.000	-0.051	-0.020
UPK219	0.031	0.000	-0.030	-0.015
Comparison clusters				
Collinder3501	0.043	-0.005	-0.050	-0.021
Collinder3502	0.016	-0.003	-0.053	-0.017
NGC2682_1	0.037	0.000	-0.050	-0.021
NGC2682_2	0.047	0.027	-0.036	0.000
NGC2682_3	0.031	-0.003	-0.052	-0.030
NGC2682_4	0.090	-0.002	-0.040	-0.025

Table A.6: Sensitivity matrix of Si for all targets

Name	$\Delta[Si/Fe]/\Delta\ T_{eff}$ (K)	$\Delta[Si/Fe]/\Delta$ log g (dex)	$\Delta[Si/Fe]/\Delta[Fe/H]$ (dex)	$\Delta[Si/Fe]/\Delta\ v_{micro}$ (km s^{-1})
ASCC 11	0.037	0.006	-0.047	-0.049
Alessi 1_1	0.004	0.026	-0.041	-0.021
Alessi 1_2	0.004	0.013	-0.083	-0.114
Alessi 1_3	-0.010	-0.016	-0.050	-0.019
Alessi 1_4	0.003	0.011	-0.082	-0.018
Alessi Teusch 11	-0.020	0.048	-0.043	-0.049
Basel 11b_1	0.005	0.021	-0.091	-0.016
Basel 11b_2	0.005	0.017	-0.025	-0.040
Basel 11b_3	-0.003	0.015	-0.038	-0.019
COIN gaia 30	0.002	0.009	-0.040	-0.031
Collinder 463_1	-0.001	0.025	-0.042	-0.011
Collinder 463_2	-0.006	0.020	-0.038	-0.023
Gulliver 18	-0.046	0.057	-0.029	-0.047
Gulliver 24	-0.029	0.070	-0.025	-0.035
Gulliver 37	-0.020	0.022	-0.020	-0.087
NGC2437_1	0.000	0.015	-0.040	-0.022
NGC2437_2	0.007	0.012	-0.041	-0.038
NGC2437_3	0.024	0.013	-0.044	-0.025
NGC2437_4	0.003	0.018	-0.040	-0.058
NGC2437_5	-0.000	0.021	-0.078	-0.023
NGC2437_6	0.001	0.014	-0.039	-0.020
NGC2437_7	-0.030	0.031	-0.059	-0.023
NGC2509	-0.011	0.068	-0.038	-0.090
NGC2548_1	0.013	0.025	-0.035	-0.017
NGC2548_2	0.003	0.025	-0.024	-0.045
NGC2548_3	-0.001	0.024	-0.037	-0.051
NGC2548_4	0.006	0.019	-0.041	-0.010
NGC7082	0.011	0.012	-0.043	-0.029
NGC7209_1	-0.001	0.024	-0.039	-0.052
NGC7209_2	-0.073	0.016	-0.035	-0.028
Tombaugh 5_1	-0.006	0.040	-0.059	-0.020
Tombaugh 5_2	0.001	0.0125	-0.040	-0.023
Tombaugh 5_3	0.003	0.014	-0.041	-0.046
UPK222	0.022	0.020	-0.043	-0.033
Comparison clusters				
Collinder 350_1	-0.030	0.030	-0.058	-0.012
Collinder 350_2	0.009	0.012	-0.044	-0.034
NGC2682_1	-0.019	0.034	-0.036	-0.044
NGC2682_2	-0.006	0.015	-0.030	-0.021
NGC2682_3	0.000	0.011	-0.039	-0.024
NGC2682_4	0.004	0.010	-0.056	-0.020

Table A.7: Sensitivity matrix of Ca for all targets

Name	$\Delta[Ca/Fe]/\Delta\,T_{eff}$ (K)	$\Delta[Ca/Fe]/\Delta\,\log g$ (dex)	$\Delta[Ca/Fe]/\Delta[Fe/H]$ (dex)	$\Delta[Ca/Fe]/\Delta\,v_{micro}$ (km s^{-1})
ASCC_11	0.071	-0.008	-0.055	-0.114
Alessi 1_1	0.074	-0.011	-0.052	-0.046
Alessi 1_2	0.063	-0.016	-0.104	-0.080
Alessi 1_3	0.056	-0.014	-0.063	-0.039
Alessi 1_4	0.057	-0.087	-0.106	-0.040
Alessi Teausch_11	0.001	-0.002	-0.216	0.000
Basel 11b_1	0.043	-0.014	-0.053	-0.037
Basel 11b_2	0.026	-0.009	-0.032	-0.074
Basel 11b_3	0.046	-0.009	-0.053	-0.041
COIN Gaia_30	0.043	-0.006	-0.053	-0.067
Collinder 463_1	0.031	-0.003	-0.055	-0.039
Collinder 463_2	0.030	-0.015	-0.052	-0.044
Gulliver_18	0.104	-0.012	-0.042	-0.132
Gulliver_24	0.053	-0.015	-0.031	-0.102
Gulliver_37	0.047	-0.034	-0.026	-0.186
NGC2437_1	0.046	-0.012	-0.053	-0.041
NGC2437_2	0.063	-0.011	-0.052	-0.067
NGC2437_3	0.093	-0.009	-0.053	-0.088
NGC2437_4	0.059	-0.014	-0.053	-0.128
NGC2437_5	0.076	-0.017	-0.108	-0.044
NGC2437_6	0.072	-0.006	-0.054	-0.040
NGC2437_7	0.090	-0.028	-0.080	-0.064
NGC2509	0.041	-0.038	-0.047	-0.156
NGC2548_1	0.056	-0.027	-0.050	-0.062
NGC2548_2	0.050	-0.010	-0.044	-0.046
NGC2548_3	0.054	-0.013	-0.050	-0.049
NGC2548_4	0.041	-0.018	-0.069	-0.028
NGC7082	0.050	-0.005	-0.053	-0.070
NGC7209_1	0.045	-0.018	-0.031	-0.101
MGC7209_2	0.030	-0.021	-0.050	-0.085
Tombaugh 5_1	0.051	-0.019	-0.051	-0.037
Tombaugh 5_2	0.056	-0.007	-0.053	-0.094
Tombaugh 5_3	0.048	-0.012	-0.056	-0.077
UPK219	0.134	-0.008	-0.054	-0.069
Comparison clusters				
Collinder 350_1	0.060	-0.010	-0.082	-0.058
Collinder 350_2	0.039	-0.013	-0.053	-0.039
NGC2682_1	0.035	-0.010	-0.050	-0.108
NGC2682_2	0.117	-0.012	-0.050	-0.094
NGC2682_3	0.047	-0.015	-0.030	-0.093
NGC268_4	0.043	-0.020	-0.050	-0.085

Table A.8: Sensitivity matrix of Ti for all targets

Name	Δ[Ti/Fe]/Δ T_{eff} (K)	Δ[Ti/Fe]/Δ log g (dex)	Δ[Ti/Fe]/Δ[Fe/H] (dex)	Δ[Ti/Fe]/Δ v_{micro} (km s^{-1})
ASCC 11	0.094	-0.002	-0.054	-0.037
Alessi 1_1	0.094	-0.004	-0.050	-0.040
Alessi 1_2	0.091	-0.001	-0.106	-0.068
Alessi 1_3	0.084	0.003	-0.064	-0.031
Alessi 1_4	0.082	-0.002	-0.106	-0.034
Alessi Teusch 11	0.077	0.000	-0.051	-0.100
Basel 11b_1	0.066	-0.002	-0.014	-0.028
Basel 11b_2	0.040	-0.004	-0.033	-0.053
Basel 11b_3	0.057	0.000	-0.052	-0.038
COIN gaia 30	0.062	-0.001	-0.053	-0.053
Collinder 463_1	0.045	0.000	-0.051	-0.023
Collinder 463_2	0.000	0.004	-0.052	-0.042
Gulliver 18	0.156	-0.003	-0.040	-0.157
Gulliver 24	0.078	-0.009	-0.028	-0.126
Gulliver 37	0.064	-0.007	-0.029	-0.262
NGC2437_1	0.066	0.003	-0.053	-0.033
NGC2437_2	0.099	0.002	-0.054	-0.062
NGC2437_3	0.143	-0.002	-0.056	-0.047
NGC2437_4	0.088	-0.002	-0.054	-0.093
NGC2437_5	0.105	0.002	-0.107	-0.038
NGC2437_6	0.086	0.000	-0.053	-0.031
NGC2437_7	0.162	-0.004	-0.080	-0.064
NGC2509	0.072	-0.009	-0.069	-0.062
NGC2548_1	0.048	-0.008	-0.055	-0.075
NGC2548_2	0.093	-0.003	-0.053	-0.082
NGC2548_3	0.067	-0.002	-0.042	-0.051
NGC2548_4	0.063	-0.001	-0.053	-0.020
NGC7082	0.069	0.001	-0.049	-0.051
NGC7209_1	0.067	-0.001	-0.032	-0.100
NGC7209_2	0.045	0.000	-0.049	-0.099
Tombaugh 5_1	0.066	-0.004	-0.051	-0.039
Tombaugh 5_2	0.067	0.001	-0.052	-0.089
Tombaugh 5_3	0.067	-0.004	-0.053	-0.069
UPK222	0.201	-0.006	-0.055	-0.038
Comparison clusters				
Collinder 350_1	0.087	0.010	-0.078	-0.066
Collinder 350_2	0.065	-0.003	-0.058	-0.032
NGC2682_1	0.073	-0.002	-0.051	-0.126
NGC2682_2	0.150	0.000	-0.052	-0.101
NGC2682_3	0.065	-0.002	-0.030	-0.096
NGC2682_4	0.067	0.000	-0.053	-0.079

Acknowledgements

Bibliography

Alonso, A., Arribas, S., & Martínez-Roger, C. 1999, A&AS, 140, 261.

Adamo, A., Östlin, G., & Zackrisson, E. 2011, MNRAS, 417, 1904.

Adamo, A., Zeidler, P., Kruijssen, J. M. D., et al. 2020, Space Sci. Rev., 216, 69.

Andreuzzi, G., Bragaglia, A., Tosi, M., et al. 2011, MNRAS, 412, 1265.

Argast, D., Samland, M., Thielemann, F.-K., et al. 2002, A&A, 388, 842.

Adibekyan, V. Z., Sousa, S. G., Santos, N. C., et al. 2012, A&A, 545, A32.

Ahumada, R., Prieto, C. A., Almeida, A., et al. 2020, ApJS, 249, 3.

Alonso-Santiago, J., Frasca, A., Catanzaro, G., et al. 2021, A&A, 656, A149.

Anders, E. & Grevesse, N. 1989, Geochimica Cosmochimica Acta, 53, 197.

Asplund, M., Grevesse, N., Sauval, A. J., et al. 2009, ARA&A, 47, 481.

Bastian, N. 2008, MNRAS, 390, 759.

Bowen, I. S. & Vaughan, A. H. 1973, Appl. Opt., 12, 1430.

Boeche, C., Siebert, A., Williams, M., et al. 2011, AJ, 142, 193.

Baratella, M., Carraro, G., D'Orazi, V., et al. 2018, AJ, 156, 244

Baratella, M., D'Orazi, V., Carraro, G., et al. 2020, A&A, 634, A34.

Baratella, M., D'Orazi, V., Biazzo, K., et al. 2020, A&A, 640, A123.

Bastian, N. & Lardo, C. 2018, ARA&A, 56, 83. doi:10.1146/annurev-astro-081817-051839

Bertelli Motta, C., Pasquali, A., Richer, J., et al. 2018, MNRAS, 478, 425

Bensby, T., Oey, M. S., Feltzing, S., et al. 2007, ApJ, 655, L89.

Benjamin, R. A., Churchwell, E., Babler, B. L., et al. 2003, PASP, 115, 953.

Bell, R. A., Eriksson, K., Gustafsson, B., et al. 1976, A&AS, 23, 37

Bekki, K. & Chiba, M. 2005, MNRAS, 356, 680. doi:10.1111/j.1365-2966.2004.08510.x

Blanco-Cuaresma, S. & Fraix-Burnet, D. 2018, A&A, 618, A65.

Bland-Hawthorn, J. & Gerhard, O. 2016, ARA&A, 54, 529.

Bragaglia, A. & Tosi, M. 2006, AJ, 131, 1544. doi:10.1086/499537

Bragaglia, A., Carretta, E., D'Orazi, V., et al. 2017, A&A, 607, A44.

Bragaglia, A., Sneden, C., Carretta, E., et al. 2014, ApJ, 796, 68.

Bossini, D., Vallenari, A., Bragaglia, A., et al. 2019, A&A, 623, A108

Boeche, C., Siebert, A., Piffl, T., et al. 2014, A&A, 568, A71.

Bovy, J., Rix, H.-W., & Hogg, D. W. 2012, ApJ, 751, 131.

Bovy, J., Rix, H.-W., Hogg, D. W., et al. 2012, ApJ, 755, 115.

Bovy, J., Rix, H.-W., Liu, C., et al. 2012, ApJ, 753, 148.

Cantat-Gaudin, T., Vallenari, A., Sordo, R., et al. 2018, A&A, 615, A49

Cantat-Gaudin, T., Anders, F., Castro-Ginard, A., et al. 2020, A&A, 640, A1

Carrera R., Bragaglia A., Cantat-Gaudin T., Vallenari A., Balaguer-Núñez L., Bossini D., Casamiquela L., et al., 2019, A&A, 623, A80

Casali, G., Magrini, L., Tognelli, E., et al. 2019, A&A, 629, A62.

Casali, G., Magrini, L., Frasca, A., et al. 2020, A&A, 643, A12.

Casali, G., Spina, L., Magrini, L., et al. 2020, A&A, 639, A127.

Casamiquela, L., Carrera, R., Jordi, C., et al. 2016, MNRAS, 458, 3150.

Casamiquela, L., Carrera, R., Blanco-Cuaresma, S., et al. 2017, MNRAS, 470, 4363.

Casamiquela, L., Carrera, R., Balaguer-Núñez, L., et al. 2018, A&A, 610, A66.

Casamiquela, L., Blanco-Cuaresma, S., Carrera, R., et al. 2019, MNRAS, 490, 1821.

Castelli, F. & Kurucz, R. L. 2003, Modelling of Stellar Atmospheres, 210, A20

Castro-Ginard, A., Jordi, C., Luri, X., et al. 2019, A&A, 627, A35

Castro-Ginard, A., Jordi, C., Luri, X., et al. 2020, A&A, 635, A45

Castro-Ginard, A., Jordi, C., Luri, X., et al. 2021, arXiv:2111.01819

Carrera, R., Bragaglia, A., Cantat-Gaudin, T., et al. 2019, A&A, 623, A80.

Carrera, R. & Pancino, E. 2011, A&A, 535, A30.

Carrera, R., Casamiquela, L. Bragaglia, A., et al., A&A, subm.

Carrera, R., Casamiquela, L., Carbajo-Hijarrubia, J., et al. 2022a, A&A, 658, A14. doi:10.1051/0004-6361/202141832

Carraro, G., Geisler, D., Villanova, S., et al. 2007, A&A, 476, 217.

Carretta, E., Bragaglia, A., Gratton, R. G., et al. 2010, A&A, 516, A55.

Caffau, E., Ludwig, H.-G., Steffen, M., et al. 2008, A&A, 488, 1031.

Caffau, E., Ludwig, H.-G., Malherbe, J.-M., et al. 2013, A&A, 554, A126.

Casey, A. R., Ruchti, G., Masseron, T., et al. 2016, MNRAS, 461, 3336.

Casey, A. R., Hawkins, K., Hogg, D. W., et al. 2017, ApJ, 840, 59.

Chandar, R., Fall, S. M., Whitmore, B. C., et al. 2017, ApJ, 849, 128.

Chabrier, G. 2003, PASP, 115, 763. doi:10.1086/376392

Chiappini, C. 2009, The Galaxy Disk in Cosmological Context, 254, 191.

Chiappini, C., Anders, F., Rodrigues, T. S., et al. 2015, A&A, 576, L12.

Chiappini, C., Matteucci, F., & Gratton, R. 1997, ApJ, 477, 765.

Cescutti, G. 2008, A&A, 481, 691.

Cunha K., Smith V. V., Lambert D. L., 1995, ApJ, 452, 634

Goddard, Q. E., Bastian, N., & Kennicutt, R. C. 2010, MNRAS, 405, 857.

Claudi, R., Benatti, S., Carleo, I., et al. 2016, Proc. SPIE, 9908, 99081A.

Cignoni, M., Tosi, M., Sabbi, E., et al. 2011, AJ, 141, 31.

Calura, F. & Menci, N. 2009, MNRAS, 400, 1347.

Carlos, M., Meléndez, J., do Nascimento, J.-D., et al. 2020, MNRAS, 492, 245.

Cropper, M., Katz, D., Sartoretti, P., et al. 2018, A&A, 616, A5.

Dalton, G., Trager, S., Abrams, D. C., et al. 2020, Proc. SPIE, 11447, 1144714. doi:10.1117/12.2561067

De Silva, G. M., Freeman, K. C., Bland-Hawthorn, J., et al. 2015, MNRAS, 449, 2604.

de Jong, R. S., Agertz, O., Berbel, A. A., et al. 2019, The Messenger, 175, 3. doi:10.18727/0722-6691/5117

De Silva, G. M., Freeman, K. C., Bland-Hawthorn, J., et al. 2015, MNRAS, 449, 2604. doi:10.1093/mnras/stv327

Denisenkov, P. A. & Denisenkova, S. N. 1990, Soviet Astronomy Letters, 16, 275

Dehnen, W. 1998, AJ, 115, 2384. doi:10.1086/300364

Donor J., Frinchaboy P. M., Cunha K., Thompson B., O'Connell J., Zasowski G., Jackson K. M., et al., 2018, AJ, 156, 142

Donor, J., Frinchaboy, P. M., Cunha, K., et al. 2020, AJ, 159, 199

Dotter, A., Conroy, C., Cargile, P., et al. 2017, ApJ, 840, 99.

Donati, P., Beccari, G., Bragaglia, A., et al. 2014, MNRAS, 437, 1241.

D'Orazi, V., Oliva, E., Bragaglia, A., et al. 2020, A&A, 633, A38.

Da Rio, N., Robberto, M., Hillenbrand, L. A., et al. 2012, ApJ, 748, 14.

De Silva, G. M., Freeman, K. C., Asplund, M., et al. 2007, AJ, 133, 1161.

De Silva, G. M., Freeman, K. C., Bland-Hawthorn, J., et al. 2007, AJ, 133, 694.

Dias, W. S., Alessi, B. S., Moitinho, A., et al. 2002, A&A, 389, 871.

Delgado Mena, E., Tsantaki, M., Sousa, S. G., et al. 2016, A&A, 587, A66.

Delgado Mena, E., Tsantaki, M., Adibekyan, V. Z., et al. 2017, A&A, 606, A94.

Delgado Mena, E., Moya, A., Adibekyan, V., et al. 2019, A&A, 624, A78.

D'Orazi, V., Gratton, R. G., Angelou, G. C., et al. 2015, MNRAS, 449, 4038.

Epstein, C. R., Johnson, J. A., Dong, S., et al. 2010, ApJ, 709, 447.

Feng, Y. & Krumholz, M. R. 2014, Nature, 513, 523.

Friel, E. D., Janes, K. A., Tavarez, M., et al. 2002, AJ, 124, 2693.

Frasca, A., Alonso-Santiago, J., Catanzaro, G., et al. 2019, A&A, 632, A16.

Fouesneau, M., Johnson, L. C., Weisz, D. R., et al. 2014, ApJ, 786, 117.

Fukui, Y., Ohama, A., Hanaoka, N., et al. 2014, ApJ, 780, 36.

Frasca, A., Guillout, P., Marilli, E., et al. 2006, A&A, 454, 301.

Frasca, A., Alonso-Santiago, J., Catanzaro, G., et al. 2019, A&A, 632, A16.

Franciosini, E., Tognelli, E., Degl'Innocenti, S., et al. 2020, Mem. Soc. Astron. Italiana, 91, 80

Freeman, K. & Bland-Hawthorn, J. 2002, ARA&A, 40, 487.

Freeman, K. & Bland-Hawthorn, J. 2002, ARA&A, 40, 487.

Garnett, D. R. & Shields, G. A. 1987, ApJ, 317, 82.

Gaia Collaboration, Brown, A. G. A., Vallenari, A., et al. 2018, A&A, 616, A1

Goddard, Q. E., Bastian, N., & Kennicutt, R. C. 2010, MNRAS, 405, 857.

Gunn, J. E., Siegmund, W. A., Mannery, E. J., et al. 2006, AJ, 131, 2332.

Gunn, J. E., Carr, M., Rockosi, C., et al. 1998, AJ, 116, 3040.

Gao, X., Lind, K., Amarsi, A. M., et al. 2018, MNRAS, 481, 2666.

Geller, A. M., Mathieu, R. D., Latham, D. W., et al. 2021,

Gilmore, G. & Reid, N. 1983, MNRAS, 202, 1025.

Gilmore, G., Randich, S., Asplund, M., et al. 2012, The Messenger, 147, 25

Girardi, L. 2016, ARA&A, 54, 95. doi:10.1146/annurev-astro-081915-023354

Gieles, M. & Portegies Zwart, S. F. 2011, MNRAS, 410, L6.

Gratton, R. G., Carretta, E., & Bragaglia, A. 2012, A&ARv, 20, 50.

Grevesse, N. & Sauval, A. J. 1998, Space Sci. Rev., 85, 161.

Getman, K. V., Feigelson, E. D., Kuhn, M. A., et al. 2018, MNRAS, 476, 1213.

Gutiérrez Albarrán, M. L., Montes, D., Gómez Garrido, M., et al. 2020, A&A, 643, A71.

Gossage, S., Conroy, C., Dotter, A., et al. 2018, ApJ, 863, 67.

Holtzman, J. A., Harrison, T. E., & Coughlin, J. L. 2010, Advances in Astronomy, 2010, 193086.

Netopil, M., Paunzen, E., Heiter, U., et al. 2016, A&A, 585, A150.

He, Z.-H., Xu, Y., Hao, C.-J., et al. 2021, Research in Astronomy and Astrophysics, 21, 093.

Hayden, M. R., Bovy, J., Holtzman, J. A., et al. 2015, ApJ, 808, 132.

He, Z.-H., Xu, Y., Hao, C.-J., et al. 2021, Research in Astronomy and Astrophysics, 21, 093. doi:10.1088/1674-4527/21/4/93

Jacobson, H. R., Pilachowski, C. A., & Friel, E. D. 2011, AJ, 142, 59.

Jackson, R. J., Jeffries, R. D., Wright, N. J., et al. 2022, MNRAS, 509, 1664. doi:10.1093/mnras/stab3032

Jeffries, R. D., Jackson, R. J., Cottaar, M., et al. 2014, A&A, 563, A94

Jönsson H., Allende Prieto C., Holtzman J. A., Feuillet D. K., Hawkins K., Cunha K., Mészáros S., et al., 2018, AJ, 156, 126

Johnson, L. C., Seth, A. C., Dalcanton, J. J., et al. 2012, ApJ, 752, 95.

Jönsson H., Holtzman J. A., Allende Prieto C., Cunha K., García-Hernández D. A., Hasselquist S., Masseron T., et al., 2020, AJ, 160, 120

Jofré, P., Heiter, U., & Soubiran, C. 2019, ARA&A, 57, 571

Jacobson, H. R., Friel, E. D., & Pilachowski, C. A. 2007, AJ, 134, 1216.

Jackson, R. J., Jeffries, R. D., Wright, N. J., et al. 2020, MNRAS, 496, 4701.

Kharchenko, N. V., Piskunov, A. E., Schilbach, E., et al. 2012, A&A, 543, A156.

Kharchenko, N. V., Piskunov, A. E., Schilbach, E., et al. 2013, A&A, 558, A53

Kharchenko, N. V., Piskunov, A. E., Röser, S., et al. 2005, A&A, 440, 403.

Kruijssen, J. M. D., Maschberger, T., Moeckel, N., et al. 2012, MNRAS, 419, 841.

Kruijssen, J. M. D. & Bastian, N. 2016, MNRAS, 457, L24.

van der Kruit, P. C. 1986, A&A, 157, 230

King J. R., Soderblom D. R., Fischer D., Jones B. F., 2000, ApJ, 533, 944

Kobayashi, C., Tsujimoto, T., & Nomoto, K. 2000, ApJ, 539, 26.

Kobayashi, C., Umeda, H., Nomoto, K., et al. 2006, ApJ, 653, 1145.

Kobayashi, C. & Nomoto, K. 2009, ApJ, 707, 1466.

Kobayashi, C., Tominaga, N., & Nomoto, K. 2011, ApJ, 730, L14.

Kobayashi, C. & Nakasato, N. 2011, ApJ, 729, 16.

Kroupa, P. 2008, Pathways Through an Eclectic Universe, 390, 3

Krumholz, M. R., McKee, C. F., & Bland-Hawthorn, J. 2019, ARA&A, 57, 227.

Kruijssen, J. M. D., Pelupessy, F. I., Lamers, H. J. G. L. M., et al. 2011, MNRAS, 414, 1339.

Kobayashi, C., Karakas, A. I., & Lugaro, M. 2020, ApJ, 900, 179.

Kounkel, M. & Covey, K. 2019, AJ, 158, 122.

Ishigaki, M. N., Chiba, M., & Aoki, W. 2012, ApJ, 753, 64.

Lada, C. J. & Lada, E. A. 2003, ARA&A, 41, 57. doi:10.1146/annurev.astro.41.011802.094844

Lagarde, N., Robin, A. C., Reylé, C., et al. 2017, A&A, 601, A27.

Lagarde, N., Reylé, C., Robin, A. C., et al. 2019, A&A, 621, A24.

Lagarde, N., Decressin, T., Charbonnel, C., et al. 2012, A&A, 543, A108.

Lagarde, N., Anderson, R. I., Charbonnel, C., et al. 2014, A&A, 570, C2.

Larson, R. B. 1976, MNRAS, 176, 31.

Leiner, E., Mathieu, R. D., Stello, D., et al. 2016, ApJ, 832, L13.

Liu, L. & Pang, X. 2019, ApJS, 245, 32

Liu, F., Yong, D., Asplund, M., et al. 2016, MNRAS, 457, 3934.

Liu, F., Asplund, M., Yong, D., et al. 2016, MNRAS, 463, 696.

Luo, A.-L., Zhao, Y.-H., Zhao, G., et al. 2015, Research in Astronomy and Astrophysics, 15, 1095.

Luck, R. E. 2015, AJ, 150, 88.

Lee, Y. S., Beers, T. C., An, D., et al. 2011, ApJ, 738, 187.

Leung, H. W. & Bovy, J. 2019, MNRAS, 483, 3255.

Lind, K., Asplund, M., Barklem, P. S., et al. 2011, A&A, 528, A103.

Luck, R. E. 2015, AJ, 150, 88.

Marsakov, V. A. & Borkova, T. V. 2005, Astronomy Letters, 31, 515.

Martínez-Delgado, D., Peñarrubia, J., Gabany, R. J., et al. 2008, ApJ, 689, 184.

Matteucci, F. & Francois, P. 1989, MNRAS, 239, 885.

Majewski, S. R., Schiavon, R. P., Frinchaboy, P. M., et al. 2017, AJ, 154, 94. doi:10.3847/1538-3881/aa784d

Mapelli, M., Vallenari, A., Jeffries, R. D., et al. 2015, A&A, 578, A35

Marigo, P., Girardi, L., Bressan, A., et al. 2017, ApJ, 835, 77.

Martig, M., Bournaud, F., Teyssier, R., et al. 2009, ApJ, 707, 250.

Martig, M., Bournaud, F., Croton, D. J., et al. 2012, ApJ, 756, 26.

McCrady, N. & Graham, J. R. 2007, ApJ, 663, 844.

Meléndez, J. & Barbuy, B. 2009, A&A, 497, 611.

Meléndez, J., Bedell, M., Bean, J. L., et al. 2017, A&A, 597, A34.

Meléndez, J., Ramírez, I., Karakas, A. I., et al. 2014, ApJ, 791, 14.

Maíz-Apellániz, J. 2002, Extragalactic Star Clusters, 207, 697

Monteiro, H. & Dias, W. S. 2019, MNRAS, 487, 2385.

Magrini, L., Sestito, P., Randich, S., et al. 2009, A&A, 494, 95

Magrini, L., Spina, L., Randich, S., et al. 2018, A&A, 617, A106.

Magrini, L., Lagarde, N., Charbonnel, C., et al. 2021a, A&A, 651, A84. doi:10.1051/0004-6361/202140935

Magrini, L., Smiljanic, R., Franciosini, E., et al. 2021, A&A, 655, A23. doi:10.1051/0004-6361/202141275

Matteucci, F. 2021, A&ARv, 29, 5. doi:10.1007/s00159-021-00133-8

Minchev, I., Anders, F., Recio-Blanco, A., et al. 2018, MNRAS, 481, 1645.

Minchev, I., Chiappini, C., & Martig, M. 2013, A&A, 558, A9.

Minchev, I., Chiappini, C., & Martig, M. 2014, A&A, 572, A92.

Nordlander, T. & Lind, K. 2017, A&A, 607, A75.

Nomoto, K., Kobayashi, C., & Tominaga, N. 2013, ARA&A, 51, 457.

Roškar R., Debattista V. P., Quinn T. R., Wadsley J., 2012, MNRAS, 426, 2089.

Reggiani, M., Robberto, M., Da Rio, N., et al. 2011, A&A, 534, A83.

Ruffoni, M. P., Den Hartog, E. A., Lawler, J. E., et al. 2014, MNRAS, 441, 3127.

Robberto, M., Soderblom, D. R., Bergeron, E., et al. 2013, ApJS, 207, 10.

Randich, S., Gilmore, G., Magrini, L., et al, A&A, submitted

Mermilliod, J.-C., Andersen, J., Latham, D. W., et al. 2007, A&A, 473, 829.

Mermilliod, J. C., Mayor, M., & Udry, S. 2008, A&A, 485, 303.

Minchev, I., Chiappini, C., & Martig, M. 2013, A&A, 558, A9.

Minchev, I., Chiappini, C., Martig, M., et al. 2014a, ApJ, 781, L20.

Minchev, I., Chiappini, C., & Martig, M. 2014b, A&A, 572, A92.

Ness, M., Hogg, D. W., Rix, H.-W., et al. 2016, ApJ, 823, 114

Netopil, M., Paunzen, E., Heiter, U., et al. 2016, A&A, 585, A150

Nordlander, T. & Lind, K. 2017, A&A, 607, A75.

Paunzen, E. 2008, Contributions of the Astronomical Observatory Skalnate Pleso, 38, 435

Piskunov, A. E., Schilbach, E., Kharchenko, N. V., et al. 2007, A&A, 468, 151.

Piskunov, A. E., Just, A., Kharchenko, N. V., et al. 2018, A&A, 614, A22.

Pastorelli, G., Marigo, P., Girardi, L., et al. 2020, MNRAS, 498, 3283.

Pakhomov, Y. V., Antipova, L. I., Boyarchuk, A. A., et al. 2009, Astronomy Reports, 53, 660.

Portegies Zwart, S. F., McMillan, S. L. W., & Gieles, M. 2010, ARA&A, 48, 431.

Prantzos, N., Charbonnel, C., & Iliadis, C. 2007, A&A, 470, 179.

Prantzos, N., Casse, M., & Vangioni-Flam, E. 1993, ApJ, 403, 630.

Pace, G., Castro, M., Meléndez, J., et al. 2012, A&A, 541, A150.

Pastorelli, G., Marigo, P., Girardi, L., et al. 2020, MNRAS, 498, 3283.

Quillen, A. C., De Silva, G., Sharma, S., et al. 2018, MNRAS, 478, 228.

Queiroz, A. B. A., Anders, F., Chiappini, C., et al. 2020, A&A, 638, A76.

Reddy, A. B. S., Lambert, D. L., & Giridhar, S. 2016, MNRAS, 463, 4366.

Reid, M. J., Menten, K. M., Brunthaler, A., et al. 2014, ApJ, 783, 130.

Rosales-Ortega, F. F., Kennicutt, R. C., Sánchez, S. F., et al. 2010, MNRAS, 405, 735.

Ruprecht, J. 1966, Bulletin of the Astronomical Institutes of Czechoslovakia, 17, 33

Randich, S., Gilmore, G., Magrini, L., et al, A&A, submitted

Romano, D., Magrini, L., Randich, S., et al. 2021, A&A, 653, A72. doi:10.1051/0004-6361/202141340

Salaris, M., Pietrinferni, A., Piersimoni, A. M., et al. 2015, A&A, 583, A87.

Salpeter, E. E. 1959, ApJ, 129, 608.

Salpeter, E. E. 1955, ApJ, 121, 161. doi:10.1086/145971

Searle, L. & Zinn, R. 1978, ApJ, 225, 357. doi:10.1086/156499

Searle, L., Sargent, W. L. W., & Bagnuolo, W. G. 1973, ApJ, 179, 427.

Sagar, R. & Griffiths, W. K. 1998, MNRAS, 299, 777.

Schlafly, E. F. & Finkbeiner, D. P. 2011, ApJ, 737, 103.

Schmidt, M. 1959, ApJ, 129, 243.

Siebert, A., Bienaymé, O., Binney, J., et al. 2008, MNRAS, 391, 793.

Smiljanic, R., Romano, D., Bragaglia, A., et al. 2016, A&A, 589, A115

Spina, L., Randich, S., Magrini, L., et al. 2017, A&A, 601, A70.

Spina, L., Nordlander, T., Casey, A. R., et al. 2020, ApJ, 895, 52.

Spina, L., Ting, Y.-S., De Silva, G. M., et al. 2021, MNRAS, 503, 3279.

Soubiran, C., Bienaymé, O., & Siebert, A. 2003, A&A, 398, 141.

Soubiran C., Cantat-Gaudin T., Romero-Gómez M., Casamiquela L., Jordi C., Vallenari A., Antoja T., et al., 2018, A&A, 619, A155

Sousa, S. G., Santos, N. C., Adibekyan, V., et al. 2015, A&A, 577, A67.

Sun, Q., Deliyannis, C. P., Steinhauer, A., et al. 2020, AJ, 159, 220.

Skrutskie, M. F., Cutri, R. M., Stiening, R., et al. 2006, AJ, 131, 1163.

Schmeja, S., Kharchenko, N. V., Piskunov, A. E., et al. 2014, A&A, 568, A51.

Scholz, R.-D., Kharchenko, N. V., Piskunov, A. E., et al. 2015, A&A, 581, A39.

Seleznev, A. F., Carraro, G., Costa, E., et al. 2010, New Astron., 15, 61.

Sanna, N., Franciosini, E., Pancino, E., et al. 2020, A&A, 639, L2.

Sartoretti, P., Katz, D., Cropper, M., et al. 2018, A&A, 616, A6.

Sharma, S., Hayden, M. R., Bland-Hawthorn, J., et al. 2020

Sharma, S., Hayden, M. R., & Bland-Hawthorn, J. 2021, MNRAS, 507, 5882.

Silva Aguirre, V., Bojsen-Hansen, M., Slumstrup, D., et al. 2018, MNRAS, 475, 5487.

Sim, G., Lee, S. H., Ann, H. B., et al. 2019, Journal of Korean Astronomical Society, 52, 145. doi:10.5303/JKAS.2019.52.5.145

Smiljanic, R. 2012, MNRAS, 422, 1562. doi:10.1111/j.1365-2966.2012.20729.x

Smiljanic, R., Donati, P., Bragaglia, A., et al. 2018, A&A, 616, A112. doi:10.1051/0004-6361/201832877

Spina, L., Magrini, L., & Cunha, K. 2022, Universe, 8, 87. doi:10.3390/universe8020087

Spitoni, E., Silva Aguirre, V., Matteucci, F., et al. 2019, A&A, 623, A60.

Spitoni, E., Verma, K., Silva Aguirre, V., et al

Sun, W.-X., Huang, Y., Wang, H.-F., et al. 2020, ApJ, 903, 12. doi:10.3847/1538-4357/abb1b7

Tinsley, B. M. 1980, Fundamentals Cosmic Phys., 5, 287

Tinsley, B. M. 1980, Fundamentals Cosmic Phys., 5, 287

Timmes, F. X., Woosley, S. E., & Weaver, T. A. 1995, ApJS, 98, 617.

Torres, G., Andersen, J., & Giménez, A. 2010, A&ARv, 18, 67

Tumlinson, J. 2006, ApJ, 641, 1.

Tadross, A. L. 2003, New Astron., 8, 737.

Tarricq, Y., Soubiran, C., Casamiquela, L., et al. 2021, A&A, 647, A19.

Taylor, M. B. 2005, Astronomical Data Analysis Software and Systems XIV, 347, 29

Minchev, I., Chiappini, C., & Martig, M. 2014, A&A, 572, A92.

Villanova, S., Geisler, D., Carraro, G., et al. 2013, ApJ, 778, 186.

Ventura, P., Di Criscienzo, M., Carini, R., et al. 2013, MNRAS, 431, 3642.

Vincenzo, F., Weinberg, D. H., Miglio, A., et al. 2021, MNRAS, 508, 5903. doi:10.1093/mnras/stab2899

Warren, S. R. & Cole, A. A. 2009, MNRAS, 393, 272.

Wang, L.-L., Luo, A.-L., Shen, S.-Y., et al. 2018, MNRAS, 474, 1873.

Wright, E. L., Eisenhardt, P. R. M., Mainzer, A. K., et al. 2010, AJ, 140, 1868.

Weinberg, D. H., Holtzman, J. A., Hasselquist, S., et al. 2019, ApJ, 874, 102. doi:10.3847/1538-4357/ab07c7

Yana Galarza, J., Meléndez, J., Lorenzo-Oliveira, D., et al. 2019, MNRAS, 490, L86.

Yen, S. X., Reffert, S., Schilbach, E., et al. 2018, A&A, 615, A12.

Yanny, B., Rockosi, C., Newberg, H. J., et al. 2009, AJ, 137, 4377.

Yoshii, Y. 1982, PASJ, 34, 365

Yong, D., Grundahl, F., Nissen, P. E., et al. 2005, A&A, 438, 875.

Yong, D., Carney, B. W., & Friel, E. D. 2012, AJ, 144, 95.

Zhang, J., Zhao, J., Oswalt, T. D., et al. 2019, ApJ, 887, 84.

Zhang, Q. & Fall, S. M. 1999, ApJ, 527, L81. .

Zasowski, G., Schultheis, M., Hasselquist, S., et al. 2019, ApJ, 870, 138.

Zhang, R., Lucatello, S., Bragaglia, A., et al. 2021, A&A, 654, A77. doi:10.1051/0004-6361/202141188

Zhang, R., Lucatello, S., Bragaglia, A., et al. 2022, A&A submitted

Zhong, J., Chen, L., Wu, D., et al. 2020, A&A, 640, A127. doi:10.1051/0004-6361/201937131